UNIVERSITY OF OKLAHOMA

GRADUATE COLLEGE

LOW-COST RADAR TECHNIQUES FOR CONGESTED ENVIRONMENTS

A THESIS

SUBMITTED TO THE GRADUATE FACULTY

in partial fulfillment of the requirements for the

Degree of

MASTER OF SCIENCE

By

Lucía B. Torres
Norman, Oklahoma
2025

LOW-COST RADAR TECHNIQUES FOR CONGESTED ENVIRONMENTS

A THESIS APPROVED FOR THE
SCHOOL OF ELECTRICAL AND COMPUTER ENGINEERING

BY THE COMMITTEE CONSISTING OF

Dr. Justin Metcalf, Chair

Dr. Nathan Goodman

Dr. Russell Kenney

Para Mamá y Papá

Acknowledgments

First, I have to thank Dr. Justin Metcalf who has supported my research journey since I was a freshman. His mentorship and support has been the main pillar of my time here at the ARRC. I also want to thank Dr. Nathan Goodman and Dr. Russell Kenney for agreeing to serve on my committee. They have greatly helped in the shaping of this work.

Thank you to Cody Kieu, Breanna Mapes, and Sam Roach for being there to congregate, solve crossword puzzles, go on sweet treat trips, play guitar hero, and eat lunch with. I would not have made it through this year without your unwavering support and friendship.

I would also like to thank my boyfriend, Parker Heard, who has supported me through every accomplishment, success, cranky mood swing, and mental breakdown. I would not be here today without his constant love and support.

Thank you to my parents, Sebastian Torres and Lorena Serventi de Torres, who taught me how far hard work and passion can get you.

I thank the Defense Advanced Research Projects Agency (DARPA) for their support of this research under grant HR0011-20-1-0007 and the Federal Aviation Administration under Agreement 697DCK-25-H-00001. The views, opinions and/or findings expressed are those of the author and should not be interpreted as representing the official views or policies of the Department of Defense, Federal Aviation Administration, or the U.S. Government.

Table of Contents

List of Tables

List of Figures

Abstract

The radio frequency spectrum is overcrowded by the ever-increasing number of technologies that use it. Functioning within the spectrum can be and often is a difficult task that leads to complications due to the congestion from different users and technologies operating at the same desired frequencies. In particular, this thesis will explore two types of interference, a common and dangerous side effect of the congested RF spectrum, that occur between radar and communications systems: wideband interference and out-of-band interference.

Wideband technologies operate across a broad range of frequencies that can overlap and encompass narrow band systems, causing degradation in performance. This is commonly seen with wideband communication signals, such as 5G, interfering with narrowband radar systems. Further, these wideband signals are often sampled at different – usually higher – rates than the narrowband signals, making undersampling and its associated complications another undesirable consequence of wideband interference. Nevertheless, this work presents a novel post-processing algorithm that aims to recover lost information, resolving the issues caused by undersampling. In conjunction with this, a simulation of an $\Sigma - \Delta$ analog-to-digital converter, developed in MATLAB, is used to simulate the sampling – and thus the undersampling – process that occurs when digitizing data.

Adjacent frequency bands, such as the radar altimeter and 5G network bands, are likely to suffer from out-of-band interference. 5G networks reside in one of the

most populous frequency bands, ranging from 3.7 to 4.2 GHz. Radar altimeters are allocated directly above this, in the adjacent band from 4.2 to 4.4 GHz. Radar altimeters are used in aircraft for landing, low-visibility flights, and other flight maneuvers. 5G emissions can cause out-of-band interference on radar altimeters, causing performance loss in the radar altimeter's receiver. It is often due to the low quality front-end filters that cannot filter out lower band emissions that this interference occurs, however, it is also possible for spurious 5G emissions to leak into the radar altimeter band. This work aims to understand out-of-band interference and how different post-processing techniques – namely, matched filtering and stretch processing – are able to mitigate this interference. Furthermore, this includes experimentation and analysis to understand radar altimeters and 5G networks both individually and in combination.

This thesis introduces three main contributions: an algorithm to recover undersampled information, an analog-to-digital converter simulation, and an analysis of 5G and radar altimeter signals and their interactions. Ultimately, this thesis simulates, experiments, and analyzes congestion in the RF spectrum with the intention of developing solutions that will contribute to mitigating the negative effects caused by coexistence.

Chapter 1

Introduction

1.1 Spectrum Sharing

The radio frequency (RF) spectrum is a portion of the electromagnetic spectrum that has been shared and regulated for decades. Today, all technologies are assigned specific frequency bands (ranges or spans of frequency) in which they are allowed to operate (transmit and receive). Figure 1.1 shows how the RF spectrum has been divided so that all technologies and their various applications have a designated frequency band [1].

Although the RF spectrum is large, spanning from 3 Hz to 300 GHz, the actual desirable frequency bands are between 30 MHz and 30 GHz. At these frequencies, propagation is good and the bandwidth is achievable and adequate for various uses [1]. In other words, there is no overall spectrum scarcity, but there is overwhelming use within the desirable frequency bands. Communications and radar technologies operating in this desirable spectrum will be the focus of this thesis.

1.1.1 RF Spectrum History

The RF spectrum is a finite and valuable resource used by and for military, licensed, and general users. In 1934, the U.S. Congress created the Federal Communications Commission (FCC), an independent agency with the mission of managing and allocating non-federal use of the RF spectrum [2]. In 1981, the spectrum lottery was introduced, in which applicants would apply for a spectrum license and the FCC would randomly assign frequencies [2]. This lottery system only caused profiteering, and thus auctions were introduced in 1993 as an alternate solution.

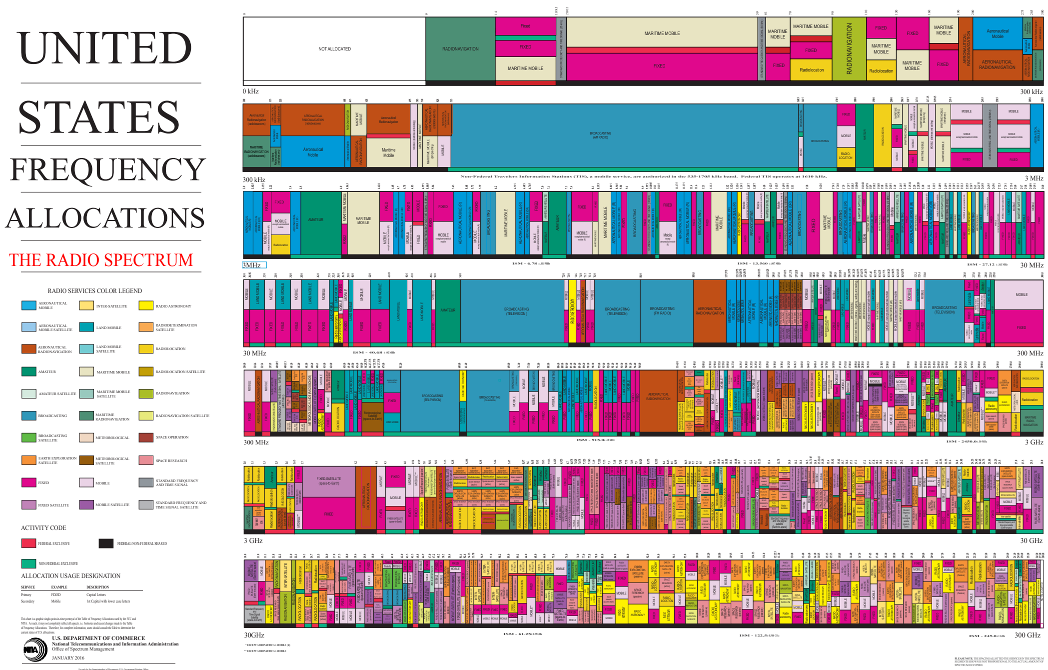

Figure 1.1: United States RF frequency spectrum allocation chart. The spectrum of focus for this thesis is from 3.7 GHz to 4.4 GHz, which includes fixed-satellite (space-to-earth), fixed, and aeronautical radionavigation technologies. Courtesy of [1].

The spectrum auction allowed the FCC to use competitive bidding to grant spectrum to users [2]. The purpose of the spectrum auction was to promote the deployment of new technology and increase services, especially in rural regions [2]. This, in turn, also increased competition and diversified licensees, creating a more efficient use of the RF spectrum.

The FCC's authority to auction spectrum has been extended continuously since 1998, when it was first supposed to end, and has presently been extended until September 30th, 2025 [2]. However, if the FCC's auctioning authority were to not be extended, as occurred in 2023, the spectrum auctioning authority will lapse. This causes uncertainty as some licenses have not yet been granted and future planning by the FCC is halted.

Today, the FCC still manages and regulates the RF spectrum with the goal of maintaining an efficient spectrum with collaboration between all licensees (i.e., wireless communication companies and the military).

1.1.2 Congestion in the RF Spectrum

The overarching spectrum sharing problem is one in which limited RF spectral bands are shared by many different users (and technologies) over time and space [3]. Functioning in the desirable 30 MHz to 30 GHz range can be, and often is, difficult as it leads to unexpected complications due to the number of users and technologies that are constantly fighting for bandwidth. Interference is a common and unfavorable side effect of a congested spectrum, such as this one. Specifically for this thesis, two different types of interference that occur between communications and radar will be explored: wideband interference (WBI) and out-of-band (OOB) interference.

Wideband systems utilize a broad range of frequencies, encapsulating even an entire frequency band. For technologies that reside in the same frequency band, this can be very detrimental to performance. More specifically, WBI will disrupt a large portion of the frequency spectrum. Narrowband technologies can be completely corrupted by WBI. For this thesis, WBI will be explored with a radar system operating within the same frequency band as a wideband communications system. This will be further discussed in Chapters 2 and 4.

Adjacent frequency bands are likely to suffer from OOB interference from their neighbors. OOB interference occurs when emissions from systems in other (usually adjacent) frequency bands leak into the operating band. These OOB emissions cause performance loss for the operating technology. Consider Fifth Generation New Radio (simply, 5G) networks and radar altimeters (radalts), which reside in adjacent frequency bands. The OOB emissions that occur from 5G transmissions affect the performance of radalt receivers. This will be further discussed in Chapters 3 and 5.

1.2 Background

With the ever-increasing need for communication networks, radars are no longer isolated in the RF spectrum. In fact, radars face interference from these communication systems that is potentially detrimental, as discussed in the previous section (Section 1.1.2). As communication demands increase and, with that, frequency allocations for communication systems, efficient spectrum sharing frameworks and techniques are needed to enable coexistence.

For example, the unlicensed national information infrastructure (U-NII) bands are a regulatory framework that exists between radar and communication systems [4]. This framework, applied in the 5 GHz band, deems commercial weather radar as the primary user and wideband networks as secondary, only to operate when the radar is not detected in the frequency band. However, the weather radar still experiences interference from the communications network [5][6]. Inversely, another framework sets the radar as the secondary user, where it dynamically accesses available bandwidth on a pulse-by-pulse basis [7][8][9][10].

Unfortunately, these frameworks still present opportunities for interference to occur between technologies. For example, in [5], a terminal Doppler weather radar (TDWR) cannot find any available spectrum and thus is forced to operate in the presence of another technology. This scenario, where radars suffer from interference caused by a communications system, must be mitigated so that radars can continue operating as expected.

Reference signal reconstruction techniques are commonly used in passive radars for interference extraction [11][12]. In [13], an interfering orthogonal frequency-division multiplexing (OFDM) signal is demodulated and remodulated to create a signal that can be subtracted from the radar's received data. These demodulation and remodulation techniques have shown promise for various radar systems [13][14].

This work presents a post-processing algorithm that recovers the communication signal sampled by a narrowband radar application. Its goal is to mitigate the WBI – a natural effect of spectrum sharing – caused by communication transmissions on the radar's spectrum. This allows radars, which often need to operate in the same frequency band as communication networks, to continue operating at the desired performance level. This work approaches WBI from the perspective of the radar application and aims to determine whether WBI can be mitigated in post-processing, rather than prior to any operation, as has been done in the past.

For reference, Appendix A contains experimentation conducted by the Department of Defense pertaining to the OOB interference problem presented in this thesis. [15] contains information on various 5G base stations and how their emissions were measured to observe OOB on radalts. However, this work takes a new, low-cost approach to investigate and observe OOB interference from 5G emissions on radalts.

1.3 Contributions

This thesis presents the following novel contributions:

- An analog-to-digital converter (ADC) simulation in MATLAB for a $\Sigma - \Delta$ ADC architecture, including the mathematical model for a 12-bit $\Sigma - \Delta$ ADC.
- A post-processing algorithm, aptly named the Algorithm for Information Recovery (AIR), uses the principles of random signals to recover lost information due to undersampling occurring in the ADC. Recovering this information allows ADCs to sample below the Nyquist frequency without loss of information.
- An analysis of OOB interference to better understand how 5G emissions affect radalts. This work establishes the foundational systems and lays our the groundwork for future analysis on this crucial concern.

1.4 Thesis Outline

This thesis is organized into the following chapters:

Chapter 2 provides the background on ADC hardware and how wideband communication signals effect narrowband radar signals. This chapter includes a brief overview on the principles of sampling.

Chapter 3 focuses on the history and functionality of radalts and 5G networks. This also included a brief introduction to the OOB interference that may occur from 5G emissions on radalt receivers.

Chapter 4 focuses on the mathematical theory behind ADC hardware and an algorithm to recover lost information. The post-processing algorithm, AIR, is tested in simulation and experiments to determine its accuracy, robustness, and limits.

Chapter 5 includes all the tests, experiments, analysis, and discussion on OOB interference, further explaining the interactions between 5G transmissions and radalt receivers. Understanding these interactions with experimentation and theory allows both telecommunications and aircraft developers to determine proper mitigation techniques.

In Chapter 6, conclusions on coexistence in the RF spectrum – namely, communication signals interfering with radar signals – and future directions of the work presented in the previous chapters of this thesis are given.

Chapter 2

Wideband Communication Interference on Radars

This chapter provides the necessary background to understand WBI and the dangers of undersampling. It is setup as follows. Sections 2.1.1 – 2.1.4 continue to discuss wideband communications. Section 2.2 describes binary phase shift keying – a common modulation method and the waveform used in Chapter 4 of this thesis. Section 2.4 is an introduction to ADCs and its different architectures. Section 2.3 explains sampling theory.

2.1 Wideband Communications

Wideband (also called broadband) communication is characterized by its broad frequency bandwidth, occupying a large portion of the RF spectrum. Common technologies under the wideband communications umbrella include ultra-wideband (UWB), satellite communications, and 5G wireless networks (described further in Section 3.3).

Wideband communications have, over the past couple decades, impacted the availability and distribution of information. They have provided an accessible, fast, and inexpensive form of transportation for information [16]. Now more than ever, users can (and do) effectively engage with information, especially compared to older and slower networks that do not promote interaction. In other words, the availability of an always-on high-speed connection increases online activity and thus activity in the RF spectrum [16].

2.1.1 Ultra-Wideband Communications

Ultra-wideband communications are a subset of wideband communications, revolutionary for their ability to transmit large amounts of data over a very broad frequency spectrum [17]. A communications system is considered UWB if the absolute bandwidth is more than 500 MHz and operates in the 3.1 to 10.9 GHz range, as per the FCC.

Unlike other communication techniques, UWB utilizes short pulses (which directly relate to a wide bandwidth). UWB systems transmit information by generating energy at specific time instants and occupying a large bandwidth, enabling pulse position or time modulation [17]. Information can also be modulated on the UWB signals.

Communication systems need more mobility, flexibility, and higher data rates to handle the ever-increasing number of users. The capacity of the communications channel is directly related to its bandwidth, making wideband communications inevitable. Some advantages of UWB communications include high data rate, low power, and multiple access communications. However, there are also some disadvantages to wideband communication, the most crucial of these being interference with coexisting systems.

2.1.2 Satellite Communications

Satellite communications are crucial for various technologies such as television, radio, and mobile (especially international) services. Today, satellites have enabled interconnectivity throughout the world – including enabling the Internet and distributing information [18]. These systems work 50,000 miles from Earth and operate for 15 to 18 years without human maintenance [18].

Conceptually, satellite communication systems are very similar to terrestrial systems. The key difference is that satellites have hundreds of beams covering a huge section of the Earth's surface, while terrestrial systems have minimal coverage. Technologically, beamforming becomes much more difficult when hundreds of beams are being handled [18].

The demand for wideband communications can be satisfied with satellite communications [18]. This would be true for all the applications currently supported by satellite communications, such as broadcasting and mobile services. Even so, there are still disadvantages to satellite communications, namely atmospheric phenomena and interference from coexisting systems.

2.1.3 5G Wireless Networks

5G wireless networks are among the most recognized communication systems. Although fourth generation (4G), the predecessor of 5G, provided mobile services nearly equivalent to wired connections, the 5G era required further advances to achieve a more efficient wireless experience. These advances include high speed, rapid response, high reliability, and energy efficiency [19].

Recall in the previous section that satellite communications use hundreds of beams to cover a large area. 5G networks, instead, have hundreds of base stations with small coverage, providing low latency and almost instant communication. This means that user equipment (UE) is seamlessly transferred from base station to base station. Base stations are oriented at a downtilt angle of $1°$ to $2°$ below broadside (horizontal) [15].

The increasing demand from new users and technologies (i.e., smart watches, autonomous cars, robots) requires a wideband signal that can support such traffic. Today, that demand for always-on connectivity is satisfied with 5G wireless networks. However, as a wideband signal, 5G networks still suffer from limited coverage (from an individual base station) and coexistence interference within the RF spectrum.

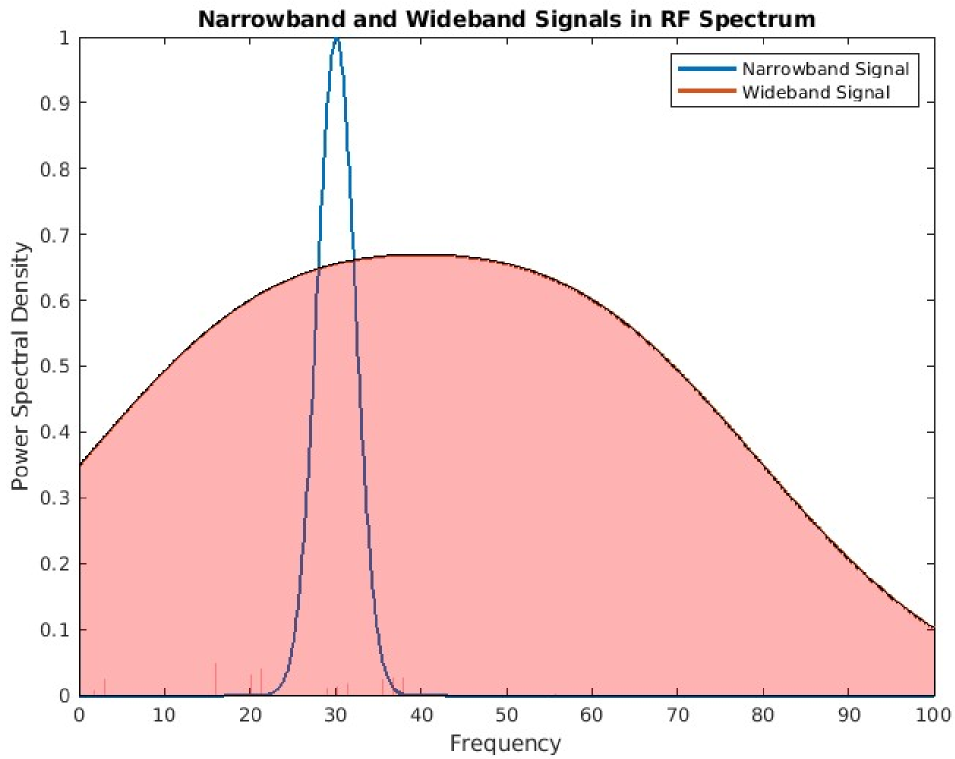

Figure 2.1: Visualization of narrowband and wideband interactions in RF spectrum. The wideband signal in red overlaps and envelops the narrowband signal in blue. This interaction causes distortion and loss in performance for the narrowband technology.

2.1.4 Wideband Communications and Radar

Radars are a technology that often operates in a narrowband fashion. That is, they have a narrow range of frequencies within the RF spectrum to transmit and receive their signal. This allows for lower power consumption and further propagation, but requires lower data rates. However, this also means they are susceptible to WBI.

As has been mentioned, the coexistence of many technologies in the RF spectrum leads to complications in the performance of these same technologies. Consider the interaction between a wideband communication system and a narrowband radar – they both operate in the same frequency band, as per FCC regulation, at the same time. Wideband communication transmissions are likely to leak into radar receivers, more so if we consider the large bandwidth that is sure to overlap with the radar's bandwidth. View Figure 2.1 for an example of this WBI. This interference is detrimental to radar as it litters the entire spectrum. The radar ends up overwhelmed by the WBI and thus must be removed for proper operation to continue.

2.2 Binary Phase Shift Keying

Binary Phase Shift Keying (BPSK) is a modulation technique commonly used in communication systems to transmit information. The symbols in a BPSK

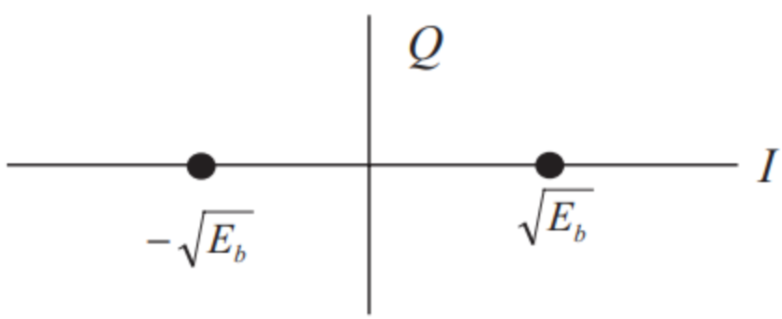

Figure 2.2: BPSK constellation diagram where $-\sqrt{E_b}$ is represented by a binary 0 and $\sqrt{E_b}$ by binary 1. Note that there is no Q component in a BPSK signal. Courtesy of [20].

signal modify the phase of the signal by 180 degrees (180°). These symbols are denoted with binary 0 or 1 to represent a phase shift of 0° and 180°, respectively. Phase modulation is suitable for communication channels that suffer from noise and interference, such as WiFi and Bluetooth. It is easier to understand this modulation scheme by visualizing it in the form of a constellation. Figure 2.2 is a constellation diagram of a BPSK signal, where the in-phase (I) and quadrature (Q) components are plotted on a two-dimensional plane. Mathematically, the BPSK signal is [20]:

$$s_{BPSK}(t) = \begin{cases} \sqrt{\frac{2E_b}{T_b}} \cos\left(2\pi f_{c,b} t + \theta\right) \quad 0 \leq t \leq T_b \qquad (binary \quad 1) \\ -\sqrt{\frac{2E_b}{T_b}} \cos\left(2\pi f_{c,b} t + \theta\right) \quad 0 \leq t \leq T_b \qquad (binary \quad 0) \end{cases} \tag{2.1}$$

where E_b is the energy per symbol, T_b is the duration of the symbol, and $f_{c,b}$ is the center frequency of the system.

Figure 2.3 shows the modulation process for generating a BPSK communication signal. The symbols change the phase of the carrier wave by 180°. The mixer, which is at the same center frequency, $f_{c,m} = f_{c,b}$, as the carrier wave, is mixed with the carrier wave, generating the transmitted wave. Since the carrier and the mixer waves have the same center frequency, mixing them results in constant values dependent on the phase of the two waves – a square wave. Note that this means that the transmitted wave is acutally a baseband representation of what is actually transmitted through the communications channel. A more detailed explanation of how this signal is generated is given in Section 4.1.1.

2.3 Sampling Theory

To process or store an analog signal, the signal must be saved digitally. The following section (Section 2.4) will dive into ADCs, which is a crucial piece of hardware that uses sampling to transform analog signals into the digital domain.

The simplest way to store an analog signal, $x(t)$, is to sample it at intervals of length T_s, so that $x(mT_s)$ values of the analog signal are sampled [21]. Generally, sampling provides an approximation of $x(t)$.

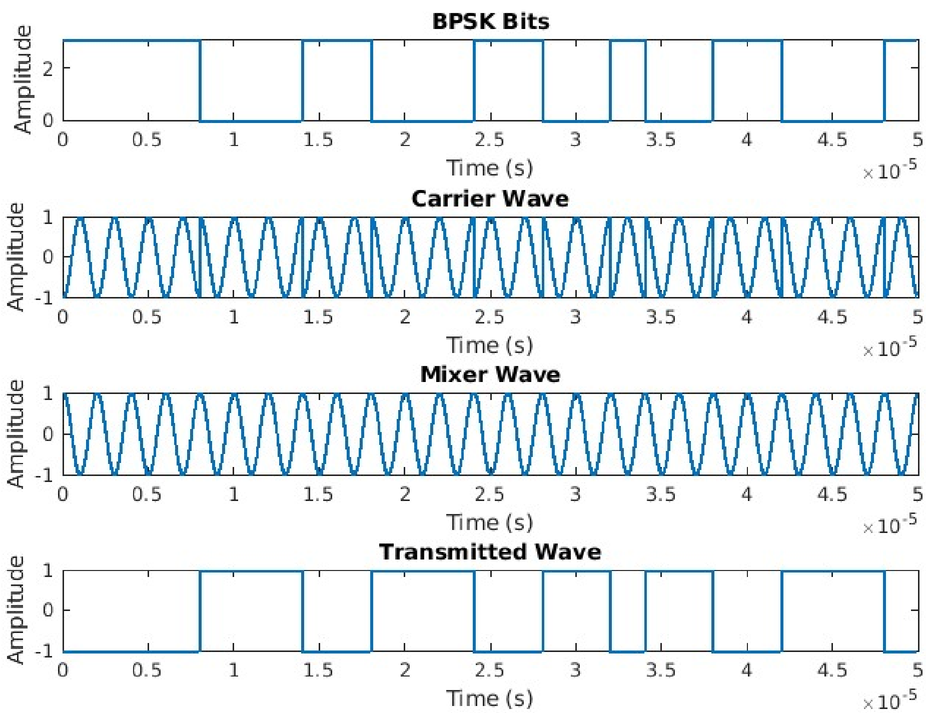

Figure 2.3: BPSK wave generation. The signals in order from top to bottom are: the BPSK phase terms, the carrier wave, the mixer wave, and the transmitted BPSK signal. The transmitted wave is a square wave since the carrier wave and mixer wave are at the same center frequency. This means that the transmitted wave depicted here is a baseband representation of what is actually transmitted.

2.3.1 The Shannon-Nyquist Theorem

The Shannon-Nyquist theorem, colloquially called the Nyquist theorem, is undoubtedly the most studied and influential sampling theorem in signal processing. Essentially, the theorem states that any signal, $x(t)$, bandlimited to $[-f_s/2, f_s/2]$

(where f_s is the sampling frequency for the signal) can be completely described by its samples $x(m/f_s)$ at rate f_s [22]. Moreover, $x(t)$ can be recovered from its samples.

Mathematically, for $x(t)$ to be perfectly recoverable, the sampling frequency, f_s, must be at least twice the highest frequency in the signal, f_{max}. View (2.2) for this inequality. Note that this inequality is commonly called the Nyquist criterion.

$$f_s \geq 2f_{max} \tag{2.2}$$

The minimal frequency that satisfies (2.2) is referred to as the Nyquist rate. In practice, sampling rates are usually much higher than the Nyquist rate. If the Nyquist theorem is not followed, complications and errors such as aliasing occur.

2.3.2 Undersampling

There are three main relationships that define how an ADC samples an analog signal: oversampled, critically sampled, and undersampled.

In practice, the sampling rate is often chosen such that the analog signal is being oversampled. An oversampled signal has a sampling rate that is much higher than required by the Nyquist theorem. However, there is a balance to consider. Oversampling means that more samples are being taken and stored, and thus more processing power (ADC capability) and storage space are required.

A critically sampled signal is sampled at the Nyquist rate (exactly $2f_{max}$). Therefore, all aspects of the Nyquist theorem are met without additional computational costs or complexity. Critically sampling a signal is not common in practice, as was described above. However, for simulations and understanding concepts, perfect sampling is a practical choice.

An undersampled signal violates the Nyquist criterion. The sampled signal ends up aliased and the original analog signal cannot be reconstructed. Undersampling has massive consequences, including the loss of information about the analog signal.

To fully understand the consequences of undersampling, one must first understand the implications of aliasing [23]. Consider a simple sine wave in the time domain with a frequency f_a. The sampling frequency is set to a frequency f_s where $f_a < f_s < 2f_a$ – the Nyquist criterion is violated. The pattern of the samples produces an aliased sine wave at a frequency $f_s - f_a$.

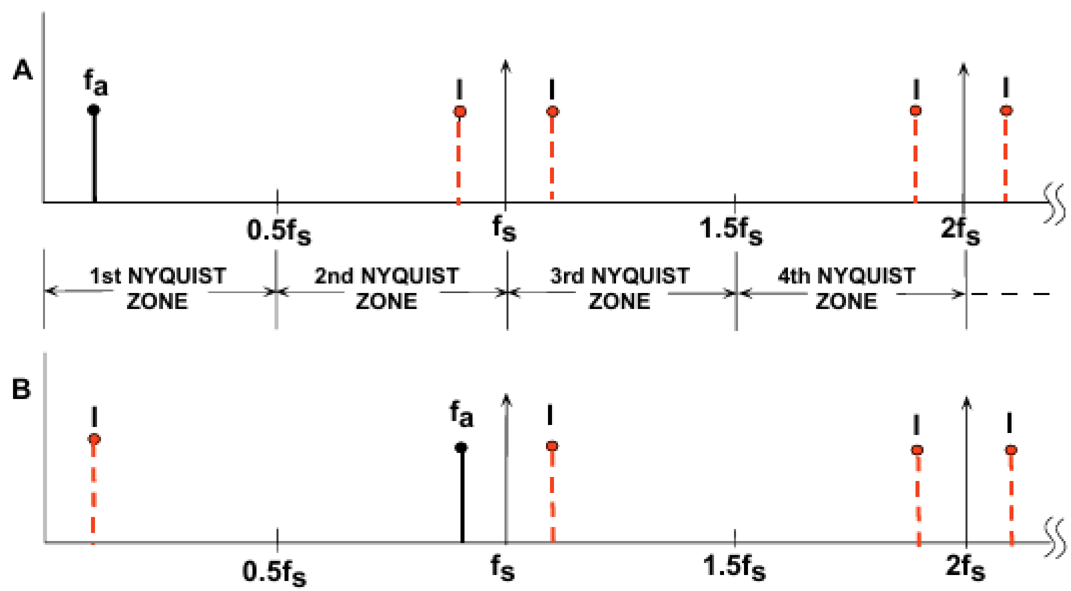

Figure 2.4: Images for analog signal with frequency f_a sampled at a rate of f_s. The aliases fall at $|\pm K f_s \pm f_a|$. If the value of $f_s < f_a$, the images will fall in the first Nyquist zone and the signal will be aliased. Courtesy of [23].

Now, when a signal is sampled in accordance with the Nyquist theorem, the frequency domain of the sampled signal shows aliases or images of the original signal centered at multiples of f_s [23]. The frequency spectrum is divided into an infinite number of Nyquist zones, each of width $f_s/2$. In practice, only the first Nyquist zone, from direct current (DC) to $f_s/2$, is preserved. Going back to the previous sine wave, one of the images fall at $f_s - f_a$ which is inside the first Nyquist zone. The unwanted signal produces a spurious frequency component in the first Nyquist zone. See figure 2.4 for a visualization of this concept.

In the work presented in this thesis, the ADC will undersample the BPSK signal, $x(t)$. This causes two main consequences: each sample will contain more than one symbol and it is likely that one symbol will be in more than one sample. Note that the digital output is proportional to the symbols within that one sample and their values. Due to these complications, additional processing is necessary to fully demodulate the signal and recover all the symbols that were originally transmitted. Chapter 4 explains this novel post-processing algorithm.

2.4 Analog-to-Digital Converters

ADCs are electronic devices that measure analog signals, which are characteristic of most real-world phenomena, and convert them to a digital representation (i.e., binary code) for digital processing [23]. Simply, an ADC allows digital systems, such as computers, to interact with real-world analog data. A digital-to-analog converter (DAC) does the opposite functionality.

2.4.1 ADC Architectures

All ADCs work in a similar way and with the common goal of converting analog data to digital data. The basic flow of any ADC is as follows. The ADC samples the analog signal at uniform time intervals – this is an ADC sample. The analog sample is then converted to its digital representation. Every ADC architecture does this differently, depending on use and application. The speed of the ADC is measured in $samples/s$ (commonly in $Msamples/s$ or MSPS) and determines the fastest sampling capability of the ADC (how fast the ADC can convert). The resolution of the converter is determined by the number of binary bits used to represent each ADC sample, where a larger number of bits translates to better resolution. Notably, the sampling process must be in accordance with the Nyquist criterion (see Section 2.3). There is also inherit quantization error due to the finite resolution of the converter. This error determines the maximum dynamic range of the converter.

The most basic ADC is called a comparator or a 1-bit ADC [23]. Its input is converted to a logical 1 or 0 depending on if the analog value is above or below a predetermined reference voltage, respectively. A comparator is a crucial part of any and all ADC architectures.

There are three main ADC architecture categories: high speed, counting and integrating, and $\Sigma - \Delta$ – each with specific features that make them adequate for different applications. However, the $\Sigma - \Delta$ (also called $\Delta - \Sigma$) ADC architecture is the focus of this thesis and will be explained in a separate section (Section 2.4.2).

High Speed ADCs

High speed ADCs include ADCs such as flash converters, successive-approximation, and pipelined [23]. These ADCs have high sampling rates, hence the "high speed". Applications usually lie in real-time digital signal processing, such as broadband communications.

Flash converters are the fastest type of ADC and use a combination of resistors and comparators. Specifically, it has 2^N resistors and $2^N - 1$ comparators (where N is the number of bits in the ADC) [23]. The first flash converter was developed in 1921 [23].

Successive approximation ADCs are most popular for data acquisition applications [23]. The basic architecture involves a sample-and-hold input, where the signal is constant during the conversion cycle. The sampling rate of these ADCs is in the MHz range [23]. Today, this ADC architecture is commonly seen in low-power integrated circuits.

Pipelined ADCs are commonly used for truly high-speed applications, where sampling rates are 65 MSPS or even 170 MSPS [23]. This is due to the "pipelined" capability of this type of ADC, where one stage is able to process data from the previous state at any given clock cycle [23]. Today, low-power complimentary metal-oxide conductors (colloquially, CMOS) are a common application of this architecture.

Counting and Integrating ADCs

Counting-based ADCs are not well suited for high speed applications – unlike the ADC architectures described above. They are ideal for high resolution, low frequency applications, especially if combined with integrating techniques [23].

In 1952, voltage-to-frequency converters (VFCs) were developed using an oscillator whose frequency was linearly proportional to a control voltage [23]. It is commonly seen in telemetry applications since the VFC is cheap, small, low-powered, and with high resolution. Unlike other ADCs, their output is a pulse stream, making them useful in a wide range of applications [23].

Dual slope ADCs were truly a breakthrough when they were first developed in 1957 due to their high resolution capabilities for applications such as digital voltmeters [23]. Dual slope integration has many advantages, including conversion accuracy being independent of capacitance and clock frequency and the rejection of noise frequencies in the analog domain. Today, multislope ADCs have been developed with the same core architecture as the dual slope.

2.4.2 $\Sigma - \Delta$ ADCs

$\Sigma - \Delta$ ADCs (as they will be referred to for the rest of this thesis) are used for precision and instrumentation, such as for audio signal processing. These ADCs require high resolution but have lower, more effective, sampling rates. Figure 2.5

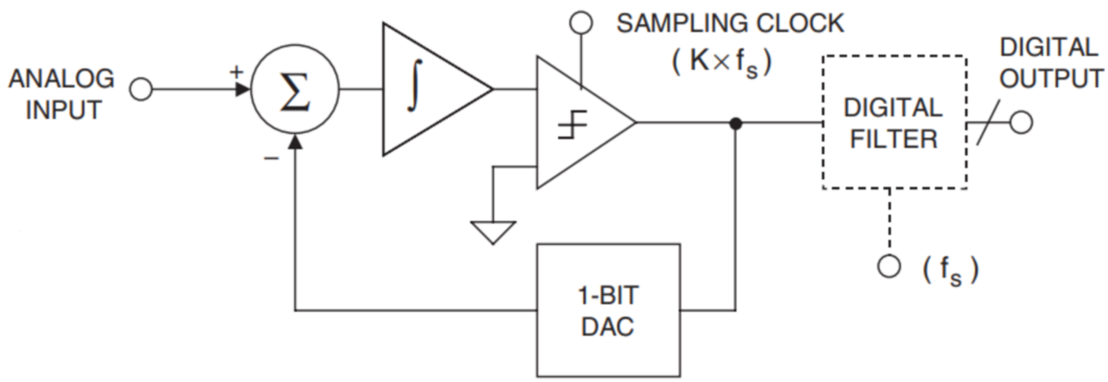

(a) Single bit $\Sigma - \Delta$ architecture.

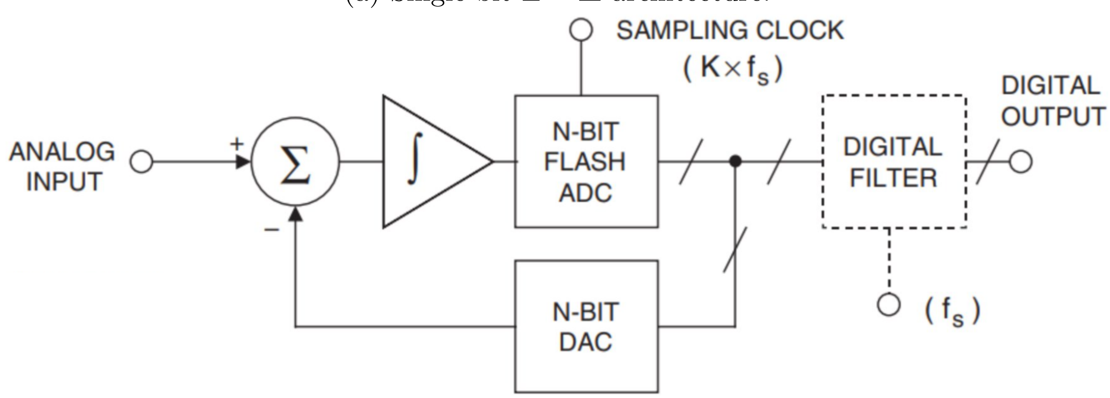

(b) Multibit $\Sigma - \Delta$ architecture.

Figure 2.5: Single bit (a) and multibit (N-bit) (b) $\Sigma - \Delta$ ADC architectures. The main difference between these two diagrams is that the single bit architecture needs only a comparator to digitize the signal while the multibit architecture requires an N-bit flash ADC. Courtesy of [23].

shows a single bit and multibit (2.5a and 2.5b, respectively) first-order $\Sigma - \Delta$ ADC architecture. For this thesis, the focus will be on a 12-bit $\Sigma - \Delta$ ADC, which emulates what is seen in Figure 2.5B. Note that a multibit ADC will be more comparable to its input analog signal.

There are four key concepts in a $\Sigma - \Delta$ ADC: oversampling, quantization noise shaping, digital filtering, and decimation [23]. Oversampling allows noise to be distributed over a wider bandwidth DC using an oversampling factor, improving the resolution and relaxing analog anti-aliasing filter requirements [23]. Applying a digital lowpass filter removes much of the quantization noise but maintains the desired signal. Decimation is the process of keeping every Kth result and discarding the rest of the signal. Note that, decimation does not occure if the analog signal is oversampled by as much or more than the decimation ratio.

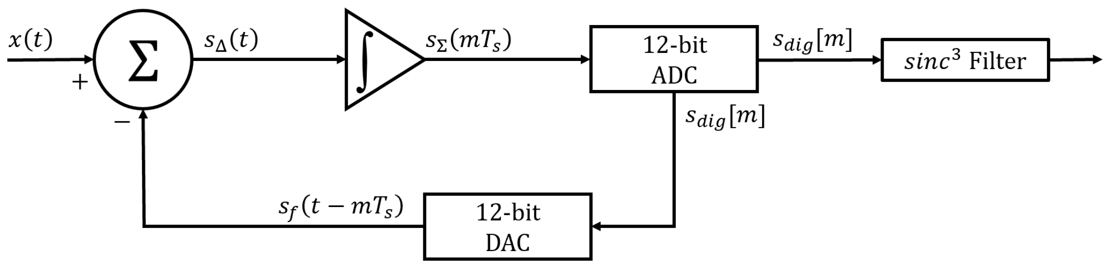

Figure 2.6: 12-bit $\Sigma - \Delta$ ADC architecture with variables. Recall Figure 2.5b for the general version of this ADC. Refer to this figure for Chapter 4.

Variable	Unit	Description
$x(t)$	V	Analog input signal
$s_\Delta(t)$	V	Constant analog signal, Δ output
$s_\Sigma(mT_s)$	V	Constant analog signal, Σ output
$s_{dig}[m]$	12-bit	Digital signal, ADC output
$s_f(t - mT_s)$	V	Feedback analog signal, DAC output
T_s	s	Duration of one ADC sample
T_b	s	Duration of one symbol
N	-	Number of bits in resolutions
M	-	Number of ADC samples

Table 2.1: Variables in a 12-bit $\Sigma - \Delta$ ADC as corresponds to the diagram shown in Figure 2.6.

The $\Sigma - \Delta$ ADC operates as follows (and will be simulated in this way in Chapter 4). Refer to Figure 2.6 and Table 2.1 for the basic operation and variable interpretation.

Due to the properties of ADCs, the input signal, $x(t)$, is shifted to be completely positive, disregarding noise. In general, analog signals are generated centered around 0. Thus, this shift implies that the ideal minimum value is 0 and the ideal maximum value is twice the amplitude.

First, a sample of $x(t)$ with a duration of T_s is sent to Δ modulation, marked with a Σ in Figure 2.6. Although it may seem counterintuitive, Δ modulation refers to the change in value between consecutive samples, much like how the Δ symbol is often used in mathematical practice [23]. Similarly, Σ represents the integration that occurs. Simply, a $\Sigma - \Delta$ ADC takes a difference (Δ) and then integrates (Σ) it [23].

As stated above, Δ modulation performs a subtraction between two analog signals. The first is the ADC sample taken from the input signal and the second is the feedback signal, $s_f(t - mT_s)$. Note that for the first sample, the value of the feedback signal is 0, as nothing has passed through the ADC yet. The output of Δ modulation is $s_\Delta(t)$, a constant value analog signal.

The signal then undergoes integration, a Σ variation to Δ modulation. The output, $s_\Sigma(t)$, cumulatively sums the integration outputs of all the ADC samples. This is where first-order quantization noise shaping occurs. In Figure 2.6, note that $s_\Sigma(t)$ is shown as $s_\Sigma(mT_s)$ to represent the ADC sample for which this integration corresponds.

An N-bit ADC has 2^N possible discrete values. Therefore, a 12-bit ADC converts the analog value ($s_\Sigma(mT_s)$) to one of 4096 discrete values. This is the resolution of the ADC. The more bits an ADC uses for its digital representation, the more the digital values will correspond to the analog signal. Recall that the digital representation is binary, where one sample is represented by, in this case, 12 bits. If the value of $s_\Sigma(mT_s)$ is larger than twice the amplitude or less than 0, the value will be rounded to be within the finite resolution.

There is also quantization error at this step in the $\Sigma - \Delta$ ADC. Since there is a finite number of states the ADC can choose from – 4096 in this case that all correlate to a digital representation (that is 12 bits long) – the continuous voltage in $s_\Sigma(mT_s)$ has to be rounded to the nearest discrete state. This means that if $s_\Sigma(mT_s)$ is between two voltage states, the voltage is rounded to the nearest state. Therefore, error occurs between the true analog value and the ADC value which cannot be recovered.

The digital signal, $s_{dig}[m]$, is split into two directions: the third-order sinc ($sinc^3$) filter and the feedback loop. The $sinc^3$ filter smooths the output of the ADC. Although a different filter could be applied here, the $sinc^3$ filter is the most common in practice. If the input signal was oversampled, then the output signal undergoes decimation after digital filtering. The digital value is then stored or sent to a host computer. Through the feedback loop, the digital value $s_{dig}[m]$ is converted back to an analog signal via a 12-bit DAC. The DAC converts the binary code into the analog signal, $s_f(t)$, that is subtracted from the next ADC sampled (Δ modulation). Essentially, $s_f(t)$ is the quantized form $s_\Sigma(mT_s)$. Note that in Figure 2.6, $s_f(t)$ is shown as $s_f(t-mT_s)$ because it represents the previous ADC sample with respect to the current ADC sample that is being processed in Δ modulation. This continues until the entire analog signal has been digitized.

A more detailed mathematical model of the 12-bit $\Sigma-\Delta$ ADC will be described in Chapter 4.

Chapter 3

5G Interference on Radar Altimeters

The main focus of Chapters 3 and 5 is understanding the interactions of 5G transmissions (signals) with radalt receivers for terrestrial only communications (ignoring aerial). This chapter will cover the necessary background to fully understand this OOB interference. This will include information on radar (or radio) altimeters (from here on called radalts) in Section 3.2, 5G transmissions in Section 3.3, and the intersection between these two subjects in Section 3.4.

3.1 3.7 to 4.2 GHz and 4.2 to 4.4 GHz Frequency Bands

The 3.7 to 4.2 GHz frequency band, also known as the US n77 band, is currently being used for fixed-satellite services. Recently, it has also been made available to 5G, a common wireless network and wideband technology. In the United States, phones and other UE are associated with 5G.

The 4.2 to 4.4 GHz is an exclusive frequency band reserved for radalts worldwide. This band is one above (and adjacent to) the US n77 band described above. In other words, the 3.7 to 4.2 GHz and 4.2 to 4.4 GHz frequency bands have adjacent spectrum.

For clarity, the 3.7 to 4.2 GHz frequency range and the 4.2 to 4.4 GHz frequency range will also be referred to as the 5G band and radalt band, respectively. Any other frequency bands will be specifically stated.

3.1.1 Radalt Interference Overview

Radalt receivers are designed with front-end filtering to decouple them from other radars operating near them in frequency (from 3.7 to 4.2 GHz) [15]. Most radalts perform better with a slow rate of frequency-dependent roll-off in their front-end filtering, which leads to roll-off in these lower frequencies. However, this filtering is not necessarily effective since the 3.7 to 4.2 GHz spectrum was historically quiet. It was not until recently that the 3.7 to 4.2 GHz band was opened for more active and intense use (i.e., 5G networks).

Today, relatively high-powered 5G networks – commonly in the 3.7 to 3.98 GHz range within the 5G band – introduce interference into the RF spectrum due to their demand and wideband characterization. This interference can otherwise be described as a coexistence problem between adjacent frequency bands. 5G transmitters and radalt receivers in adjacent spectrum, 3.7 to 4.2 GHz and 4.2 to 4.4 GHz, respectively, are one pressing example of a larger set of such adjacent-band electromagnetic coexistence situations.

The interference from 5G emissions may affect radalt receivers in one of two possible ways. One is due to unwanted emissions within the radalt band. The second is due to coupling of 5G power into radalt receivers in the 3.7 to 3.98 GHz band, which is for 5G transmitters. More details on this crucial interference problem are provided in Section 3.4.

3.2 Radar Altimeters

The first radalts used by the United States were deployed in World War Two. They are commonly used in military applications, but are also seen in commercial aircraft. Their purpose is to detect the distance between an aircraft and the terrain below it. This data provides information that is used for low-elevation flights, landings, and low-visibility situations. Today, radalts worldwide are exclusively allocated the 4.2 to 4.4 GHz band as a protected safety-of-life service [15].

Radalts can be pulsed or frequency-modulated continuous wave (FMCW). Generally, pulsed radalts are found in military aircraft while FMCW radalts are found in civilian aircraft. Pulsed radalts work by conventional out-and-back translations of transmitted pulses and echo returns [15]. FMCW radalts operate on the principle of beating the transmitted waveform against the identical echo [15]. The focus of this thesis will be on FMCW radalts, which will be further discussed in Section 3.2.1.

3.2.1 Linear FMCW Radar

A simple FMCW radar architecture is depicted in Figure 3.1. Although there may be differences from radar to radar and application to application, the basic outline is given below. See Section 3.2.2 for more details on radalt architectures specifically.

FMCW radars can be separated into two distinct parts: the frequency modulation and the continuous wave (CW). It is easier to begin with a simple CW architecture and then incorporate the frequency modulation.

The most common applications of CW radars are in low-power short-range applications that mainly require velocity measurements [24]. CW radars require a transmitting antenna and a separate receiving antenna (bistatic architecture). This is because CW radar, by definition, never stops transmitting or receiving, they are both continuously on. This is a great benefit of CW architectures, as the average power is not limited by a duty cycle [24]. See Figure 3.2.

However, CW radars cannot measure range due to the transmit and receive signals being indistinguishable. The frequency of the transmit signal is constant, which causes the receive signal to be identical to the transmit signal, only shifted in time.

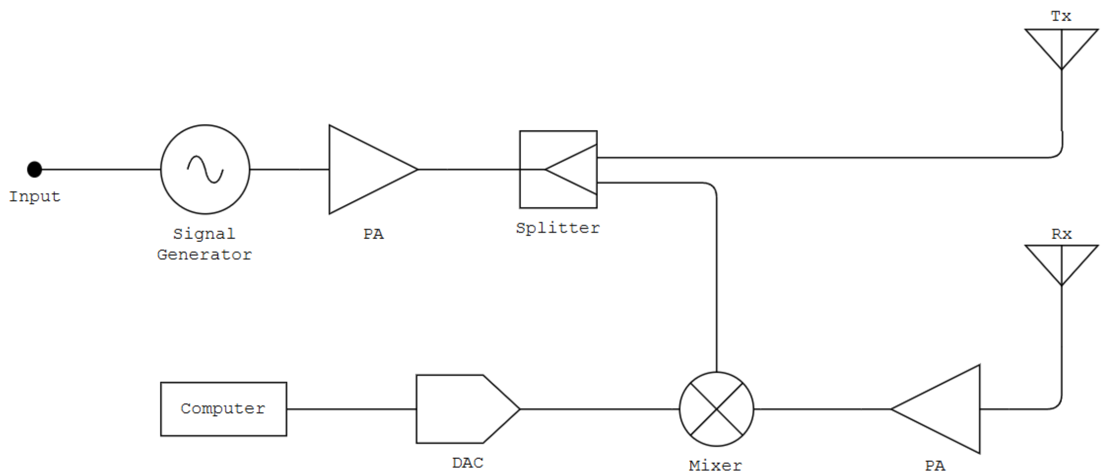

Figure 3.1: Basic FMCW radar architecture. The top part of the diagram shows the steps to generate the transmitted FMCW signal. The bottom part of the diagram shows the steps after receiving the signal.

By modulating the frequency of the signal over time (frequency modulation), the range and velocity of the targets is measurable. This is why radalts use FMCW radar, as their purpose is to detect the distance a aircraft is from the ground (i.e., range).

The expression in (3.1) is the complex form of one sweep of a linear FMCW waveform [24]. This repeats every T seconds, forming a continuous wave. Note that with no frequency modulation, this is simply a CW radar. With frequency modulation radars are able to easily measure range.

$$x(t) = \exp\Big[j\Big(2\pi F_t t + \pi\frac{\beta}{T}t^2\Big)\Big], \quad 0 \leq t \leq T \tag{3.1}$$

where F_t is the starting frequency of the sweep, β is the bandwidth, T is the

FMCW sweep interval. Note that $1/T$ is the sweep rate.

$$F_i(t) \equiv F_t + \frac{\beta}{T}t \quad Hz, \quad 0 \leq t \leq T \tag{3.2}$$

A closer look at the sweep gives us (3.2) [24]. The frequency sweeps linearly

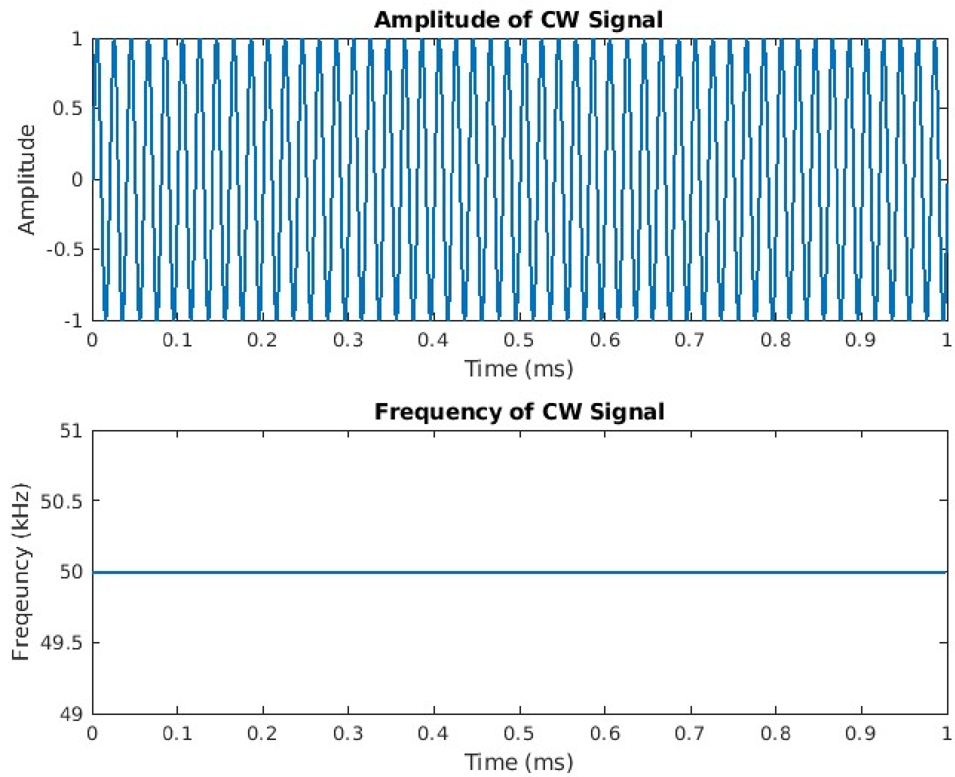

Figure 3.2: CW waveform with amplitude (top) and frequency (bottom) as a function of time. In a CW waveform the frequency is constant.

from F_t to $F_t\beta$ Hz in T seconds. In other words, the signal linearly increases its frequency for the duration of the sweep interval, repeating this same sweep continuously. One well known frequency modulation technique is linear frequency modulation (LFM) [24]. Within LFM, there are different modulation techniques, one of the most common and the one that will be detailed here is sawtooth modulation (or a chirp). Figure 3.3 illustrates this concept (with an upsweep chirp).

In practice, the sawtooth wave in Figure 3.3 can be reversed, where the upsweep

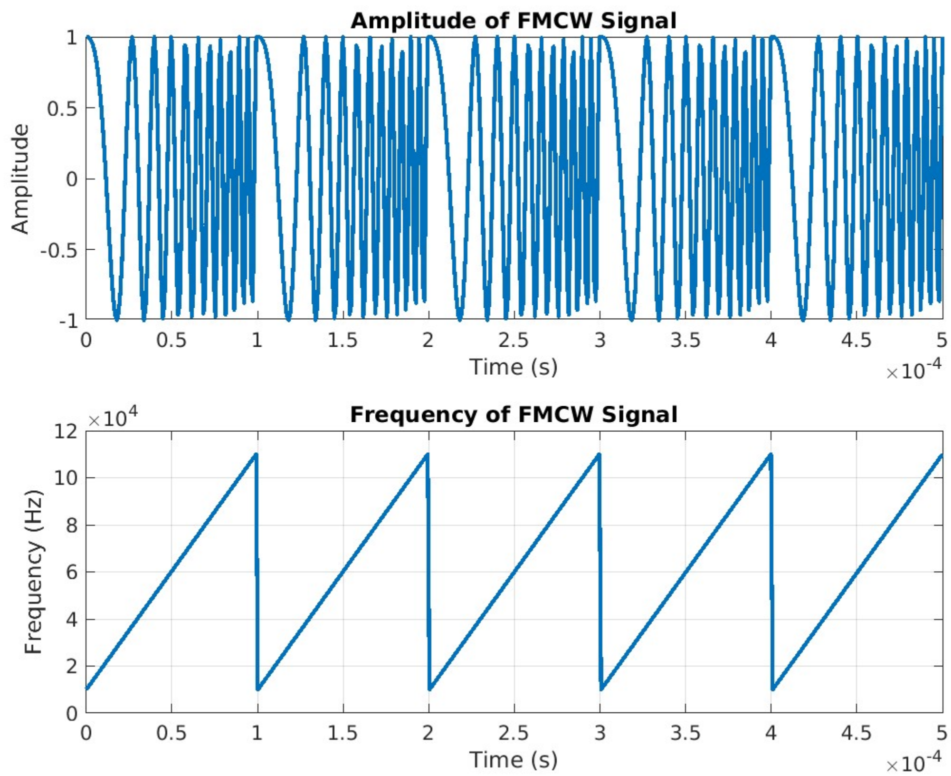

Figure 3.3: FMCW waveform with sawtooth modulation (LFM) with amplitude (top) and frequency (bottom) as a function of time, Note the differences between this figure and Figure 3.2, which has no frequency modulation.

becomes a downsweep with a simple change of sign in the quadratic phase term (see (3.1)) [24]. Both sawtooth waves are used in practice.

The chirp, seen in Figure 3.3 (bottom), can be configured in a theoretically unlimited number of ways. There are three main parameters that can be altered for specific performance requirements (note that there are other configurable aspects to FMCW radar): initial frequency, F_t, bandwidth, β, and sweep interval, T. Recall (3.1) and (3.2). Changing the initial frequency changes where in the RF spectrum the radar operates. In the case of radalts, the initial frequency could be anywhere in the radalt band as long as the final frequency is still within the band bounds. Adjusting the bandwidth affects how much frequency we cover in a singular sweep, essentially the difference between the initial frequency and the final frequency. The bandwidth is inversely proportional to the range resolution, given in (3.3).

$$\Delta R = \frac{c}{2\beta} \tag{3.3}$$

Changing the sweep interval, as the name states, changes the duration of a sweep. This value is inversely proportional to the maximum unambiguous velocity that can be detected by the radar. However, note that FMCW radars cannot detect velocity with sawtooth modulation. With these parameters, the FMCW radar can be configured for a multitude of scenarios and requirements. In the case of radalts, we expect the most critical spec to be range resolution (and thus bandwidth), as precise range measurements are a key performance metric.

Now, with FMCW, at any point in time there is a transmit signal and a receive signal. As was mentioned above in the CW explanation, the transmit and receive signals are identical, except that the receive signal is delayed in time. Looking at the same moment in time, the transmit signal and the receive signal are at different frequencies. The difference in frequency between the two signals is called the beat frequency. See (3.4).

$$f_{beat} = |f_{tx} - f_{rx}| \tag{3.4}$$

The beat frequency is crucial for finding the range of the target. With it and the slope of the sweep (the bandwidth over time), the range of the target can be found using (3.5).

$$R = \frac{c\Delta t}{2} = \frac{cTf_{beat}}{2\beta} \tag{3.5}$$

where Δt is the time delay between the transmit and receive signal. Note that this is the basic equation for a stationary target. If we continuously take these range measurements, the radalt can continuously measure the distance between the aircraft and the ground below it.

Matched Filtering

The matched filter is one of the most popular filters in signal processing as it is the optimal linear filter for maximizing the signal-to-noise ratio (SNR) [24]. The filter works on the basis of the matched condition: where the receiver filter response is matched to a particular signal waveform. The impulse response is calculated by [24]:

$$y(t) = \int_{-\infty}^{\infty} x'(s)h^*(t-s)ds = \int_{-\infty}^{\infty} x'(s)x^*(s+T_M-t)ds \tag{3.6}$$

where $x'(t)$ is the received signal, $x(t)$ is the transmitted waveform, and T_M is the arbitrary time at which the SNR is maximized.

In practice, the autocorrelation, the correlation of a signal with a delayed copy of itself, of the transmitted signal is often necessary. The autocorrelation can be found by applying the matched filter to the transmitted signal itself. Essentially,

$$y_{ac}(t) = \int_{-\infty}^{\infty} x(s)x^*(s+T_M-t)ds \tag{3.7}$$

Stretch Processing

Stretch processing, as defined by [24], is a specialized technique for matched filtering of wideband LFM and FMCW waveforms. Its main benefit is for applications where fine range resolution is necessary over a shot-range window. Stretch processing makes a trade-off between the sampling rate and sampling time: a lower rate but for a longer data collection time. It is implemented in the analog domain (before going through the ADC). For radalts, stretch processing is essential, so a large bandwidth can be used and a fine range resolution can be obtained (recall (3.3)).

The following steps describe stretch processing as applied to FMCW. First, the transmit signal is mixed with the received signal as per (3.8). This results in a beat frequency signal. The windowing is an optional step, which has chosen to be ignored in Section 5.3 but is denoted here for completeness.

$$b(t) = x'(t) * x^*(t) \tag{3.8}$$

where, like with the matched filter equations, $x'(t)$ is the received signal and $x(t)$ is the transmitted waveform.

The frequency spectrum is found by applying the fast Fourier transform (FFT), as seen in (3.9). Note that applying additional zero-padding improves frequency resolution.

$$B(f) = \mathcal{F}\{b(t)\} \tag{3.9}$$

Note that in ideal conditions, the matched filter output and the stretch processing output have identical resolution, implying that neither process is superior. However, as applications and situations vary, the choice between the matched filter and stretch processing becomes more crucial.

3.2.2 Radalt Design

The main performance characteristics of typical radalts are described in Table 3.1.The differences in performance between the matched filter and stretch processing are seen in more detail in Chapter 5. The antenna characteristics, related to the hardware and physical attributes of radalts, are in Table 3.2. These tables are derived from those in [15].

Architecturally, radalts fall into three broad categories: homodyne, noncoherent heterodyne, and coherent heterodyne [15]. A homodyne architecture has

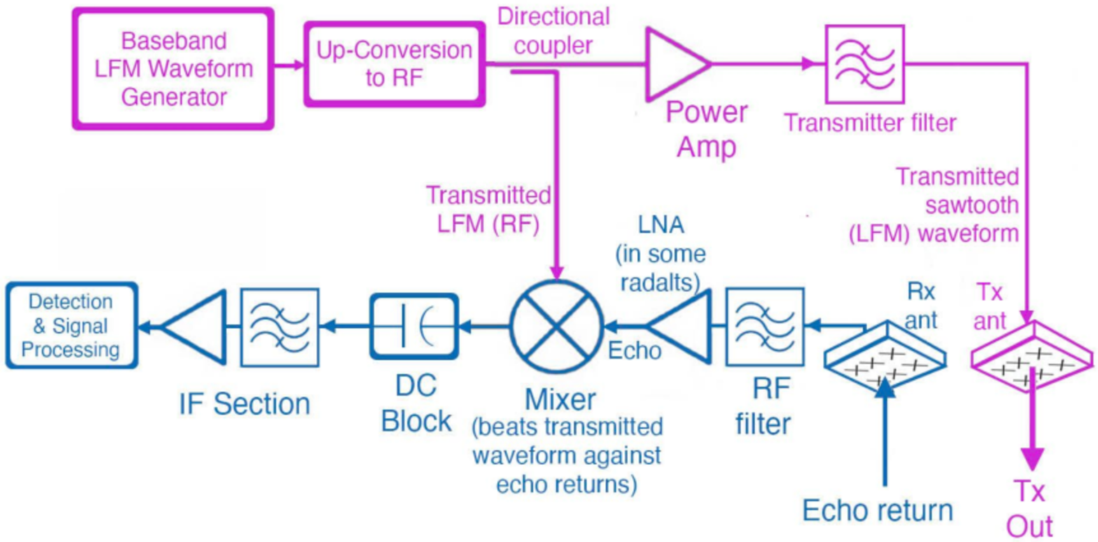

Figure 3.4: Homodyne architecture for radalts. The purple represents the transmission signal generation and the blue represents the receiving hardware. Courtesy of [15].

Parameter	Civilian Value	Military Value
Max. Reported Altitude	760 m to 2300 m	460 m to 15000 m
Altitude Accuracy	±0.46 m to ±0.91 m up to 30.5 m ±2% to ±3% from 30.5 to 152.4 m ±2% to ±5% above 152.4 m	±0.61 m to ±1.22 m up to 30.5 m ±2% to ±4% above 30.5 m
Pitch-and-roll Angle Range	±20° to ±40°	±20° to ±60°

Table 3.1: Typical radalt performance. Derived from the tables in [15].

Radalt Antenna Parameter	Value
Rx Bandwidth	100 Hz to 10 kHz
Tx-Rx Separation	0.9 m to 1.2 m
Tx-Rx Power Isolation	85 dB to 90 dB
Tx-Rx Orientation	H-plane coupled
Polarization	Linear

Table 3.2: Typical radalt antenna characteristics. Derived from the tables in [15].

no mixed-down IF stage and is soley used for FMCW radalts. The noncoherent heterodyne architecture uses two independent local oscillators (LO) with a mixed-down intermediate frequency (IF) and is used by some pulsed radalts. The coherent heterodyne architecture has a single local oscillator and a mixed-down IF and is used by pulsed and phase-shift-keyed models. Figure 3.4 is an example schematic for the homodyne architecture.

Note that the RF bandpass filter on the front-end of the receiver is a standard design feature, although the widths and roll-off rates of these filters vary from radalt to radalt. Varying the bandpass filter is proposed as a way to mitigate 5G interference.

3.3 5G Transmissions

The general problem is the 5G signal leakage into the radalt spectrum. This is due to the proximity of the 5G band and the radalt band. Due to how 5G operations occur, the 5G signal is indecipherable to a radalt receiver [15]. This is because of the supplemental information needed to demodulate (decrypt) the 5G signal. Thus, to the radalt receiver, the 5G signal appears as an uncorrelated, time-gated (70% duty cycle), and band-limited (100 MHz wide) Gaussian noise signal [15]. Note that even when data transmission needs are pushed to the limit (emissions are fully loaded), the radalt receivers will see no difference in the leaking 5G data, which is otherwise understood as interference, and thus this factor can be ignored.

Refer to Section 2.1.3 for more information on 5G networks.

3.3.1 Orthogonal Frequency-Division Multiplexing

OFDM is a digital transmission technique widely used in wireless systems, such as phones. OFDM enables high data rate transmissions by dividing modulated high-bandwidth signal carriers into many modulated narrowband subcarriers. Some key advantages and characteristics of OFDM, and why it is used in communications, are its orthogonality, robustness against intersymbol interference due to a cyclic prefix, and efficiency in being implemented via the FFT and inverse FFT (IFFT) [25]. The transmitted complex baseband OFDM waveform is given by [26]:

$$u(t) = \sum_{n=0}^{N-1} B[n] e^{j2\pi nt/T} I_{[0,T]} \tag{3.10}$$

where $B[n]$ is the symbol using the modulating signal and the nth subcarrier. A single OFDM symbol can be defined with the inverse discrete Fourier transform [25]:

$$x_b(t) = \frac{\mathrm{rect}\left(\frac{t-T_b}{T_b}\right)}{\sqrt{N_{sub}}} \sum_{k=0}^{N_{sub}-1} X_k e^{j2\pi kt/T_b} \tag{3.11}$$

where T_b is the symbol duration and N_{sub} is the number of subcarriers.

OFDM is a frequency-division multiplexing (FDM) method with the added property that all subcarrier signals are orthogonal (at 90°) to each other. Orthogonal subcarriers do not suffer from a phenomenon called crosstalk, where one channel creates an undesired effect on another channel. Orthogonality also allows for high spectral efficiency, where almost the entire available frequency band can be used.

OFDM uses a cyclic prefix between subsequent symbols, which introduces a guard interval in time [25]. This guard interval contains a copy of the last N_{CP} samples of the symbol, appended to the beginning of the symbol to create the cyclic prefix. The cyclic prefix does not carry data. The benefit of using a cyclic prefix is that it eliminates intersymbol interference and accommodates for simple frequency domain processing.

3.3.2 5G Multiple-Input Multiple-Output Array Design

5G base station transmitters (simply, 5G transmitters) use multiple-input multiple-output (MIMO) arrays. A key feature of MIMO arrays is their ability to form directed individual antenna radiation beams, maximizing and nulling desired and undesired UEs, respectively [15]. In addition, vertically arranged subarrays use phase control to form the beam at different elevations relative to broadside. Note that, generally, this elevation is in the negative direction (downtilt), as shown in Figure 3.5.

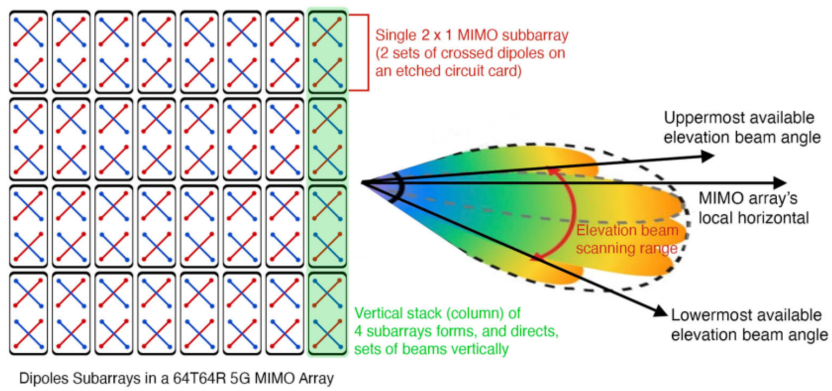

Figure 3.5: Example of MIMO array architecture and beamforming. This is the most common antenna array used by 5G signals. Courtesy of [15].

There are three antenna patterns that are considered in 5G MIMO applications: narrow, intermediate, and wide [15]. The narrow and intermediate patterns are commonly used for already established links with UEs. Additionally, the narrow pattern discriminates against undesired UE links. The wide pattern has low discrimination against undesired UEs and is used by new UEs to link and begin communication.

Although not shown, the elevation dimension provides significantly lower radiation power above the local horizontals than the main beams. However, at elevation angles between 10° and 20° above the local horizontal, there is a trend of relatively high sidelobes [15]. At all azimuthal widths, there are deep nulls from 60° to 90° above the local horizontal [15].

3.3.3 The Wireless Association

This section brings in the perspective of The Wireless Association, referred to as CTIA as it was previously known as the Cellular Telephone Industries Association. CTIA represents the U.S. wireless communications industry and the companies throughout the mobile ecosystem. The association includes wireless carriers, device manufacturers, suppliers, and app/content companies. The purpose of CTIA is to advocate for polices that foster wireless innovation and investment.

Below is CTIA's stance on the Federal Aviation Administration's (FAA) Airworthiness Directives, which directly impact the 5G transmitter and radalt receiver interference concerns raised by the FAA and explored in this thesis. CTIA claims that 5G base stations and radalts can coexist in their allocated spectrum bands, as has been designated by the FCC, without interference.

3.7 to 3.98 GHz 5G Networks

Early 5G networks (i.e. base stations) deployed for wireless use in the US operate in the 3.7 to 3.8 GHz range. That is, 5G transmitters and radalt receivers are separated by at least 400 MHz. Future models of 5G networks – which have already been built in the US and deployed in other countries – will operate up to 3.98 GHz, leaving a 220 MHz separation between them and radalt receivers [27]. As noted by the C-Band Order, put forth by the FCC on technical rules for 5G operations, this separation is enough protection for aeronautical services deployed in the radalt band. The OOB transmissions that occur near the radalt band are low enough to be insignificant, according to equipment vendors [27].

However, the FAA declared in their Airworthiness Directives, issued in December of 2021 (when the launch of the first 3.7 to 3.8 GHz 5G networks was scheduled), that radalts are not reliable if they experience interference from these new 5G transmitters. Due to these concerns raised by the FAA, 3.7 to 3.8 GHz 5G networks were delayed and precautionary measures were taken. These measures are to lower the power of 5G transmissions across the US, to effectively curtail operations in areas near airports and helipads (where radalts are most commonly used), and to postpone deploying the new 5G base stations, especially near airports [27]. In January 2022, the FAA approved 13 radalt models, allowing 78% of US commercial aircraft to use radalts in the vicinity of 5G transmitters [27].

CTIA requests that the Airworthiness Directives be retracted or, in the least, revised. CTIA's main concern is that the Airworthiness Directives are based on a study that has much evidence against it and that the FAA needs to be more transparent on its assessment of radalt models.

Current 5G Networks

CTIA, based on real-world 5G networks in other countries, claims that the FAA and their Airworthiness Directives are excessive and unsupported. Around 40 countries in Europe and Asia have 5G networks operating in the same frequency band as in the US, some even consistent with the limits dictated in [28]. None have reported any interference to radalts, which reside in the same 4.2 to 4.4 GHz band, or air traffic safety. Moreover, several countries operate in the same band but with higher power limits than the FCC permits, again with no negative effects on radalts. These real-world deployments of 5G networks in countries outside the US specifically deny the claims made by the FAA that 5G networks are dangerous to radalt performance. If anything, these deployments of 5G networks only help prove that the FCC's technical limits do, in fact, protect aeronautical services [28].

The Airworthiness Directives

The main document the FAA uses to support the Airworthiness Directives is the "Assessment of C-Band Mobile Telecommunications Interference Impact on Low Range Radar Altimeter Options" by the Radio Technical Commission for Aeronautics (RTCA) [29]. This report, according to CTIA, is highly flawed and unsound. Furthemore, CTIA states that the Aerospace Vehicle Systems Institute (AVSI), which collected the data the RTCA used in their report, also has a flawed methodology. Following are the reasons to support these claims.

First, the AVSI developed a "pass/fail criteria" that is more stringent than the one used by the FAA. The FAA requires that radalts detect altitudes within a 3% margin between 30.5 m and 152.4 m and a 5% margin above 152.4 m [27]. The AVSI determined that radalts with a mean error greater than 0.5% would be considered a failure. This high standard, higher than what is required by the FAA, yielded skewed results.

Second, the RTCA used the worst performing radalts as a representation of all radalts. The RTCA report separates radalts into three distinct categories: commercial air transport airplanes, all other fixed-wing aircraft, and helicopters. To determine whether interference from 5G transmissions is harmful, the RTCA chose the worst performing radalt to represent each category. The RTCA report goes on to state that radalts are impacted by 5G transmissions, a conclusion reached on this basis.

Third, the RTCA adopted unrealistic and unwarranted margins in their analysis of radalt performance. Incorrect assumptions such as too high loop loss or unnecessary cable loss skewed the results. The RTCA reports that, under these new margins, 5G is a risk to radalt performance.

Fourth, the RTCA models a worst-case landing scenario that is implausible. The scenario involves various signals from other radalts. This scenario is so harsh that most radalts failed even before the 5G signals were emitted. These conditions caused otherwise safe and reliable equipment to be determined as unreliable.

Five, the RTCA unrealistically models 5G transmissions. The RTCA does not take into account the realistic operation of 5G base stations. For example, they do not operate at 100% occupancy and form separate beams to serve multiple UEs (rather than a singular beam) [27]. The RTCA, thus, greatly exaggerates the impact of 5G networks.

By correcting these errors, the CTIA determined that several radalts were not affected by 5G signals, even in the unrealistic scenario designed by the RTCA. For further assurance, CTIA tested radalts in more realistic scenarios and with more realistic margins. These tests concluded that 5G networks would not affect radalts.

3.4 Potential OOB Interference

There are two possible scenarios in which 5G transmissions can interfere with radalt receivers: unwanted and intentional emissions. Both are a type of OOB interference. Simply, unwanted 5G interference is due to the 5G emissions and intentional 5G interference is due to the radalt.

3.4.1 Unwanted 5G Emissions

The definition of an unwanted emission be defined as unintentional radiation. This includes radiation that falls just beyond the intended frequency band, called OOB emissions. Any radiation further extended from the spectrum is coined spurious.

All 5G transmitters will produce some amount of unwanted emissions in the radalt receiver band. The potential interference in radalt receivers depends on how high the unwanted emissions are in the radalt band. Figures 3.6a and 3.6b demonstrate this scenario.

3.4.2 Intentional 5G Emissions

Intentional 5G emissions are the opposite of unwanted emissions. This form of interference occurs when the radalt receiver has too wide of a frequency-response range that it sees the 5G transmissions. Such a scenario is likely due to the low noise amplifiers (LNAs) in the radalt receiver being overloaded by the high transmitter power. Figure 3.6b demonstrates this scenario.

3.4.3 Interference Mitigation

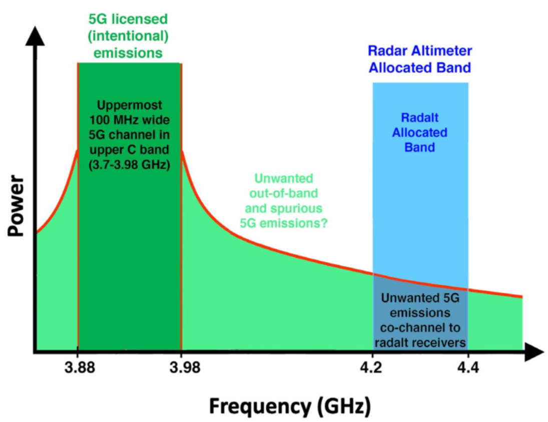

(a) Representation of 5G unwanted emissions leaking into radalt band.

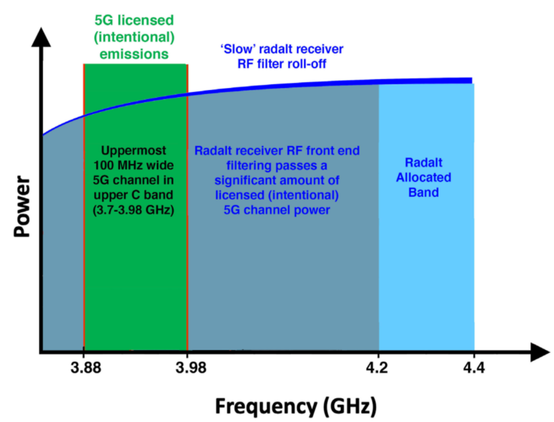

(b) of intentional 5G emissions being seen by radalt receivers.

Figure 3.6: Representation of 5G emissions and radalt altimeters and the possible OOB interference that could occur between these adjacent (in frequency) technologies. Courtesy of [15].

The ideal condition would be that unwanted emissions are low enough within the radalt band that the radalts are unaffected by this interference and for intentional emissions to go undetected by radalt receivers. Achieving adjacent-band coexistence requires effective RF filtering from both the 5G transmitter outputs and radalt receiver front-end inputs [15]. For 5G transmitters, filtering is ideally placed after the power amplifier (PA) output. For the radalt receivers, filtering would occur before the LNA input.

However, each potential interference scenario has its own mitigation solution. 5G transmitters need to be more effectively filtered for unwanted 5G emissions, while radalt receivers require more filtering for intentional emission mitigation. Thus, it is crucial to understand which scenario is (or if both are) transpiring and to what extent.

Chapter 4

Data Recovery in Communications and Radar

When radars convert analog signals at a lower rate than desirable, some information is lost (see Section 2.3). To recover lost data, a novel post-processing algorithm, named the Algorithm for Information Recovery (from here on referred to as AIR), is presented that allows for the demodulation and digitization of undersampled data. Using a post-processing algorithm, such as the one presented in

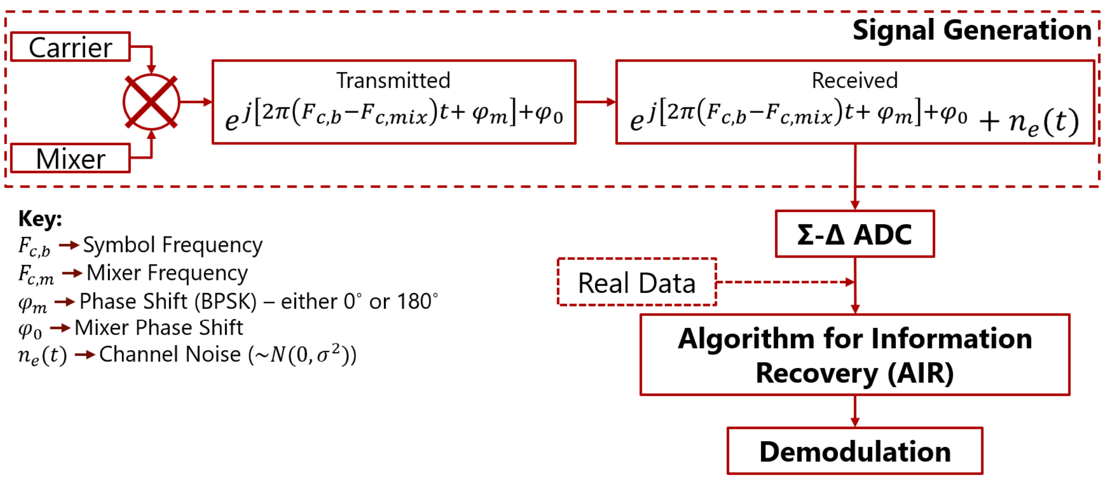

Figure 4.1: Flowgraph for undersampled data modeling. The steps are as follows: the carrier and mixer wave are mixed together to generated the transmitted signal, which is then received, digitized and undersampled via the $\Sigma - \Delta$ ADC, then, the lost information is recovered using the AIR, and finally, the recovered signal is demodulated.

this thesis, simpler, cheaper, and less complex ADCs can be used for high sampling rates and more accurate digitization of analog data.

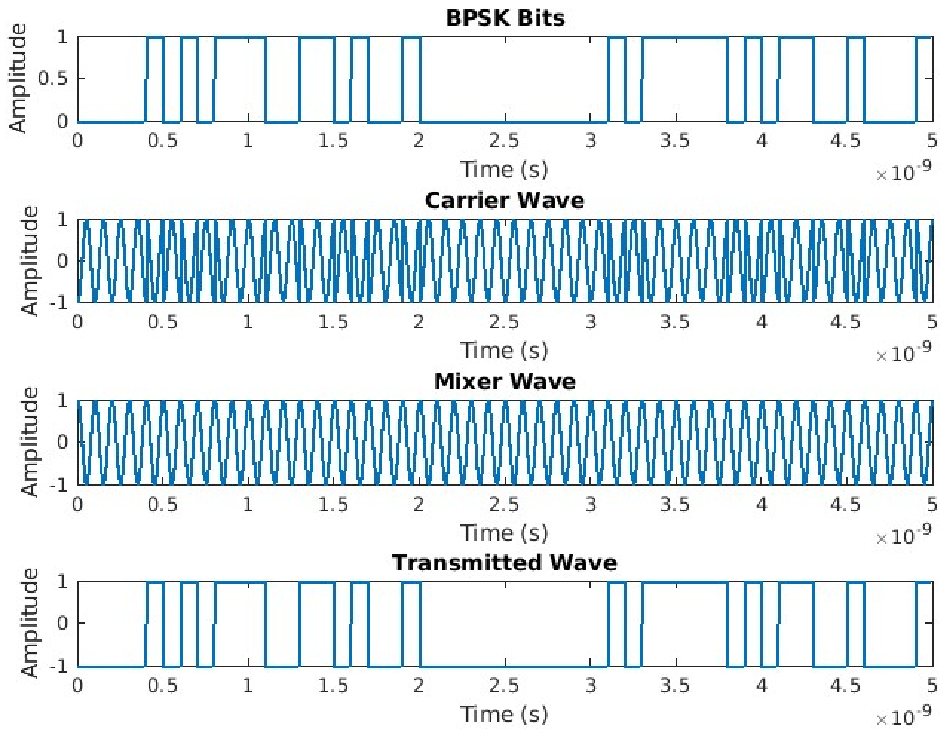

Figure 4.2: BPSK wave generation simulation. The signals in order from top to bottom are: the BPSK phase terms, the carrier wave, the mixer wave, and the transmitted BPSK signal. The transmitted wave is a square wave since the carrier wave and mixer wave are at the same center frequency. This means that the transmitted wave depicted here is a baseband representation of what is actually transmitted.

This chapter includes a detailed explanation of the AIR, a $\Sigma - \Delta$ ADC simulation in MATLAB, and simulation and experimentation results. It is organized as follows. Section 4.1 describes the signal generation and $\Sigma - \Delta$ ADC models. In Section 4.2, the AIR is introduced and explained. Sections 4.3 and 4.4 provide examples and results for tests carried out in simulation and with real data, respectively. Lastly, a summary of this chapter is found in Section 4.5.

4.1 Undersampled Data Modeling

There are three sections to modeling undersampled data: signal generation, $\Sigma - \Delta$ ADC, and demodulation (where the AIR occurs). Figure 4.1 provides an overview of the model. Each section of the model will be explained mathematically and with various figures.

4.1.1 Signal Generation

Gold codes are well suited for BPSK symbol generation. A Gold sequence is a type of product code in which two m-sequences are exclusive or'd (XOR) together [30]. This pseudorandom sequence of bits represents the phase shifts for the BPSK signal, ϕ_m, each with the same symbol duration T_b. Refer back to Section 2.2 for more information on BPSK.

Specifically, phase shifts affect the phase of the carrier wave. The mixer wave, which is similar to the carrier wave, maintains a constant phase. Note that other parameters, such as the center frequency of the carrier wave, $f_{c,b}$, and the center frequency of the mixer wave, $f_{c,m}$ can be altered to fit the needs of the designated simulation. If the center frequencies for the carrier and mixer waves are the same (view Figure 4.2), the transmitted signal will not oscillate and will actually represent the phase shifts. View (4.1) to (4.3).

$$e^{j(2\pi f_{c,b}t+\phi_m)} \tag{4.1}$$

$$e^{j2\pi f_{c,m}t} \tag{4.2}$$

$$c(t) = e^{j[2\pi(f_{c,b}-f_{c,m})t+\phi_m]+\phi_0} \tag{4.3}$$

where ϕ_0 is the channel phase shift and $c(t)$ represents the transmitted communications signal in baseband.

As with any system above absolute zero, whether analog or digital, the communication channal has noise. Therefore, the received signal contains additive white Gaussian noise. The received signal, $x(t)$ – called this because it is the signal received by the wireless communications system – is the input of the $\Sigma - \Delta$ ADC. Figure 4.3 and (4.4) show this.

$$x(t) = c(t) + n_e(t) \tag{4.4}$$

where channel noise is represented as

$$n_e(t) \sim \mathcal{N}(0, \sigma_n^2) \tag{4.5}$$

It should be noted that it is more realistic for the center frequencies of the carrier and mixer waves, $f_{c,b}$ and $f_{c,m}$, respectively, to be different values. However, in practice, the frequency of the carrier and mixer are known, thus setting them equal to each other allows them to cancel out, removing a step in the digitization processes.

4.1.2 $\Sigma - \Delta$ ADC Model

To preface, although the purpose of this chapter is to demonstrate the capabilities and purpose of the AIR, tests to ensure the correctness of the $\Sigma - \Delta$ ADC simulation were run. This will be discussed and shown briefly in this section.

Refer to Figure 2.6 from the previous chapter for the schematic of a 12-bit $\Sigma - \Delta$ ADC, which is the reference for the MATLAB simulation, and to Section 2.4.2, which provides more information on this type of ADC architecture.

The ADC takes a sample of the analog signal, $x(t)$, of duration T_s. The duration of the sample is the inverse of the sampling rate of the ADC, f_s. The

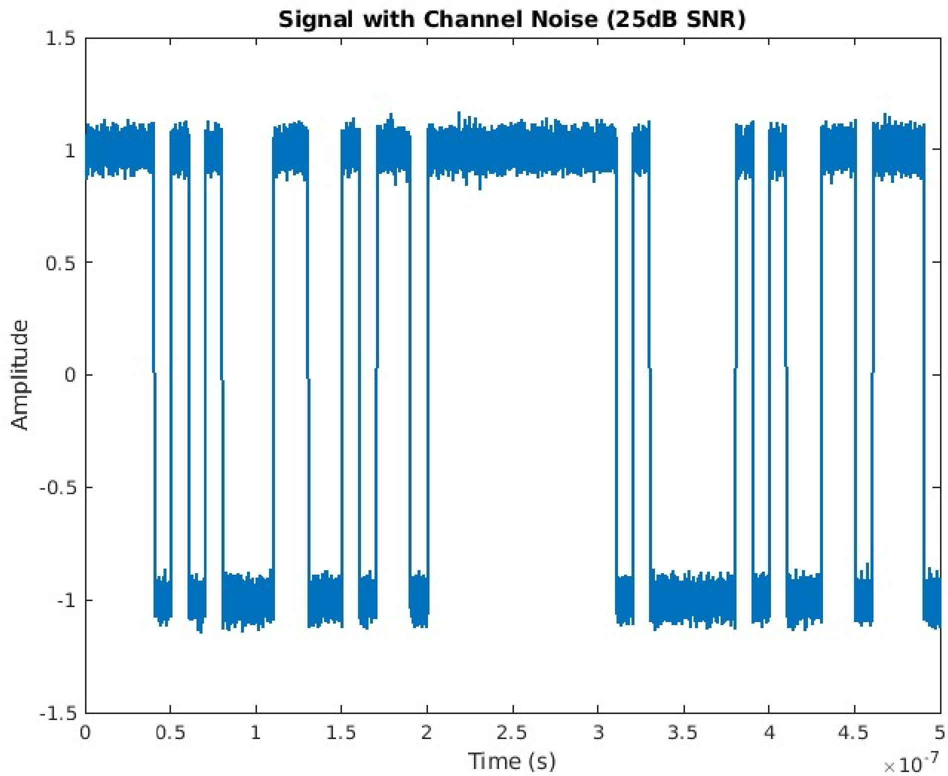

Figure 4.3: Received BPSK signal with 25 dB of added channel noise. This signal is the input for the $\Sigma - \Delta$ ADC. Recall the bottommost plot in Figure 4.2 to note the differences between the transmitted and received waves.

relationship in (4.6) – based on the frequency rates (or durations if inverted) of the symbols and samples – defines whether the ADC is undersampling, critically sampling, or oversampling.

$$R = \begin{cases} \frac{f_b}{f_s} > \frac{1}{2} & (undersampling) \\ \frac{f_b}{f_s} = \frac{1}{2} & (critically\ sampling) \\ \frac{f_b}{f_s} < \frac{1}{2} & (oversampling) \end{cases} \tag{4.6}$$

where R gives the proportion of the rate of the symbols to the sampling frequency of the ADC and thus, in other words, the relationship between the analog signal and the ADC. An example of this relationship is shown in Figure 4.4 where R

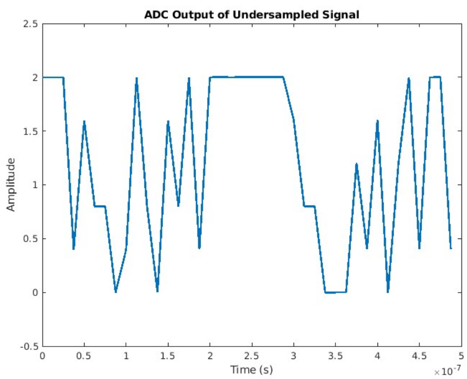

(a) Undersampled ADC output with $R = 1.25$.

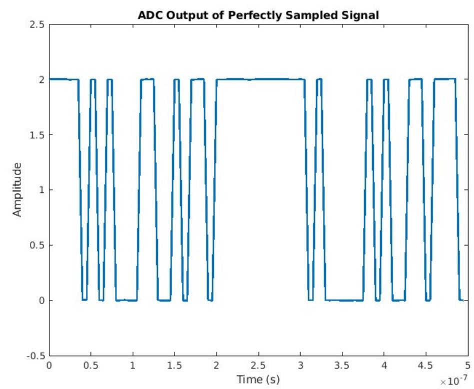

(b) Critically ADC output with $R = 0.5$.

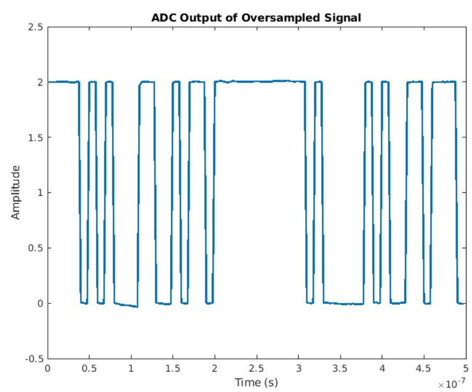

(c) Oversampled ADC output with $R = 0.25$.

Figure 4.4: $\Sigma - \Delta$ ADC digital output of the simulated symbols with sampling rates that cause undersampling (a), critically sampling (b), and oversampling (c). The undersampled output, compared to the critcally sampled and oversampled outputs, has sharp peaks and valleys with various amplitudes. The critically sampled and oversampled ADC outputs appear very similar but on closer inspection the oversampled output more information about each symbol.

is changed so that the ADC is undersampling (Figure 4.4a), critically sampling (Figure 4.4b), or oversampling (Figure 4.4c). The same 10 symbols are transmitted at a frequency of 100 MHz for easy comparison.

In addition, the sampling rate determines how many ADC samples there will be to represent the entire analog signal, as seen in (4.28).

$$M = \left\lceil \frac{N}{R} \right\rceil \tag{4.7}$$

where M is the total number of ADC samples and N is the total number of symbols transmitted.

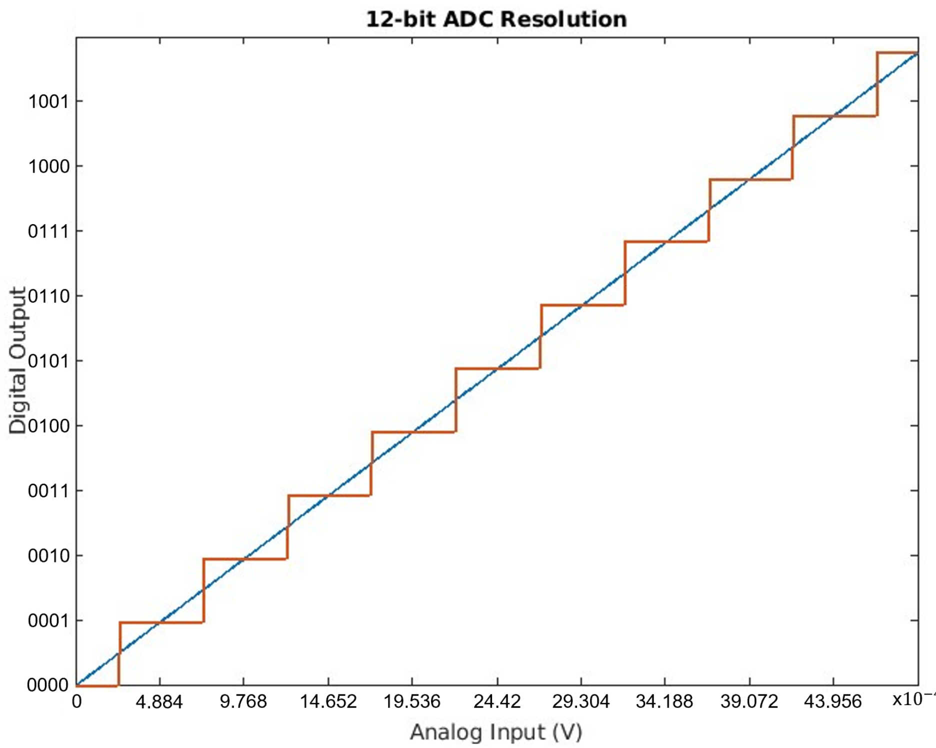

Figure 4.5: First 9 digital conversions of a 12-bit ADC conversion resolution where the analog voltages are directly related to a digital output in binary. The orange signal is a digital representation of the analog signal in blue.

The following was briefly explained in Section 2.4.2. Refer back to Figure 2.6 and Table 2.1 in the previous chapter for a basic understanding of the $\Sigma - \Delta$ architecture and the variable names that will be used in this section. In this section, there will be more details on how these signals are calculated in the 12-bit $\Sigma - \Delta$ ADC.

The Δ modulation includes a feedback signal of the previous ADC sample which is subtracted from the current ADC sample, resulting in $s_\Delta(t)$, as seen in (4.8).

$$s_\Delta(t) = x(t) - s_f(t - mT_s) \tag{4.8}$$

where $s_f(t - mT_s)$ Note that for the first sample, this value is zero. More details on the feedback loop are given below.

The output of the Δ modulation, $s_\Delta(t)$, is integrated for the duration of an ADC sample to find a singular value that can represent the analog signal. Here, the sampling rate becomes of upmost importance. When oversampling, the ADC can more precisely recreate the analog signal, although it takes up more storage. However, when undersampling the information is lost, as a singular digital value represents much more of the analog signal, making it less representative of the original analog signal. This is why the Nyquist criterion exists and why undersampled signals cannot be reconstructed. Equation (4.9) is the mathematical representation of the Σ variation.

$$s_\Sigma(mT_s) = \int_{t=(m-1)T_s}^{t=mT_s} s_\Delta(t) - s_\Sigma((m-1)T_s) + n_i(t)\, dt \tag{4.9}$$

where

$$n_i(t) \sim \mathcal{N}(0, \sigma_n^2) \tag{4.10}$$

as, again, digital devices have inherit noise which are assumed to be Gaussian. Note also that the $s_\Sigma((m-1)T_s)$ term in (4.9) is the cumulative integration of all the previous samples.

Recall that the signal has been shifted such that the ideal minimum value is 0. This means that ideal values range from 0 to twice the amplitude. Also, recall that the resolution of the ADC determines how precise the analog to digital conversion is. With a 12-bit ADC, there are 4096 possible digital values that the analog sample is mapped onto, each separated by a voltage of δ, where

$$\delta = \frac{2A}{2^{12} - 1} \tag{4.11}$$

and A is the amplitude of the transmitted BPSK signal. Thus, $s_\Sigma(mT_s)$ is rounded to the nearest analog value that aligns with a digital representation, $s_{dig}[m]$. Figure 4.5 gives an example of this relationship.

This digital value, $s_{dig}[m]$, is divided into two paths. One path leads to a $sinc^3$ filter that smooths the ADC output. This output is the final result of the $\Sigma - \Delta$ ADC and is the digital signal that will be used for demodulation. Note that, commonly, there is a decimation (downsampling) after the $sinc^3$ filter. However, this step is ignored when undersampling. The output from the $sinc^3$ filter is denoted as $s_{out}[m]$ for every T_s, as shown in (4.12).

$$s_{out}[m] = \mathrm{sinc}^3 * s_{dig}[m] \tag{4.12}$$

The other path leads to the feedback loop, where the digital value, $s_{dig}[m]$, is converted back to an analog value via a 12-bit DAC. Due to the rounding that occurred in the previous step, quantization error is introduced. From here, the ADC continues to the next sample, now where the feedback signal, $s_f(t)$, is an analog value (with some margin of error) representative of the previous ADC sample.

Windowed-$sinc^3$ Filter

The digital filter is integral to the $\Sigma - \Delta$ ADC. $sinc^3$ filters are popular for low-frequency, high-resolution applications. The $sinc^3$ response has a steeper roll-off characteristic and zeros at multiples of the throughput rate, which helps in AC power line rejection (see Figure 4.6) [23]. The purpose of the $sinc^3$ filter at the output of the ADC is to smooth the digital signal. Small discrepancies are smoothed and large jumps between different symbols are not as erratic. The mathematical representation of the $sinc^3$ filter is derived in (4.13) through (4.15).

The third-order *sinc* filter transfer function is given by [31]:

$$H(z) = \left(\frac{1}{L} \frac{1 - z^{-L}}{1 - z^{-1}} \right)^3 \tag{4.13}$$

where L is the length of the filter. Note that the length is commonly an odd number so that the peak of the filter can be centered. This equation corresponds to a magnitude response of

$$|H(e^{j\omega})| = \left| \frac{sin(M\omega/2)}{M sin(\omega/2)} \right| \tag{4.14}$$

A Blackman window, specified in (4.15), is multiplied element-wise – giving the filter the fitting name of windowed-$sinc^3$ filter. It should also be noted that the $sinc^3$ filter is normalized for unity gain before filtering the ADC samples.

$$w(l) = 0.42 - 0.5 \cos\left(\frac{2\pi l}{L-1}\right) + 0.08 \cos\left(\frac{4\pi l}{L-1}\right) \qquad 0 \le l \le L-1 \tag{4.15}$$

The frequency response of the $sinc^3$ filter is shown in Figure 4.6.

4.2 Algorithm for Information Recovery

The algorithm presented in this thesis is a proof-of-concept that completely reconstructing analog signals after they have been undersampled is plausible. However, there is much future work in order to have a faster and more robust algorithm, which is discussed in Chapter 6. The AIR is applied in post-processing, right

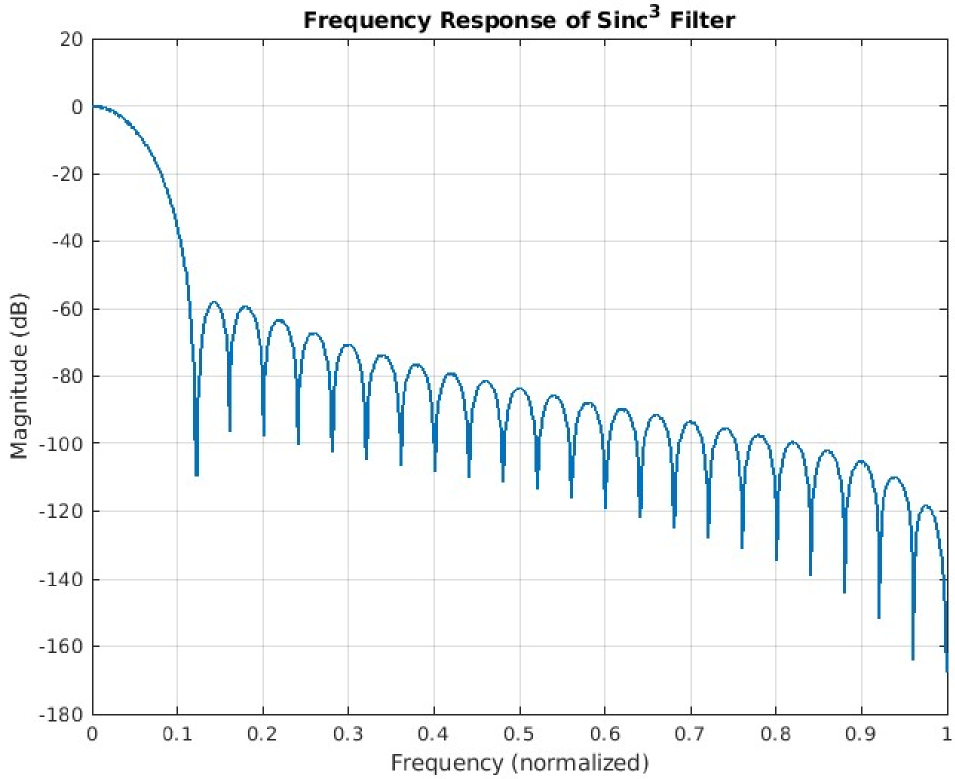

Figure 4.6: Normalized frequency response of windowed-$sinc^3$ filter of length $L = 51$. The $sinc^3$ filter is windowed with a Blackman window.

after the ADC has finished converting the analog signal into digital values. This algorithm is based on the probability density function (PDF) of the ADC output, $s_{dig}[m]$, to recover the lost symbols and thus reconstruct the original analog signal, $x(t)$.

First, the ADC output is normalized by dividing by the amplitude of $x(t)$, so that the range of the ADC output is 0 to 2 (not including noise). This normalization eases the following computation and allows results to be comparable in practice and literature.

4.2.1 Probability Density Function

The PDF of the output of the $\Sigma - \Delta$ ADC provides key information about the digital signal. Thus, it is crucial that the PDFs generated in simulation and the math provided in Section 4.1.2 align.

Recall that in (4.9) there is a Gaussian random variable in the integration meant to represent the inherent noise found in digital devices. The analog signal is deterministic and can be easily calculated. The definite integral of the Gaussian noise is another Gaussian random variable. This phenomenon is shown with (4.16) through (4.17).

$$\int_{(m-1)T_s}^{mT_s} n_T(t)dt = \mathcal{W}_{mT_s} - \mathcal{W}_{(m-1)T_s} \tag{4.16}$$

where $n_T(t)$ is the total Gaussian noise from the communications channel, $n_e(t)$, and the ADC, $n_i(t)$, and the result is the difference of two Wiener processes. One characteristic property of Wiener processes is that they have Gaussian increments with mean 0 and variance μ.

$$\mathcal{W}_{mT_s} - \mathcal{W}_{(m-1)T_s} \sim \mathcal{N}(0, \mu) \tag{4.17}$$

Consider an oversampled digital signal. From the information provided above, it is clear that the resulting PDFs of the ADC samples are Gaussian with a mean at either 0 or 2, depending on the symbol that was transmitted. The mean is at 2 when 1s are transmitted due to the DC shift applied at the beginning of the ADC. Figures 4.7a and 4.7b show these PDFs with a highly oversampled ADC and a BPSK signal that has transmitted solely 0s or 1s, respectively.

Notice that these PDFs do not look Gaussian. This is due to the quantization error of the ADC. Rounding values that go outside the digital range (from 0 to 2A) cause otherwise Gaussian distributions to not appear so. Removing this quantization error reveals that the PDFs are Gaussian as seen in Figures 4.8a and 4.8b. However, it is not physically possible to remove this error in hardware and

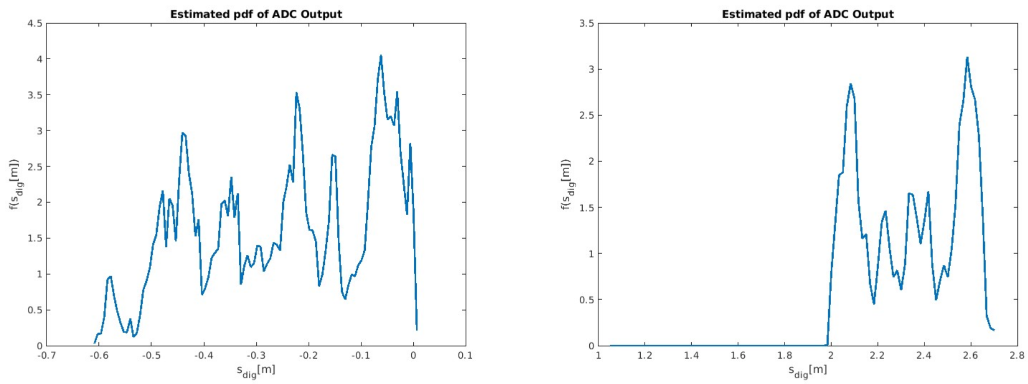

(a) PDF of only binary 0 symbols transmitted.

(b) PDF of only binary 1 symbols transmitted.

Figure 4.7: PDFs of oversampled ADC output when either only binary 0s (a) or binary 1s (b) are transmitted. The resulting PDFs are not Gaussian due to the inherit quantization error within the ADC (this is true for all ADCs).

thus will be maintained in the simulation as well.

4.2.2 Information Recovery

When undersampled, the PDFs of the ADC samples become more complex as information is not only lost, but various symbols end up within the same ADC sample. However, the proportions of symbols within a sample correlate greatly with the peak(s) of the PDF. The proportion of each symbol defines how much of that symbol is in the ADC sample that is being demodulated. Since R, the ratio between the rate of the symbols and the sampling frequency, is a known value, it can be used to determine the proportion of symbols within a sample. Figure 4.9 shows an example of this concept.

There are three main scenarios that define what an ADC sample's PDF can look like: peak at 0, peak at 2, or peak in between. If the ADC sample PDF has a peak at 0, all symbols within that sample are also 0. Similarly, if the ADC

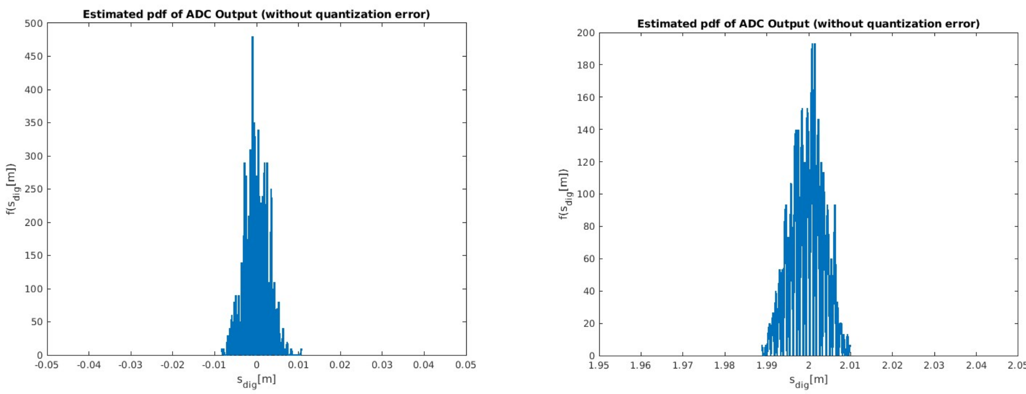

(a) PDF of only binary 0 symbols transmitted.

(b) PDF of only binary 1 symbols transmitted.

Figure 4.8: PDFs of oversampled ADC output when either only binary 0s (a) or binary 1s (b) are transmitted. Removing the quantization error results in Gaussian PDFs, which is the expect result. It is not physically possible to remove the quantization error and thus will not be removed from the simulation. This figure demonstrates the Gaussian property of the $\Sigma - \Delta$ ADC.

sample PDF has a peak at 2, all symbols within that sample are 1. For these two scenarios, symbol recovery is fairly straightforward. Refer to Figures 4.10a and 4.10b for examples of these PDFs.

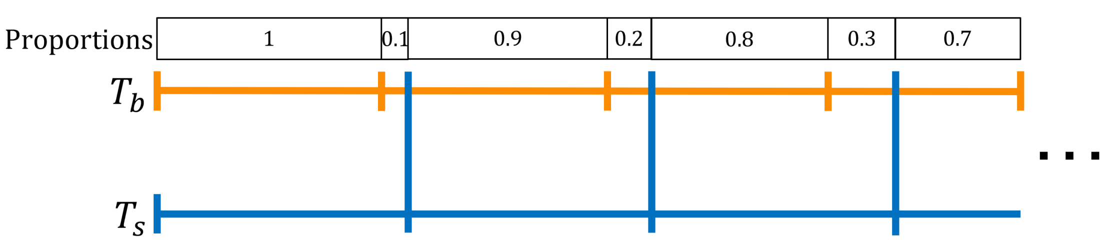

Figure 4.9: Proportion of symbols within ADC samples with $R = 1.1$ and 4 symbols transmitted. This is a visualization of how the duration of the symbols and the samples affects how much of each symbol will be contained in each sample.

The complexity arises when the symbol changes during a single ADC sample. When this occurs, the resulting PDF has a peak somewhere between 0 and 2. Now, the question is how to determine which symbols and in what order the symbols are in. This is where the proportion of symbols within an sample is key.

Since the ADC is undersampling, R will always be greater than 0.5, as discussed in (4.11). Table 4.1 gives a brief description of how the value of R changes the relationship between symbols and samples. Note that although when $R < 1$

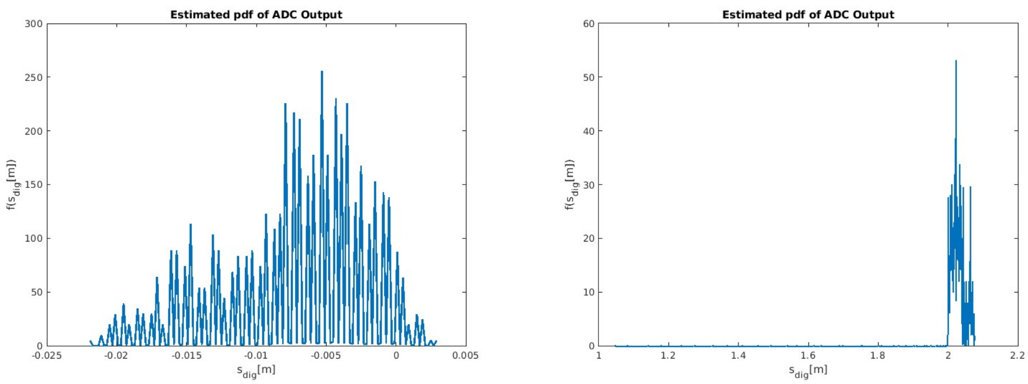

(a) PDF of only binary 0 symbols transmitted.

(b) PDF of only binary 1 symbols transmitted.

Figure 4.10: PDFs of undersampled ADC, where $R = 1.1$, output when either only binary 0s (a) or binary 1s (b) are transmitted. Note again how the quantization error causes the PDFs to not appear Gaussian.

R	Symbol to Sample Relationship
$R < 1$	There will be more than one sample per symbol
$R = 1$	Exactly one symbol within each sample
$R > 1$	There will always be more than one symbol within each sample

Table 4.1: Symbol to sample relationship depending on R for undersampling ADCs. R is the ratio between the symbol frequency and the sampling frequency.

the ADC is undersampling the signal, the duration of a sample is shorter than the duration of a symbol, it is just more than $\frac{1}{2}T_b$.

The easiest scenario to recover and reconstruct the analog signal is when $R = 1$. Since there is exactly a 1:1 ratio between symbols and samples, the sample PDFs will always have a peak at either 0 or 2. Note that this algorithm, for now, ignores any time delay between the signal and the ADC.

When $R > 1$ or $R < 1$, the information recovery process is as follows. Let P be a $1 \times p$ matrix that contains the proportions of the symbols contained in an ADC sample. p can be equally described as two things: the number of symbols within a sample or the number of proportions in P.

$$P_1 = \begin{cases} 1 & q_{m-1} = 1 \\ 1 - q_{m-1} & otherwise \end{cases} \tag{4.18}$$

$$q = R - P_1 \tag{4.19}$$

Where q is the part of the ADC sample in which the proportions of the symbols have yet to be determined and q_{m-1} indicates the proportion of the last symbol contained in the previous sample (i.e., the value of P_p of the previous ADC sample). Note that when demodulating for the first symbol of the signal, q_{m-1} is assumed to be 0.

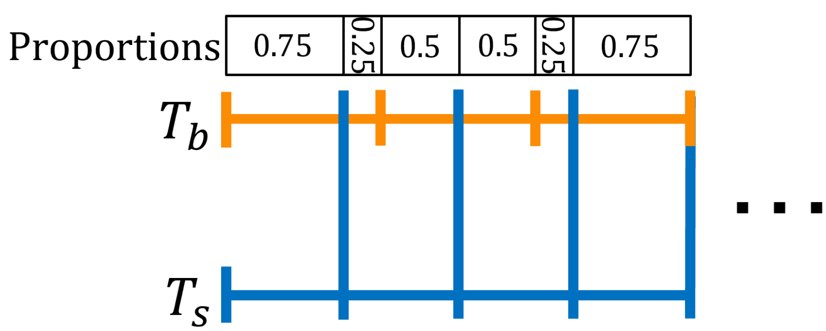

Figure 4.11: Proportion of symbols within ADC samples with $R = 0.75$ and 3 symbols transmitted. This is a visualization of how the duration of the symbols and the samples affects how much of each symbol will be contained in each sample.

There are two scenarios that can occur here. One, where q is less than 1, meaning that there are two symbols within the sample. Two, where q is greater than or equal to 1, which means that there are more than two symbols in the sample. Examples of these two scenarios are shown in Figures 4.11 and 4.9 (from

Section 4.2.2), respectively.

If $q < 1$, only (4.22) is necessary. If $q > 1$, proportions of value 1 must be added between the first and last proportions in P, since those symbols are completely contained within that singular sample. See (4.20) and (4.21).

$$P_2, ..., P_{p-1} = 1 \tag{4.20}$$

where

$$p - 1 = \lfloor q \rfloor + 1 \tag{4.21}$$

and

$$P_p = q - \lfloor q \rfloor = q_m \tag{4.22}$$

Note that $p - 1 = 0$ when $q < 1$ and no additional proportions will be added to P other than the proportion calculated in (4.22). Note here that q_m, which is the proportion of the symbol that is contained within the currently sample, will become q_{m-1} once we start the AIR process again for the following ADC sample.

Although P shows the physical proportions of the symbols within a sample, the actual proportions of the symbols, P', are relative to R. This is because the sample PDFs are in terms of the sample duration, not symbol duration. To adjust P, use (4.23). This step fully characterizes the ADC sample in terms of symbol proportions.

$$P' = \frac{2P}{R} \tag{4.23}$$

The final step of the AIR is to demodulate the undersampled signal using the sample PDF and proportions matrix, P', of the ADC sample. Simply, determine which symbols make up the ADC sample.

First, find all possible combinations of symbols based on the number of symbols in the sample, p. Essentially, what needs to be found is

$$C = 0 : 2^p \qquad \textit{in binary} \tag{4.24}$$

where C is a $2^p \times p$ matrix that contains a two-level full-factorial design. In other words, it provides the numbers from 0 to 2^p in binary form, where each symbol is its own element within the matrix. For example, if there are two symbols per sample, there are four possible combinations: $C = \begin{bmatrix} 0 & 0 & 1 & 1 \\ 0 & 1 & 0 & 1 \end{bmatrix}^T$.

Throughout this section, the peak of the PDF has been aptly used to describe and determine the symbols within a sample. However, more specifically, it is the location of this peak that contains the necessary information to demodulate the signal. Interestingly, the location of the peak of the ADC sample PDF, $\arg\max\{f(s_{out}[m])\}$, is directly related to the symbols and their proportions within the sample. Thus,

$$C'_{i,j} = C_{i,j} P'_i \tag{4.25}$$

represents how all combinations of symbols would behave within the sample given the calculated proportions P'. The proportions affect how much weight each symbol has within a symbol and, in turn, change the shape of the PDF accordingly.

The algorithm goes through each row of C' – each possible combination of symbols – and evaluates it with the inequality seen in (4.26).

$$\left| \Sigma_{i=1}^{p} C'_{i,j} - \arg\max\{PDF(s_{out}[m'])\} \right| < \epsilon \quad T_s m < \frac{T_s}{\alpha} m' < T_s(m+1) \tag{4.26}$$

where ϵ is the margin of error and α is how many artificial samples are added. Here, $s_{out}[m']$ is the same digital signal, $s_{out}[m]$, which was outputted by the

$\Sigma - \Delta$ ADC. However, m' represents the artificial samples that are added to the ADC output in post-processing. These artificial smaples are added via a simple interpolation where each ADC output value is held for the specified duration of the ADC sample, T_s. These additional samples allow the AIR to generate an estimated PDF of each ADC sample.

Once the algorithm hits a combination that makes (4.26) true, those symbols are saved in matrix S of dimension $N \times 1$. S contains all the originally transmitted symbols, including the lost information due to undersampling in the ADC.

If a symbol is split between two samples (i.e., $q_{m-1} \neq 1$), it can be assumed that the first symbol of the current ADC sample (m) is the same symbol as the last symbol of the previous ADC sample ($m - 1$). This speeds up the process, eliminating certain combinations in C' that do not begin with the correct symbol.

This process presented in this section is repeated for all ADC samples. Thus, with the use of sample PDFs and the proportion of symbols within each ADC sample, the lost information due to undersampling can be recovered and the analog signal can be reconstructed.

Parameter	Value
A	1
N	25
$f_{c,b}$	100 MHz
T_b	10 ns
$f_{c,m}$	100 MHz
ϕ_0	0°

Table 4.2: Example simulation parameters for BPSK signal generation.

4.3 Simulation

This section is a walk-through of the simulation presented in this chapter. Section 4.3.1 will discuss the robustness and accuracy of the AIR as applied to this simulation.

Table 4.2 describes the signal that was generated as per Section 4.1.1. Figures 4.12, 4.13, and (4.27) show the BPSK signal generation up to the received signal, which has 25 dB of channel noise.

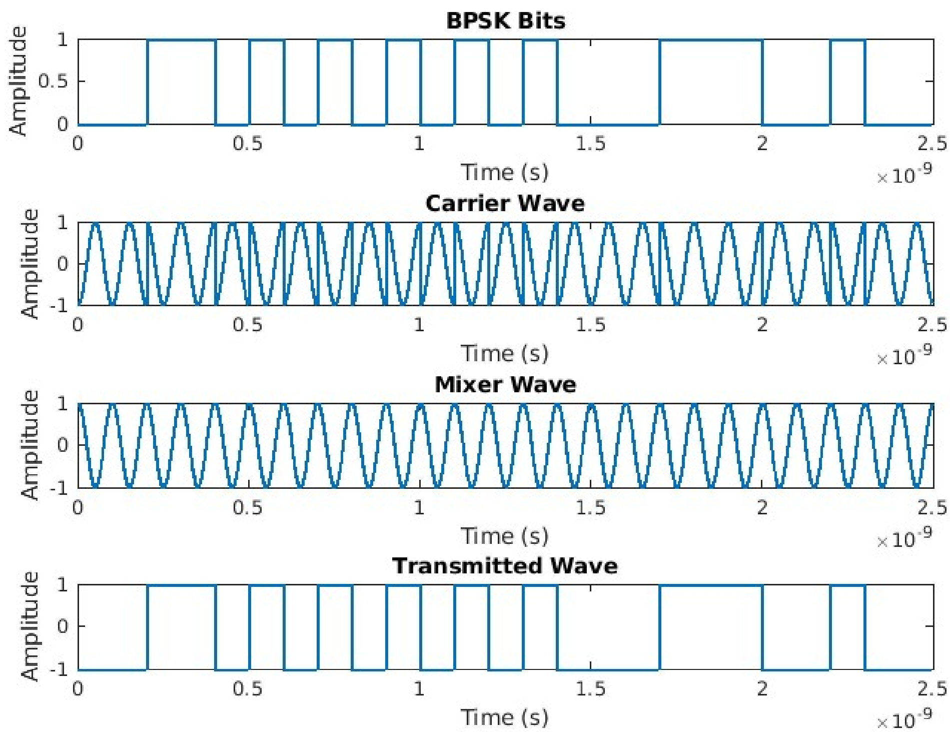

Figure 4.12: BPSK wave generation for example simulation using the parameters from Table 4.2. The signals in order from top to bottom are: the BPSK phase terms, the carrier wave, the mixer wave, and the transmitted BPSK signal. The transmitted wave is a square wave since the carrier wave and mixer wave are at the same center frequency. This means that the transmitted wave depicted here is a baseband representation of what is actually transmitted.

As can be seen in Figure 4.12, the transmitted BPSK code is:

$$0011010101010100011100100.$$

Recall that a 1 signifies a 180° and a 0 signifies a 0° phase shift. This is more noticeable in the carrier wave. Once mixed with the mixer wave, the frequency cancels out and the shown transmitted wave remains. Thus, this means that the transmitted wave shown is actually a baseband representation of what is actually transmitted by the communications system. Figure 4.13 represents the received

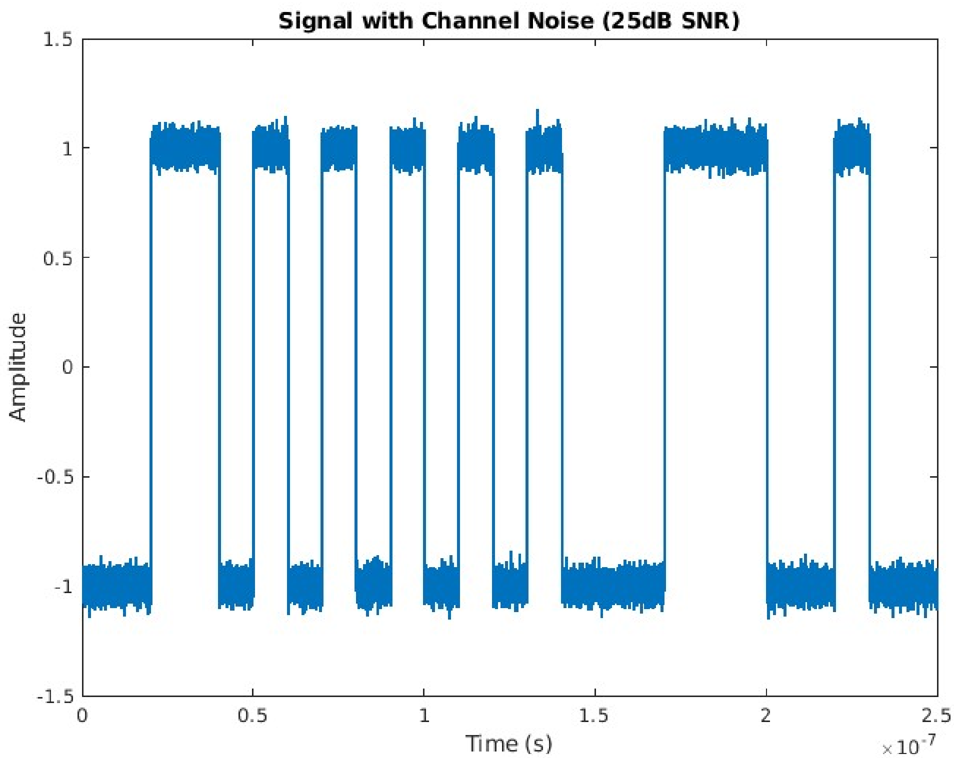

Figure 4.13: Received BPSK signal with 25 dB of channel noise. The channel noise a property of 5G systems and has been simulated with additive white Gaussian noise.

signal, $x(t)$, where,

$$c(t) = e^{j\phi_m} + 1 \tag{4.27}$$

due to the center frequencies of the carrier and the mixer waves and the channel phase shift, which has been left at 0° (recall (4.4)).

The proportion of symbols to samples can be found to be $R = 1.6$, using (4.6). Since the number of symbols originally transmitted is known, we can easily calculate the number of samples the ADC will take of the signal using,

$$M = \frac{N}{R} \tag{4.28}$$

which comes out to be $M = 16$ for this example.

Parameter	Value
f_s	62.5 MHz
T_s	16 ns
R	1.6
M	16
L	3

Table 4.3: Parameters for example simulation of $\Sigma - \Delta$ ADC with significant undersampling.

Following what was described in this chapter and in Section 2.4.2, Figure 4.14 shows the output of the analog-to-digital conversion process. Since the signal is undersampling, there is already limited information in the ADC output, too large of a digital filter will distort the information further, truly making the analog signal unrecoverable. Table 4.3 show the parameters for the ADC.

From here, the AIR post-processing is applied. Figures 4.15a through 4.15c show sample PDFs from the ADC output in Figure 4.14. These three figures give a general idea of what the sample PDFs look like. The peaks always lie between 0 and 2, inclusive. The proportions of symbols in each ADC sample are shown in Table 4.4. Recall that when there are two symbols per sample, there are four possible combinations for the symbols and when there are three symbols per sample, there are eight possible combinations for the symbols. However, the last symbol of the previous sample gives insight on the first symbol of the following sample. It is assumed that when the last symbol of a sample is completely contained within that sample, the proportion pattern will repeat.

Though not noticeable, there are 16 distinct values that make up the output of the $\Sigma - \Delta$ ADC, as determined by (4.28).

Once the AIR recovers the lost symbols, the demodulation and/or any other post-processing can ensue. For the purposes of confirming this algorithm, the symbols recovered by the AIR are compared to the symbols that were originally transmitted. Figures 4.16a and 4.16b provide two different visual comparisons of binary codes, which are the same.

4.3.1 Robustness and Limits in Simulation

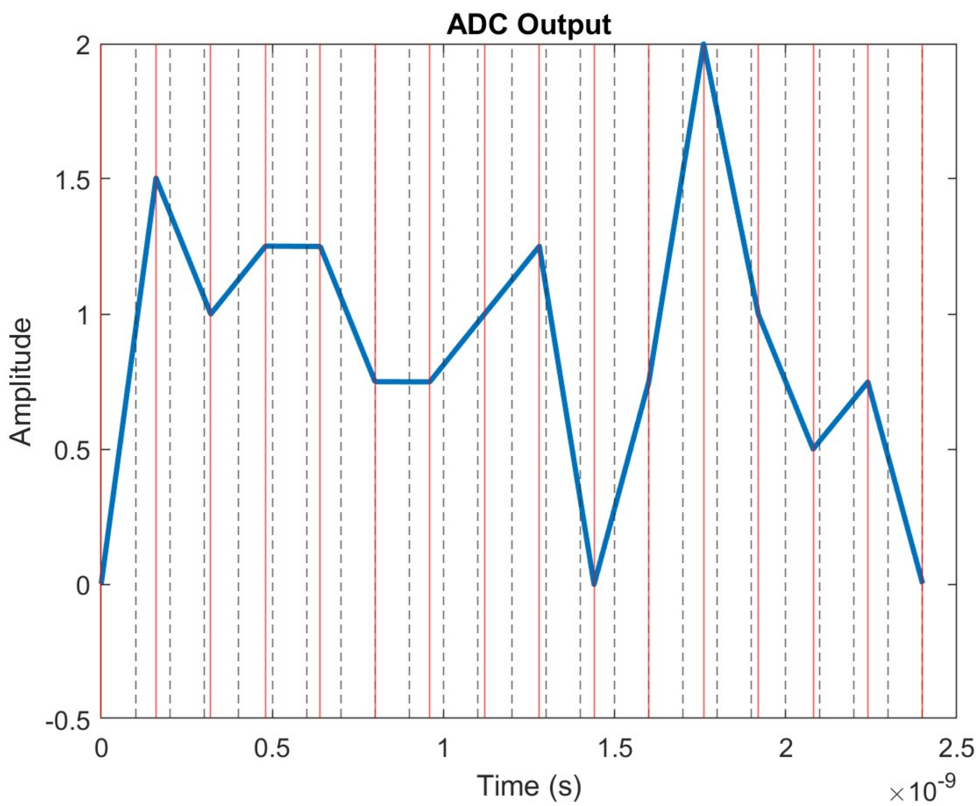

Figure 4.14: ADC simulation digital output after $sinc^3$ filter of size $L = 3$. The lines in black represent the symbols and the red lines represent where the ADC samples are in terms of their duration.

Results for this novel proof-of-concept algorithm have shown promise, as can be seen from the example provided in the previous section and in this section.

Sample	Symbol 1	Symbol 2	Symbol 3
1	1	0.6	-
2	0.4	1	0.2
3	0.8	0.8	-
4	0.2	1	0.4
5	0.6	1	-
7	1	0.6	-
8	0.4	1	0.2
9	0.8	0.8	-
10	0.2	1	0.4
11	0.6	1	-
12	1	0.6	-
13	0.4	1	0.2
14	0.8	0.8	-
15	0.2	1	0.4
16	0.6	1	-

Table 4.4: Proportions of symbols within each ADC sample for $R = 1.6$. Note that for any sample, if the proportion is not 1 for Symbol 1, the last symbol of the previous symbol (either 2 or 3) will be the same symbol split between the two samples.

Running tests with different numbers of N and values of R helped to understand the robustness and limits of this algorithm. Recall that any value of $R > 0.5$ is considered undersampling, which is the range of values explored for these results.

Testing different values of R helps determine the limits of the AIR. The limits being where the AIR begins to fail in recovering the lost symbols and, in turn, reconstructing the analog signal. The upper limit is due to the fact that too much information is contained within a sample. The lower limit is caused by the complex scenario of samples with shorter durations than the symbols, but not enough to meet the Nyquist criterion.

The simulation is run with values of R ranging from 0.5 to 2.5 (i.e., sampling frequencies from 40 MHz to 100 MHz), not inclusive. The symbol error for these tests are shown in Table 4.5. Figure 4.17 shows a visualization of the relationship between the value of R and the symbol error between the recovered symbols and the originally transmitted symbols. Note that this plot was made with a different set of bits and more fine spacing between the values of R than shown in Table 4.5. Note that the signal was generated with the parameters in Table 4.2 except $N = 500$, which are the same for all tests.

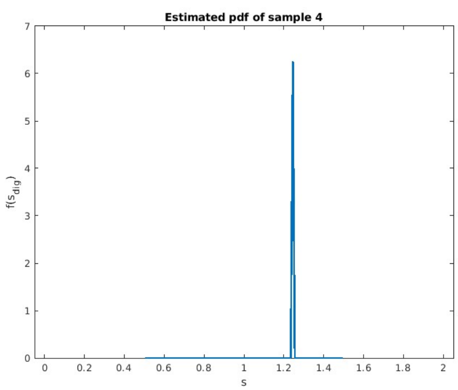

(a) PDF for the 4th sample of the ADC output with a peak at approximately 1.25.

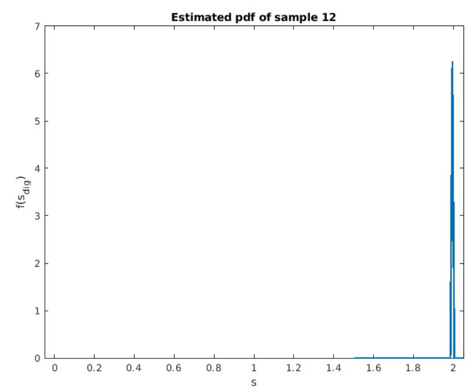

(b) PDF for the 12th sample of the ADC output with a peak at 2.

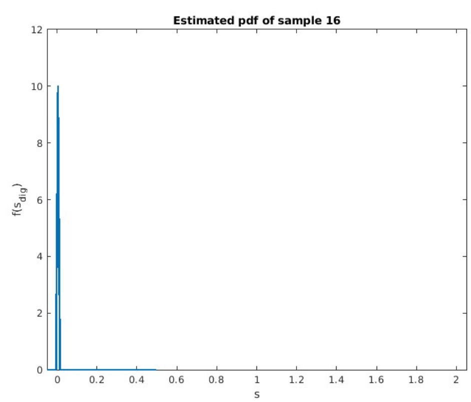

(c) PDF for the 16th sample of the ADC output with a peak at 0.

Figure 4.15: Sample PDFs of $\Sigma - \Delta$ ADC output for the example simulation. The peaks are always between 0 and 2, inclusive. In order, (a) shows the peak at 0, (b) shows the peak at 2, and (c) shows the peak somewhere in between.

Looking at values of $R < 1$, there is a trend for the significant symbol error.

All these values, except for $R = 0.75$ end up always have three samples per symbol at some point in the AIR process (when finding the probabilities of symbols within each sample). This causes major errors for this version of the AIR. The

```
Transmitted symbols: 0  0  1  1  0  1  0  1  0  1  0  1  0  1  0  0  0  1  1  1  0  0  1  0  0
Recovered symbols:   0  0  1  1  0  1  0  1  0  1  0  1  0  1  0  0  0  1  1  1  0  0  1  0  0
```

(a) Binary code (symbols) of transmitted and received signals.

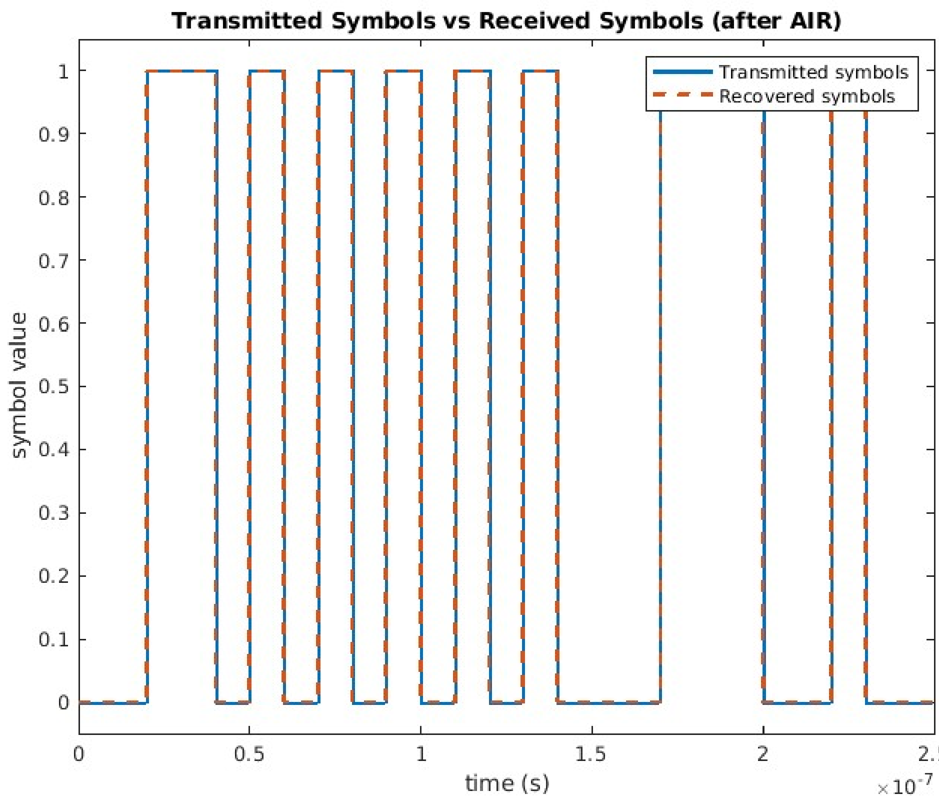

(b) Visual comparison between transmitted and received symbols.

Figure 4.16: Original symbols versus recovered symbols – after post-processing with the novel AIR algorithm and demodulation – for the provided example simulation. (a) shows the transmitted and recovered symbols while (b) is a visual representation of this.

algorithm believes a whole symbol is contained within a sample, which is true, but it also believes that that means that symbol is only contained within that sample. Unfortunately, this is an incorrect assumption, as one sample has a shorter duration than one symbol, it is just not quite half as long (to meet the Nyquist criterion).

R	Symbol Error	Number Incorrect Symbols
0.55	0.500	250
0.7	0.496	248
0.75	0	0
0.8	0.494	247
0.9	0.484	242
1	0	0
1.05	0.016	8
1.1	0.026	13
1.2	0.026	13
1.25	0	0
1.3	0.030	15
1.4	0.042	21
1.45	0.024	12
1.5	0	0
1.6	0	0
1.65	0.002	1
1.7	0	0
1.8	0.002	1
1.85	0.008	4
1.9	0	0
1.95	0.028	14
2	0.224	112
2.05	0.066	33
2.1	0.060	30
2.2	0.080	40
2.3	0.110	55
2.4	0.120	60
Avg. Error	**0.135**	**67.5263**

Table 4.5: Symbol error for different R values with $N = 500$ symbols via simulation in MATLAB. For all the different values of R, the same 500 symbols are transmitted for fairness and validity comparison. Note that the last column is the number of incorrect symbols out of the 500 symbols originally transmitted.

For the values of $R > 2$, there is a trend of increasing symbol error. This is due to too many symbols in one sample. With such a large R, there is a minimum of two complete symbols within a sample, meaning that more information is lost than retained by the ADC. At this point, a more complex AIR would be required to adjust for such loss in information. However, again, this is just a proof-of-concept algorithm.

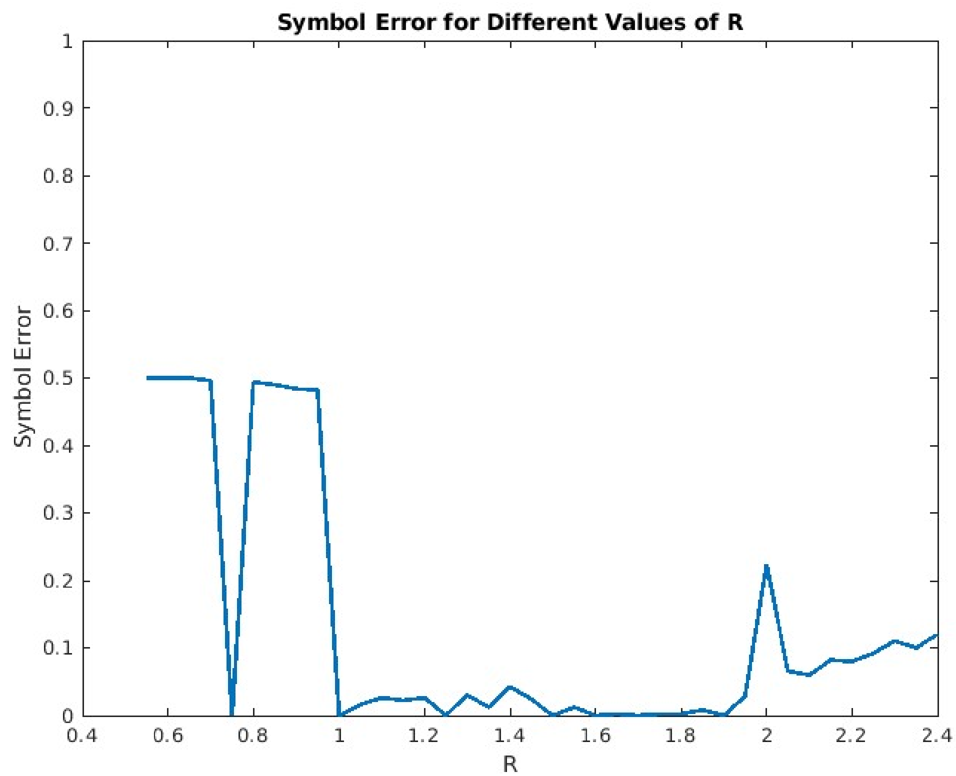

Figure 4.17: Graphical representation of the results in Table 4.5, but more verbose. The spacing between each value of R is 0.05 and ranges from 0.55 to 2.4, inclusive. Note that values of $R > 1$, the error increases relatively linearly. AT values of $R < 1$, there is significant symbol error. There is no symbol error at $R = 1$.

For the values of R ranging from 1 to 1.95, there is minimal error, with the largest being a 3.6% error. Here, symbol durations are equal to or less than the duration of a sample. Very rarely are there three symbols per sample for these values of R – and if that is to occur, it is the middle symbol that is completely contained within the sample while the first and last symbol are split with the adjacent samples.

However, when $R \geq 2$, the error starts to increase. This error is due to the fact that the larger the value of R, the more likely it is that a whole symbol will be lost within the sample. This makes it harder to recover those symbols that are completely encased in a sample.

Overall, values of R between 1 and 1.95, inclusive, are the most ideal for symbol recovery, as determined by simulation.

4.4 Experimentation

GNU Radio is an open-source toolkit that provides signal processing blocks for software defined radios (SDRs). The flowgraphs developed in GNU Radio represent different digital signal processing and hardware techniques that can be applied in either simulation or real-time hardware. This work only uses GNU Radio for its real-time system capabilities in conjunction with SDRs. SDRs are use software to manage tasks usually conducted in hardware, such as modulation and filtering.

The generation of the BPSK signal is designed in GNU Radio. The Ettus Research X310 SDR is used in lieu of a communications system.

Figure 4.18 presents the GNU Radio flowgraph that generates the BPSK signal. The X310 SDR is set in loopback mode, where the transmitter port is connected to the receiver port via a cable. With this set up, the transmitted signal is sent directly to the receiver. The received signal is saved for post-processing in MATLAB, which in this case is the $\Sigma - \Delta$ ADC and symbol recovery algorithm presented previously in this chapter.

The first block is the Constellation Modulator, which takes any input in byte format and modulates it to be a BPSK constellation. A BPSK constellation should ideally look like Figure 2.2, but due to noise some distortion and spreading occurs. The Polyphase Clock Sync block performs timing synchronization via

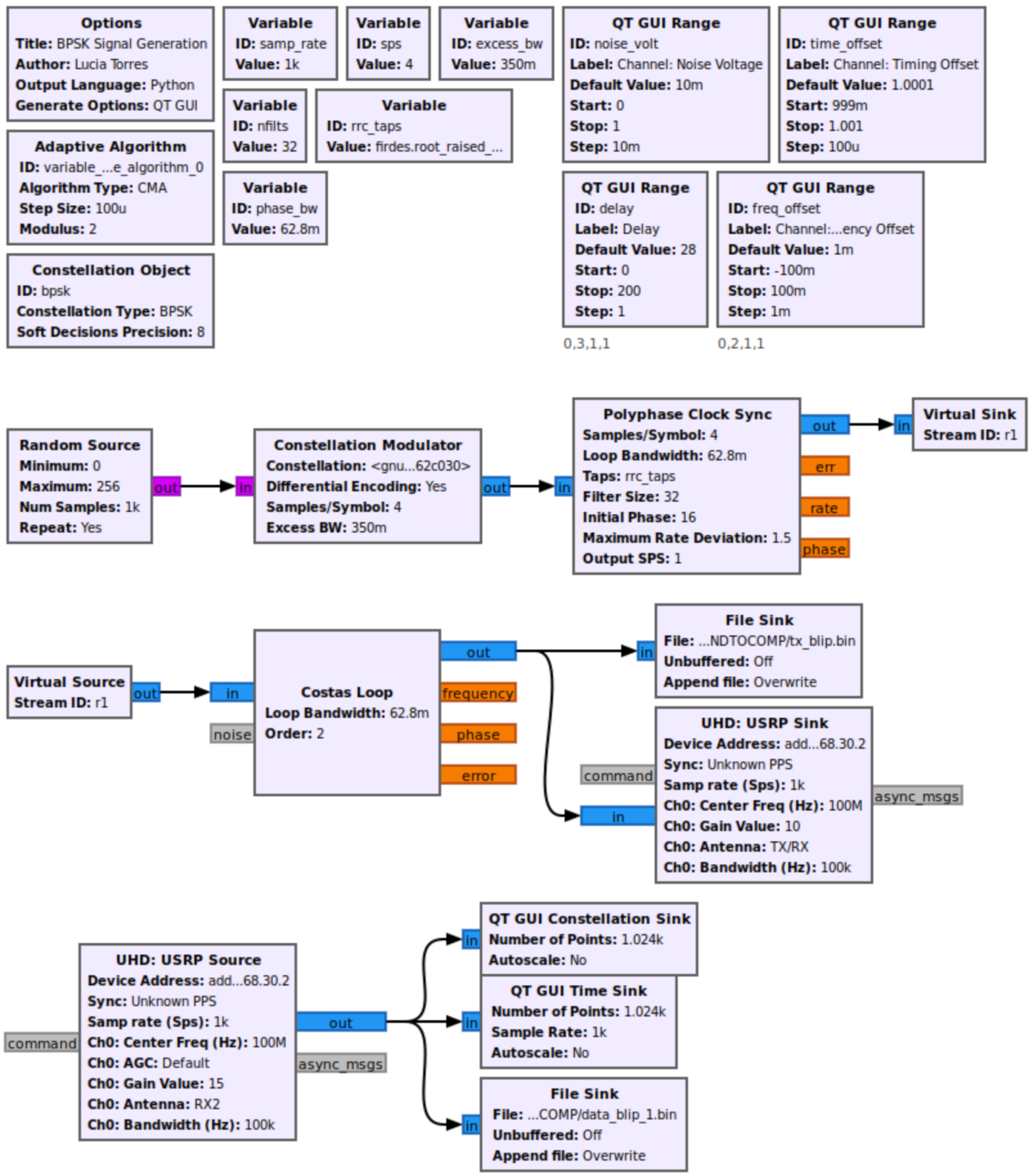

Figure 4.18: GNU Radio flowgraph of BPSK signal generation with transmitter and receiver. The UHD: USRP Sink and Source blocks represent the transmitter and receiver on an SDR, respectively. For this experiment, the SDR is set in loopback and the received BPSK signal is stored for post-processing in MATLAB.

polyphase filterbanks. The Costas Loop block, the last block of the BPSK signal design, downconverts the signal to baseband. This output is then sent to the X310 SDR's transmitter port and, because the SDR is in loobpack mode, received by the receiver port.

In MATLAB, the process is the same as in the simulation, but begins by passing the received BPSK signal through the $\Sigma - \Delta$ ADC. Essentially, the real BPSK signal is passed into the $\Sigma - \Delta$ ADC, which undersamples the signal, and then is sent through the AIR for post-processing symbol recovery.

4.4.1 Robustness and Limits in Experimentation

To test the robustness of the AIR, the signal received by the receiver port of the SDR is used as the ground truth, representing the symbols that were originally transmitted. These symbols are compared to the symbols recovered by the AIR to determine the accuracy and robustness of the algorithm.

Table 4.6, similar to Table 4.5, shows the symbol error of the recovered symbols compared to the original symbols for different values of R. The same values of R are used as in the simulation tests for completeness and easy comparison. The same 500 symbols are used for each test.

For values of $R < 1$, the error is significant (except for $R = 0.75$), to the point where almost half of the recovered symbols do not match the original symbols. However, once we reach $R = 1$, the only value of R for which there is no error, the error ratio begins to decrease to a more palatable value. From $1.1 < R < 2.4$, the symbol error is fairly consistent at approximately 26%. Although this is worse than the simulation results by a factor of 2, the experimentation results are still promising.

Consider $R = 1$ and $R = 0.75$, which have the two lowest errors from the tested values of R. By changing the number of symbols, N, transmitted and thus the number of samples generated by the ADC, the AIR has a longer processing time, with more opportunity for error. Note that this implies that the computational

R	Symbol Error	Number Incorrect Symbols
0.55	0.482	241
0.65	0.482	241
0.75	0.184	92
0.85	0.478	239
0.95	0.480	240
1	0	0
1.1	0.266	133
1.2	0.232	116
1.3	0.240	120
1.33	0.294	147
1.4	0.262	131
1.5	0.216	108
1.6	0.250	129
1.7	0.290	145
1.75	0.256	128
1.8	0.248	124
1.9	0.298	149
1.95	0.260	130
2	0.252	126
2.1	0.292	146
2.2	0.252	126
2.3	0.300	150
2.4	0.264	132
Avg. Error	**0.286**	**143**

Table 4.6: Symbol error for different R values with $N = 500$ symbols via experimentation with the X310 SDR and post-processing in MATLAB. For all the different values of R, the same 500 symbols are transmitted for fairness and validity comparison. Compare these results with the results shown in Table 4.5.

complexity increases proportionally to how many samples are being processed by the AIR. Table 4.7 shows the symbol error for different values of N.

For $R = 1$, the number of symbols in the BPSK signal does not seem to matter, as all values gave the same, perfectly recovered, result. However, with $R = 0.75$, which was known to have errors, the error varies slightly. With a symbol error mean of 19.88% and a range of 2.79%, it is concluded that the length of the BPSK signal affects the AIR results.

N	$R = 0.75$ Symbol Error	$R = 1$ Symbol Error
500	0.1840	0
1000	0.1920	0
6785	0.1973	0
10000	0.1976	0
75	0.2267	0
333	0.1952	0
Avg. Error	**0.1988**	**0**

Table 4.7: Symbol error for various N with $R = 1$ or $R = 0.75$ via experimentation with the X310 SDR. The results show a standard deviation of 0.0279 and 0, respectively for each value of R. This confirms that changing the length of the signal affects the success of AIR.

These tests and their results serve as a demonstration that symbol recovery is possible, even if only to a certain extent, when the signal has been undersampled.

4.5 Conclusions on Data Recovery

First, this chapter introduces a novel $\Sigma - \Delta$ ADC simulation. The simulation is based on mathematical models that are derived from the physical components that make up a $\Sigma - \Delta$ ADC. For this project, the purpose of the ADC was to undersample the signal. Undersampling has always been considered a dangerous and detrimental effect of ADCs that this work aims to mitigate.

A novel symbol recovery algorithm is presented, appropriately named the Algorithm for Information Recovery. This simple post-processing algorithm serves as a proof-of-concept that undersampling can be overcome. In other words, the purpose of AIR is to show that recovering lost symbols is possible, to some extent, and that developing methods to mitigate undersampling is a possible solution to faster conversions.

An ADC that can sample at a lower rate than required by the Nyquist theorem would allow for lower manufacturing and power costs and faster transmission of information. If the drawbacks of using a lower sampling rate can be adjusted for in post-processing, information travel speeds could exponentially increase, introducing a new age of high-speed connectivity.

Although simulation results performed better than experimental results, both sets of tests confirm that symbol recovery is a possible route to increase information travel speeds. Since $R = 1$ appears to be the most consistent value in simulation and experimentation, undersampling such that the sampling frequency is half of the Nyquist frequency could potentially increase data rates by a factor of at least 2, as the ADC would no longer be a constraint.

More will be discussed in Chapter 6 of this thesis.

Chapter 5

Out-Of-Band Interference from 5G Emissions

It is the concern of the FAA that high-powered wideband technology, such as 5G networks, will affect the performance of radalts. 5G emissions could seep into the radalt band, or radalts could accidentally operate at frequencies outside their allocated band. The tests and experiments performed in this section establish and validate the fundamental systems needed for OOB interference. Experiments with these systems allow for a deeper understanding and analysis of the coexistence between adjacent band technologies, as is the 5G interference problem presented by the FAA and in this thesis (review Chapter 3).

Experiments and tests are performed in the large anechoic chamber at the Advanced Radar Research Center (commonly referred to as the ARRC) in Norman, OK and outdoors. The designs of the FMCW radalt and 5G OFDM emissions are generated in GNU Radio. SDRs are used in all of these experiments to emit the signals generated in the GNU Radio flowgraphs and to capture the returned information. Specifically, Ettus Research X310 and B210 SDRs are used as the radalt and 5G OFDM emissions, respectively.

This chapter is organized as follows. Section 5.1 explains the FMCW radalt flowgraph and the tests that confirm its proper operation. Section 5.2 describes the OFDM waveform, which simulates 5G emissions. In Section 5.3, both technologies operate simultaneously, producing the data that prompt the analysis and discussion of Section 5.4. Chapter 6 contains a final summary and future work for this project.

5.1 FMCW Radalt Setup

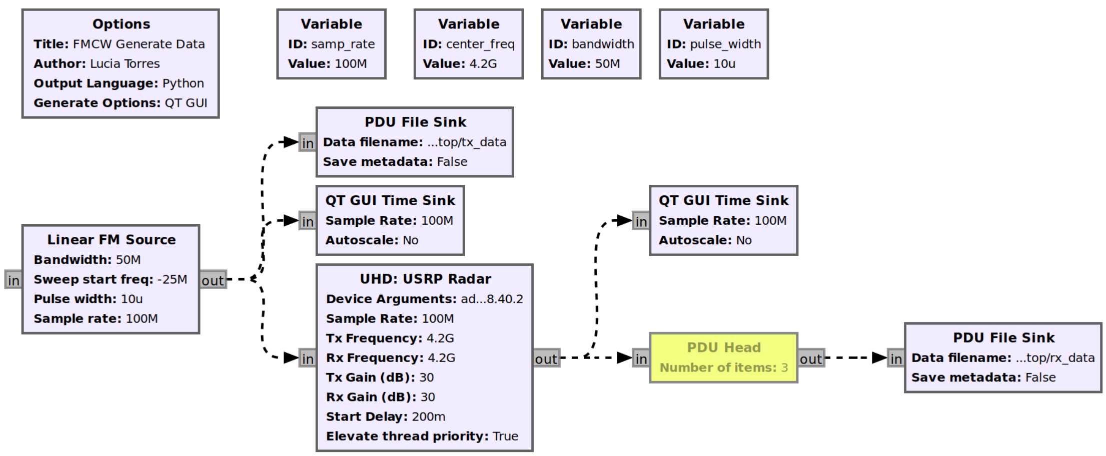

Figure 5.1: GNU Radio flowgraph of FMCW radalt transmitter and receiver. The UHD: USRP Radar block represents the transmitter and receiver on the SDR. These blocks are a part of the gr-plasma module by [32] and [33].

Figure 5.1 shows the GNU Radio flowgraph that generates an FMCW signal for radar applications. The flowgraph uses blocks from the gr-plasma module, a GNU Radio module by [32] and [33] specifically for radar signal processing applications.

The Linear FM Source, from [32], generates an LFM waveform. With a pulse repetition frequency of 0, since FMCW is continuous (and how the block was developed), the LFM source can be used as an FMCW source. The UHD: USRP Radar block connects (via Ethernet) the GNU Radio to the X310 SDR. Note that this block takes care of both the transmit and receive ports on the SDR for convenient data collection [33]. The PDU File Sink blocks save the transmit and receive signals for post-processing. The PDU Head block stops after the designated number of chirps have been processed. The QT GUI Time Sink blocks are used for visualization – plotting the signal over time – to ensure that the signal is being transmitted and received correctly during data collection.

A common issue that arose, which prompted the use of the QT GUI Time Sink blocks, was that the receive antenna was not actually capturing any data. This can be easily observed with the temporal plots. It is expected that any real received signal will be affected by noise. An error would cause the received signal to not display any noise. Using temporal plots to confirm that the received signal looked realistic (and not unusually clean) ensures that no cable or antenna is malfunctioning.

The four variable parameters are: sample rate (F_s), center frequency (F_c), bandwidth (β), and chirp duration (T). These parameters can be easily changed in the flowgraph, allowing for adaptability depending on the experiment, application, and capabilities of the SDR and host computer. For all the experiments and tests

Parameter	Value
F_c	4.2 GHz or 2.4 GHz
F_s	100 MHz
β	45 MHz
T	10 μs

Table 5.1: Parameters to generate FMCW radalt signal that is transmitted by the X310 SDR. These parameters are seen at the top of Figure 5.1 and can be changed according to the application and scenario. Note that the center frequency varies from either 4.2 GHz to 2.4 GHz depending on the experiment.

carried out in this chapter, the parameters remain consistent with those of Table 5.1. These parameters are comparable to those seen in radalts. Due to hardware and software limitations, the bandwidth and sampling rate are slightly lower than ideal. Note also that the center frequency is sometimes lower than what is expected from actual radalts (i.e., outside the radalt band).

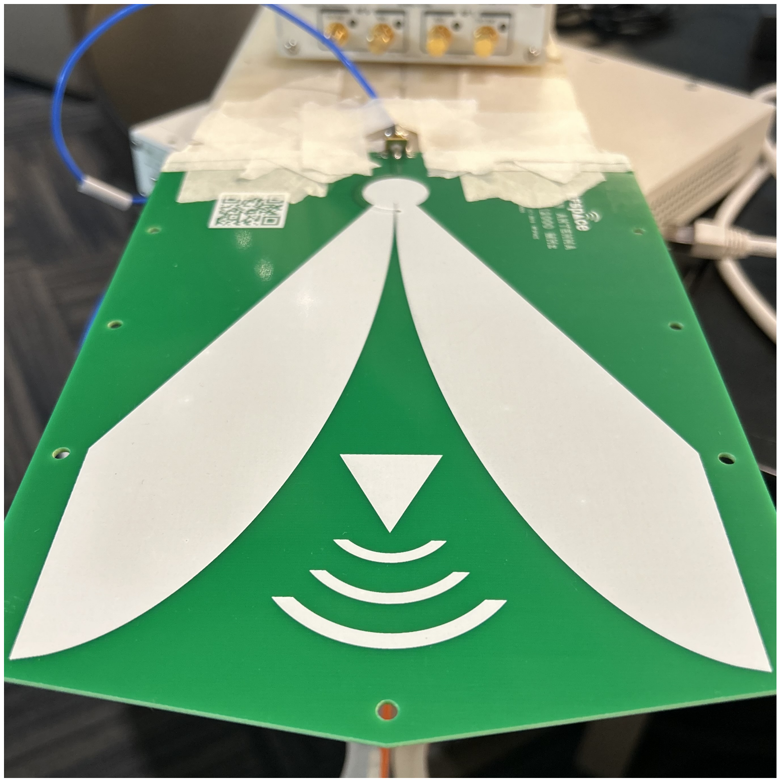

Figure 5.2: Antenna used for tests and experiments. The TSA900-12000 ultra-wideband slot antenna is used for transmitting and receiving FMCW signals as well as transmitting the OFDM signal in Section 5.3.

Recall that the FCC has designated the radalt band as restricted and only to be used by approved radalts. In the anechoic chamber and in loopback, operating at these frequencies is inconsequential. However, operating within the radalt band outdoors, where other technologies and possibly radalt systems are also operating, is dangerous. Thus, the center frequency is set at 2.4 GHz, which is within the Industrial, Scientific, and Medical (ISM) band. This is due to the safety precautions regarding the radalt band and the FCC's RF spectrum regulations.

The TSA900-12000 ultra-wideband slot antenna, pictured in Figure 5.2, is used for all transmit and receive needs. A total of three antennas are needed for the final experiments, where OFDM is introduced as interference to the FMCW radalt.

5.1.1 Loopback Tests

The X310 SDR is set in loopback mode, where the transmitter port is directly connected to the receiver port. A 30 dB attenuator is connected to the receiving side of the cable. The center frequency for these tests is set at 4.2 GHz. The GNU Radio flowgraph presented in Figure 5.1 runs on the X310 SDR.

The autocorrelation of one chirp of the transmitted signal is shown in Figure 5.3. This result is what is expected from an LFM pulse, and thus confirms that the radar is transmitting the correct signal.

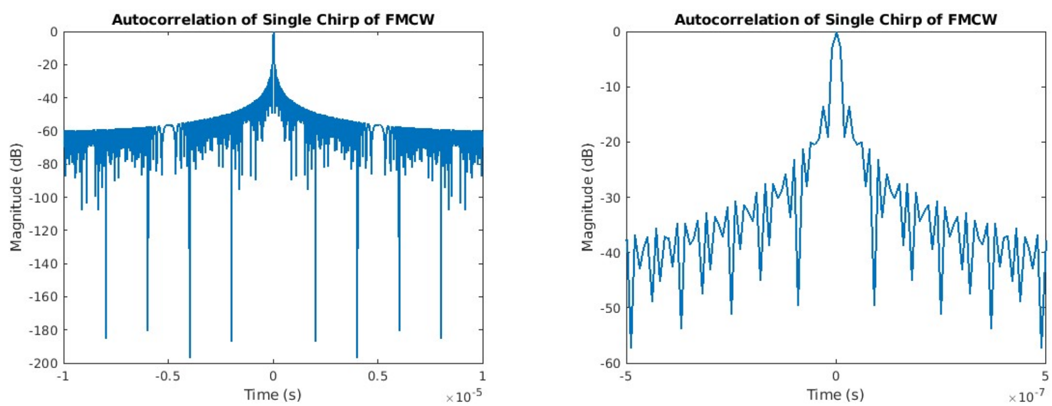

(a) Complete normalized autocorrelation. (b) Zoomed in autocorrelation.

Figure 5.3: Normalized autocorrelation (a) of a single chirp of the transmitted FMCW signal using X310 SDR. Note that the peak of the autocorrelation is at 0 s (or, alternatively, 0 m), as expected.

Figure 5.4 shows the matched filter and stretch processing outputs, superimposed on top of each other, of four FMCW chirps sent via loopback. The peak of both outputs is near 0 m, which is where we would expect it to reside in loopback, as the signal only travels the short distance of the cable (which is less than one range bin). Note that the exact peak is not at 0 m, likely due to hardware instability such as direct path leakage within the SDR's RF components, noise introduced by the hardware and traveling through a cable, and unexpected jitters.

Recall that ideally, matched filtering and stretch processing have identical range resolution. In this loopback case, the conditions are pretty much ideal and the difference between the two post-processing algorithms is minimal. The main distinction is that the stretch processing output has deeper nulls between sidelobes.

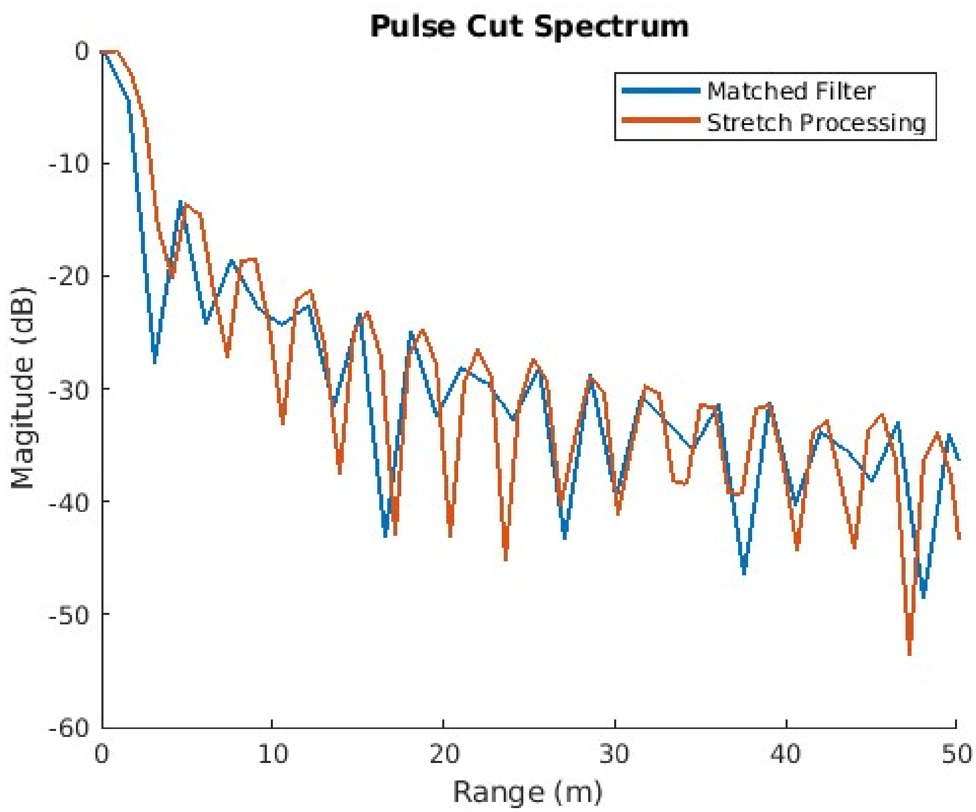

Figure 5.4: Normalized post-processing outputs for matched filtering (blue) and stretch processing (orange) applied to the received data. The received data is four chirps collected in loopback using the X310 SDR. The matched filter output appears nosier than the stretch processing output due to the range granularity (see Section 5.1.2).

The loopback mode test confirms that the X310 SDR, which will act as the radalt in future experiments and discussions, is transmitting and receiving an

FMCW signal. It is further concluded that the matched filter and stretch processing techniques result in the expected (relatively similar) outputs.

5.1.2 Range Detection Tests

The range detection tests were conducted in the large anechoic chamber and outdoors. The outside tests allow for more variability in the range of the target. The target is a large sheet of copper – a good reflector with high returns. Within the anechoic chamber, the copper reflector is approximately 8.56 m from the radalt. Outside, the target's range can vary from 0 to 1500 m, the maximum unambiguous range found with (5.1). However, there are other technologies and objects around the testing area, so the ranges were kept relatively close to the radalt. See Figure 5.5 for a picture of the test environment within the anechoic chamber.

$$R_{max} = \frac{cT_c}{2} \tag{5.1}$$

There are two goals with this test: to confirm that the generated FMCW signal can detect the copper reflector at the expected distance from the radar and to see the improvements in the data with stretch processing compared to matched filtering (recall Section 3.2.1). For these tests, the X310 SDR is equipped with two of the ultra-wideband antennas (depicted in Figure 5.2), one for transmitting and one for receiving.

Plotting a range versus time plot, commonly called a range-pulse (chirp) map, shows the location of targets, if any, detected by the radalt. Stationary targets, as will be the copper reflector, have no Doppler and stay at a constant range throughout the duration of the measurement. That is, the target should be contained in a singular range bin that determines the radial range (the distance from the radar).

The bandwidth of the signal determines the range resolution (the size of the range bins) and does not change if applying matched filtering or stretch processing. However, the range granularity – defined as how finely the range is sampled in post-processing – is affected by the post-processing algorithm applied. For the matched filter, the range granularity is the same as the range resolution of the system and is found with (3.3) in Section 3.2.1. The range granularity for the stretch processing output is found with (5.2) from [24]. For all tests and experiments, the size of the FFT (K) is set to 4096 (2^{12}), which is a couple of powers of 2 higher than the original length of the chirp. K can be changed depending on the application, although one must be aware of the possibility of range migration if the target is nonstationary and the additional computational complexity that comes with a larger FFT size.

$$\Delta R = \frac{Mc}{2\beta K} \tag{5.2}$$

Where M is the number of range bins and K is the size of the FFT. Note that, normally, $K \geq M$ and therefore the stretch processing output provides range bin widths that are equal to or smaller than that of the range resolution (recall (3.3)). Also note that this fine-resolution output is often called a high-resolution range profile [24].

First, tests were conducted in the anechoic chamber. The anechoic chamber is a specially designed room that prevents electromagnetic waves from interacting with other technologies (WiFi and Bluetooth) or objects (walls and floors). Since, within the anechoic chamber, there are no external technologies that could interfere with the radalt, the results are clean and without much noise other than the inherit noise from using hardware. As stated previously, the center frequency is set to 4.2 GHz for these tests.

The antennas and the copper reflector are arranged as shown in 5.5. The two antennas are offset so that there is less direct path leakage from the transmit antenna into the receive antenna. The copper reflector is 8.56 m from the antennas.

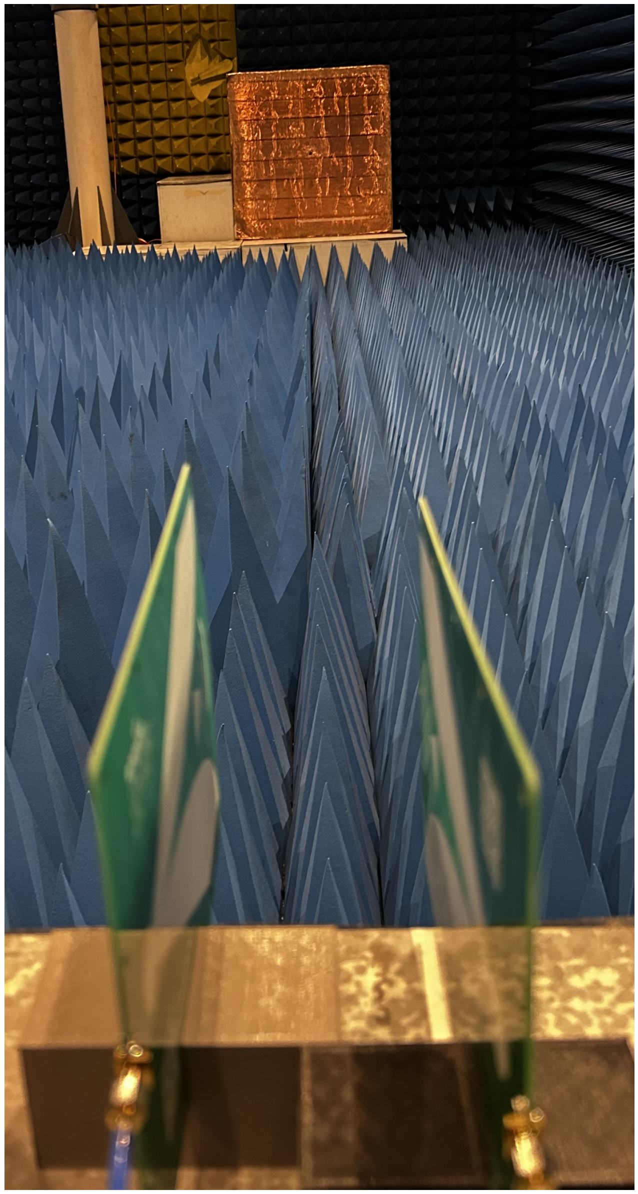

Figure 5.5: Anechoic chamber set up for tests and experiments. The two antennas in this figure represent the transmit (left) and receive (right) antennas for the FMCW radalt. Note how the receive antenna is slightly behind the transmit antenna to mitigate some of the direct path leakage. The copper reflector is approximately 8.56 m from the antennas. This same set up was recreated outside.

A bandwidth of 45 MHz yields a range resolution of 3.33 m, which is small enough for the target to be detected at the range at which it is located.

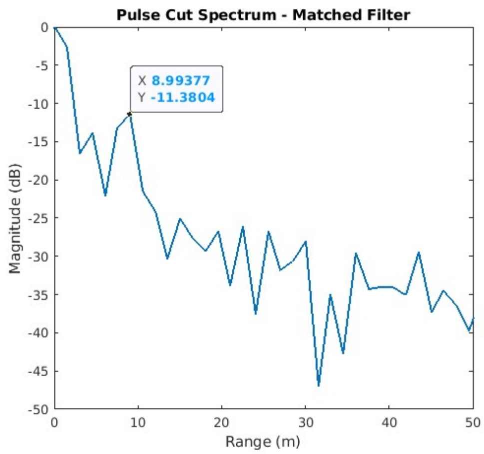

(a) Matched filtering output with target appearing at 8.99 m.

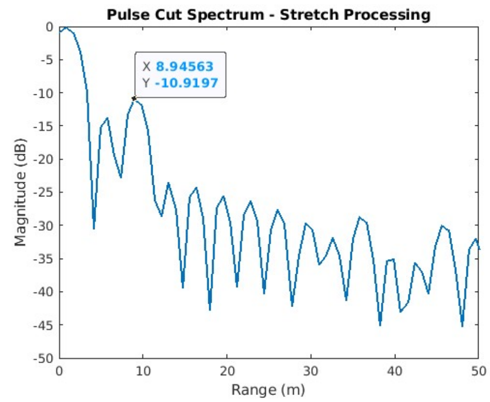

(b) Stretch Processing output with target appearing at 8.94 m.

Figure 5.6: Zoomed-in normalized matched filtering (a) and stretch processing (b) outputs of received range detection data for measurements done in the anechoic chamber. For the matched filter output, the target is shown to be at 8.99 m, which is the range bin that includes 8.56 m. Similarly for the stretch processing output, the target is shown to be at 8.94 m. The second highest peak is determined as the target because the highest peak, which is found at 0 m, is a result of the direct path leakage.

Figures 5.6a and 5.6b represent the same data processed in two ways: with the matched filter and with stretch processing. Note that the target always shows up in the same range bin and is the one closest to the true value of the copper reflector.

Note that the target is not the largest peak due to the direct path from the transmitter leaking into the receive. Thus, the second highest peak is identified as the target. Within the chamber, the normalized results show the target with a magnitude of approximately −11 dB.

The target appears to be at different ranges depending on whether the matched filter or stretch processing output is observed. However, this is an impossibility as the range-pulse plots are generated with the same data. Since the size of the stretch processing output is much larger than that of the matched filter output (due to the FFT), the range resolution granularity improves. That is, there are more smaller range bins yielding more accurate results.

To further confirm that the FMCW is detecting range properly, the system was moved outside, where more varied ranges could be chosen. The center frequency was lowered to 2.4 GHz for these tests. The antennas and the copper reflector are arranged in the same manner as shown in Figure 5.5. To accommodate being outside, the radalt system was set up on a movable cart. The two antennas are offset, as they were in the chamber, so that there is less direct path leakage from the transmit antenna into the receive antenna. Since it was already shown that stretch processing yields more accurate results than the matched filter, only the stretch processing outputs for the outdoor tests are presented – although, both post-processing algorithms were run during the tests to confirm the results.

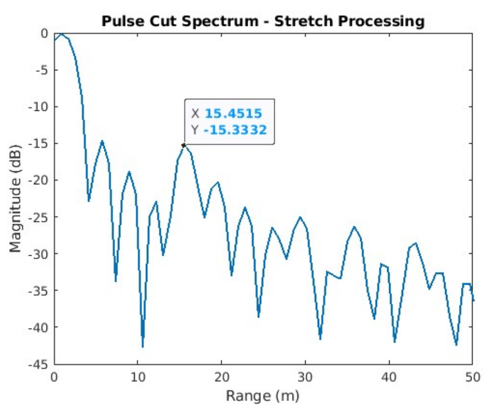

(a) Target appearing at 15.5 m.

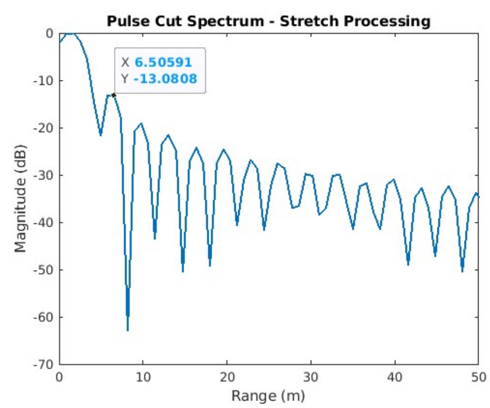

(b) Target appearing at 6.5 m.

Figure 5.7: Stretch processing outputs of range detection data for outdoor measurements. The target is at 15.2 m (a) and 6.4 m (b), respectively. The second highest peak is identified as the target because the highest peak is a result of direct path leakage.

The results, as expected, are similar to those collected in the chamber. Moving the target to different ranges moves the peak accordingly to the correct range bin.

Note that direct path leakage generates significant sidelobes, which act as clutter in this scenario. The further the target is from 0 m, the less affected it is by these sidelobes. Compare Figures 5.7a and 5.7b – which have a target at 15.2 m and 6.4 m, respectively – to observe this.

With these tests and the previously described loopback test, it is confirmed that the FMCW radalt is operating as expected. Knowing this, 5G OFDM interference can be added to the experiments. The effects of the OOB interference can be examined with certainty that the FMCW radalt performs as expected when no interference is present.

5.2 5G OFDM Emissions Setup

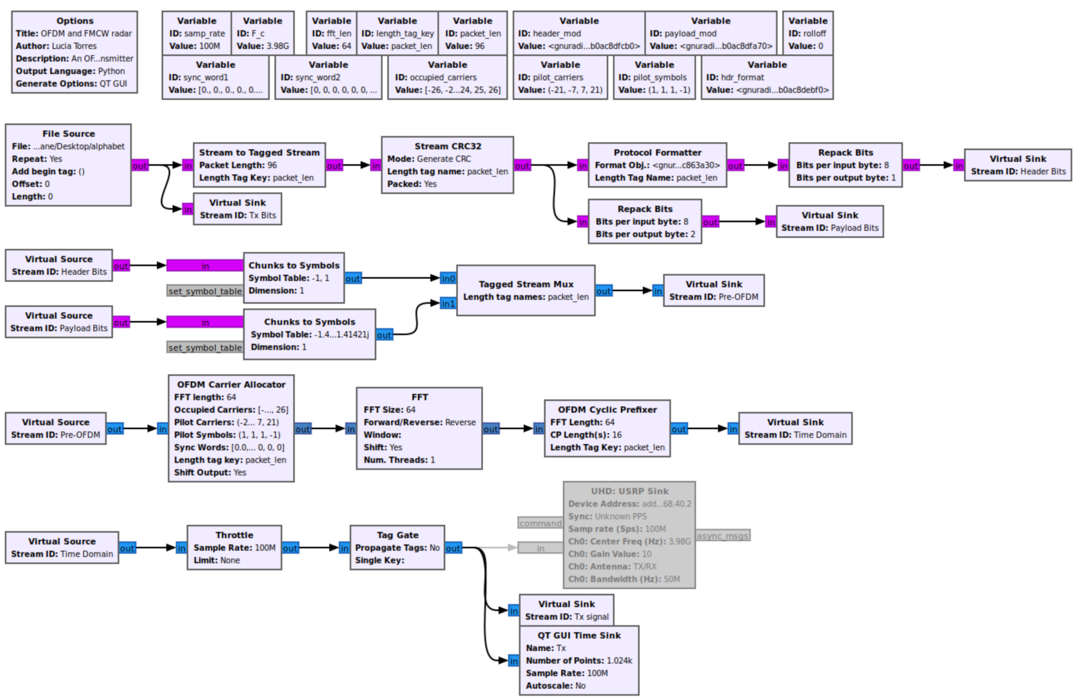

Figure 5.8: GNU Radio flowgraph that generates an OFDM signal, which represents 5G emissions in the experiments in Section 5.3.

Figure 5.8 shows the GNU Radio flowgraph that generates an OFDM signal for 5G applications.

From the File Source block to the Tagged Stream Mux block, the flowgraph generates header and payload bits, which are then combined in the Tagged Stream Mux block to create packets of data. From there the flowgraph generates the OFDM signal, adding the cyclic prefix with the aptly named OFDM Cyclic Prefixer block. The OFDM signal is then transmitted, passing through a Tag Gate block to stop the propagation of the tags.

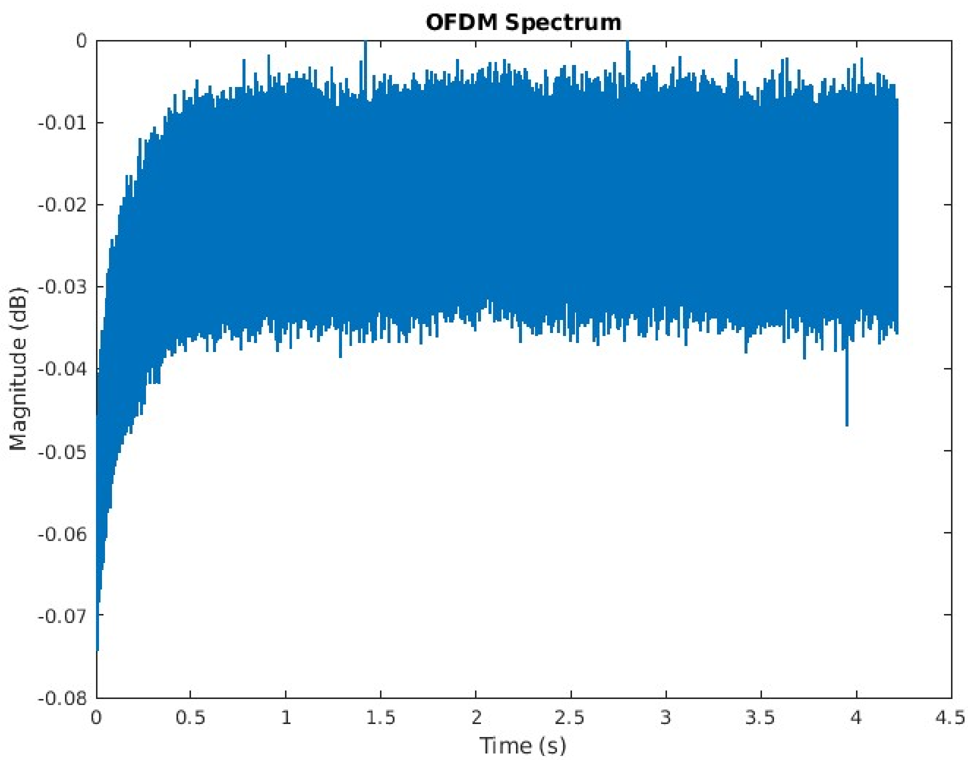

Figure 5.9: Normalized 5G OFDM example spectrum. The OFDM symbols are generated using the alphabet as the information being transmitted.

There are two things to note in Figure 5.8: the Throttle block and the disabled UHD: USRP Sink block (grayed out block). The Throttle block is only used when running the flowgraph in simulation, as was done for these tests. When used in later experimentation (see Section 5.3), the UHD: USRP Sink block is enabled to connect the flowgraph to the B210 SDR and the Throttle block is removed (or bypassed) from the flowgraph.

Figure 5.9 shows an example of the 5G OFDM transmission spectrum. However, since the symbols are pseudorandom, this spectrum changes as a function of time. Looking at the beginning of the plot, from around 0 to 0.5 seconds, there is short curve until the signal reaches a stable magnitude with an average of approximately -0.02 dB. This is due to the warm-up period the OFDM signal must have right when the flowgraph begins.

To avoid this affecting the experiments in Section 5.3, the FMCW radalt was not turned on until after the 5G OFDM emissions had been operating for a couple of seconds. Note that because the OFDM spectrum is found via loopback with the SDR, the power levels are not the same as those discussed in Section 5.3.1.

5.2.1 Demodulation Tests

Although it is not required in OOB interference experiments, demodulating the transmitted OFDM signal confirms that the flowgraph generates the expected signal. One issue that commonly occurs when generating OFDM data in GNU Radio is that the bit rate will automatically adjust to mitigate noise, which does not align with what happens in reality.

Figure 5.10 shows the GNU Radio flowgraph that demodulates the transmitted signal (generated via the flowgraph in Figure 5.8).

The transmitted signal first goes through a Channel Model block, which simulates a 5G channel and adds noise to the signal. The transmitted OFDM signal is then received with the OFDM Receiver block, which demodulates the signal. The transmit and receive symbols are then processed in MATLAB to determine if there is any error.

The expected result is that when no noise is applied in the Channel Model block (the noise voltage is set to 0 V), the demodulated OFDM symbols are exactly the same as the transmitted symbols. Figure 5.11a shows this to be true. When noise is applied to the Channel Model block (with a noise voltage of 1 V),

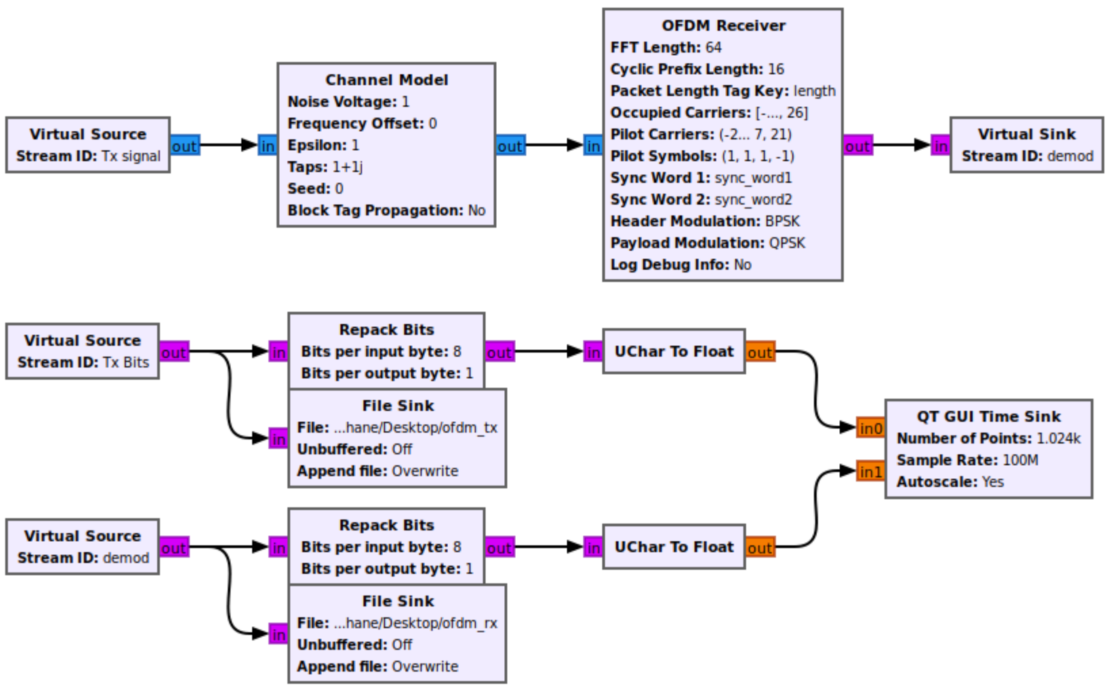

Figure 5.10: GNU Radio flowgraph that demodulates the OFDM signal generated by the flowgraph in Figure 5.8. The demodulated bits are compared with the originally transmitted bits in the second part of this flowgraph.

some error is expected. If GNU Radio were altering the bit rate to mitigate the noise, the errors would not appear, and results would be the same as when no noise is applied. Figure 5.11b shows that the addition of noise in the Channel Model block causes errors. This confirms that the OFDM signal is generated without changes in the bit rate.

Note that, due to the functionality of the OFDM Receiver block, there is always the same number of symbols that are cut off from the end of the signal. This does not affect the modulation of the OFDM signal, which is required for the OOB interference experiments in Section 5.3.

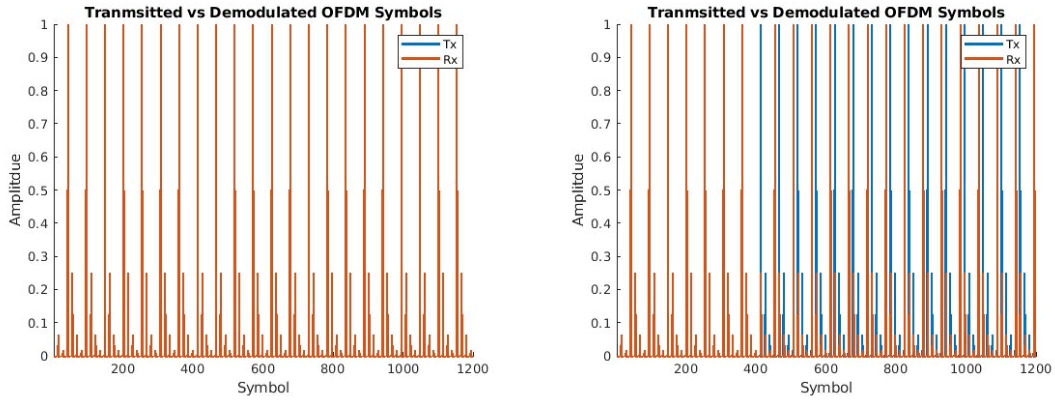

(a) With no noise in the Channel Model block.

(b) With noise in the Channel Model block.

Figure 5.11: Transmitted versus received symbols (after demodulation) with (b) and without (a) noise in the Channel Model block. Note that there is no error when there is no noise in the system. However, this case is not realistic. When channel noise is added, errors occur and the demodulated bits do not correspond with the originally transmitted bits.

5.3 Out-of-Band Interference Experimentation

The chamber is set up as shown in Figure 5.12. The antennas at the forefront of the figure are, as in Figure 5.5, the transmit and receive antenna for the FMCW radalt. Since the experiments are conducted within the confines of the anechoic chamber, the radalt can operate at a center frequency within the radalt band (at 4.2 GHz). On the opposite side of the chamber are the copper reflector and the OFDM transmitter. A separate computer is connected to the B210 SDR and runs the proper GNU Radio flowgraph (Figure 5.8). The antenna is facing directly at the radalt antennas, with the goal of interfering with the FMCW signal. The OFDM transmitter is to the left (as seen in the figure) of the copper reflector.

The OFDM operates at four distinct center frequencies – 4.2 GHz, 4.19985 GHz, 4.1997 GHz, and 4.1995 GHz – to observe how the spacing between center frequencies affects the impact of the OFDM emissions on the radalt receiver. All OFDM parameters are shown in Table 5.2.

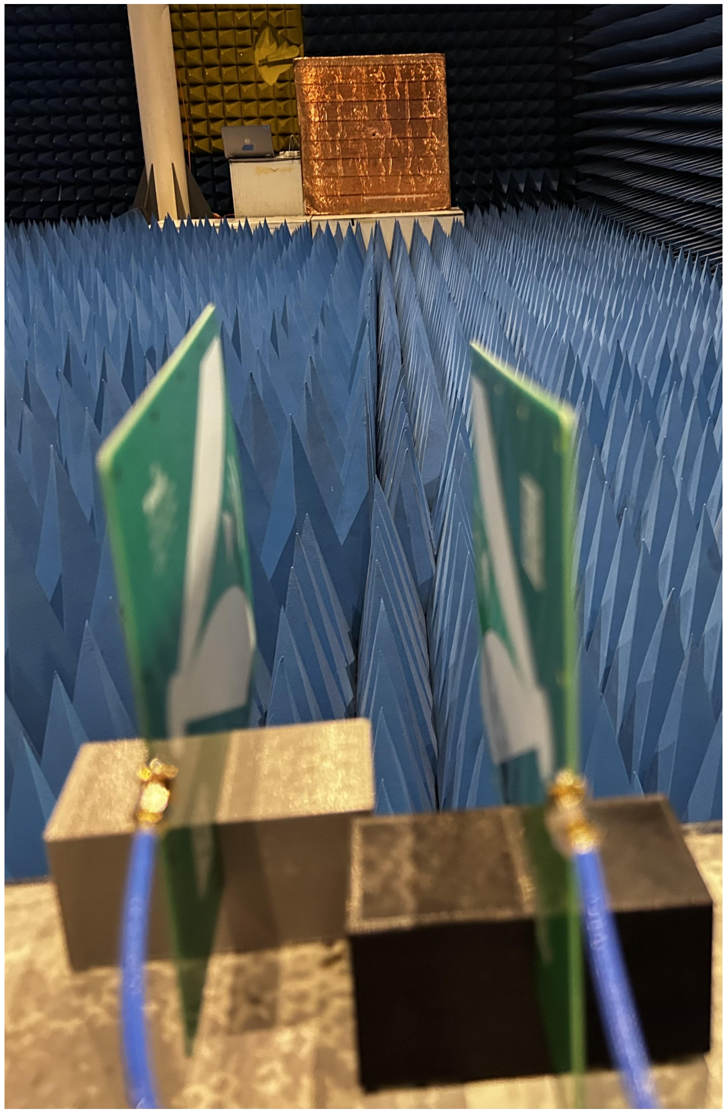

Figure 5.12: Anechoic chamber set up for OOB interference experiments. The two antennas at the forefront of the figure represent the transmit (left) and receive (right) antennas for the FMCW radalt. Note how the receive antenna is slightly behind the transmit antenna to mitigate some of the direct path leakage. On the other side of the anechoic chamber is the copper reflector and the OFDM transmitter. The OFDM transmit antenna is to the left of the target. The copper reflector and OFDM transmitter are approximately 8.56 m from the antennas.

The following experiments are conducted and analyzed in this section:

- Determining the noise floor and interference-to-noise ratio (INR) of the FMCW radalt system.

- The analysis of the effects of OFDM emissions on the FMCW receiver when no target is present.

- The extent to which OFDM emissions hinder the ability of the FMCW radalt to detect a target (that is, range detection, as was done in Section 5.1.2).

All of these experiments have the same principle objective of furthering the understanding of OOB interference and, more specifically, to what extent 5G networks affect the performance of radalts.

Parameter	Value
F_c	4.1995 to 4.2 GHz
F_s	1 MHz
β	300 kHz
T_c	10 μs

Table 5.2: Parameters to generate OFDM emissions transmitted by the B210 SDR. These parameters can be changed according to the application and scenario. Note how the center frequency varies depending on the experiment.

5.3.1 Interference-to-Noise Ratio

The interference-to-noise ratio (INR) determines how strong the interference signal is compared to the noise of the system. In this work, the 5G OFDM emissions are considered the interference signal and the noise is a quality of the FMCW radalt system. The purpose of the INR, in terms of this project, is for two things: to confirm that the OFDM emissions are affecting the FMCW signal in some capacity and to help in assessing the impact of OOB interference. The INR is calculated with either (5.3) or (5.4). Note that if the powers are in decibels, the division becomes a subtraction ((5.4)).

$$INR = \frac{P_i}{P_n} \quad (W) \tag{5.3}$$

where P_i is the interference power and P_n is the noise power.

$$INR_{dB} = P_i - P_n \quad (dB) \tag{5.4}$$

At first, the OFDM transmitter was set up on the same side as the FMCW radalt system. The antenna was placed next to the receive antenna and pointed in the same direction. However, the FMCW radalt did not capture any of the OFDM emissions. It is assumed that since the experiments were conducted within the anechoic chamber, the OFDM emissions were absorbed before the receive antenna captured them. Nonetheless, having the OFDM transmitter emit from the opposite side aligns more with the real world. 5G base stations are closer to the ground (the target for radalts) than in line with radalts, which are in the air. This point will be expanded on in Chapter 6.

The experiment is set up as follows. The transmit antenna is disconnected from the SDR so that the radalt only receives information. The copper reflector is removed from the anechoic chamber as a precaution. There should be no signals reflecting from the target since there are no FMCW transmissions and the OFDM is next to and pointed away from the normal location of the target. The center frequency of the OFDM transmitter is set to 4.2 GHz, the same as the radalt, to determine the highest INR.

Since noise cannot be removed from the system, the interference power is found by comparing the noise floor when there is interference to when there is no interference and can be calculated with (5.5).

$$P_i = P_{total} - P_n \quad (W) \tag{5.5}$$

where P_{total} is the sum of the noise power and the interference power and can be measured as shown in Figure 5.14b.

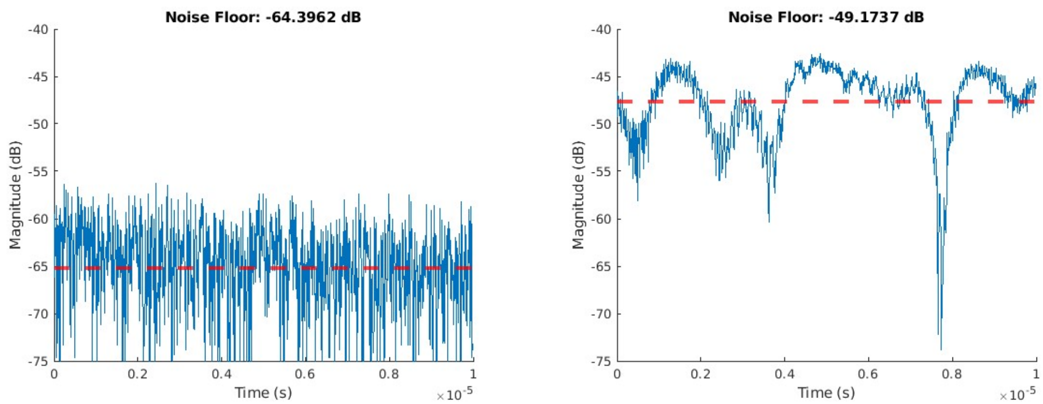

(a) Noise floor with no OFDM interference. The average noise power of the radalt system is −64.39 dB.

(b) Noise floor with OFDM interfernce. The average total power of the radalt system is −49.17 dB.

Figure 5.13: The noise floor with no interference present (a) and with OFDM interference (b). The dashed red line represents the average noise floor, which is also stated in the title of the plot. The center frequency of the OFDM system is at 4.2 GHz, which is the same as the radalt system.

Looking at Figures 5.13a and 5.14b, there is a significant change in the noise floor between the two scenarios. The FMCW radalt system has an average noise power of −64.39 dB. When OFDM interference is added, the noise floor jumps to −49.17 dB. The interference power, calculated with (5.5), is -49.31 dB. Now, applying (5.4), the resulting INR of the OFDM emissions on the FMCW radalt receiver is 15.04 dB. That is, the interference is approximately 32 times stronger than the noise. Figures 5.14a and 5.14b show how the received signal is distorted due to 5G OFDM interference. Therefore, it is valid to assume that any discrepancies, negative effects, or erratic behavior in the FMCW returns are the result of the OFDM interference.

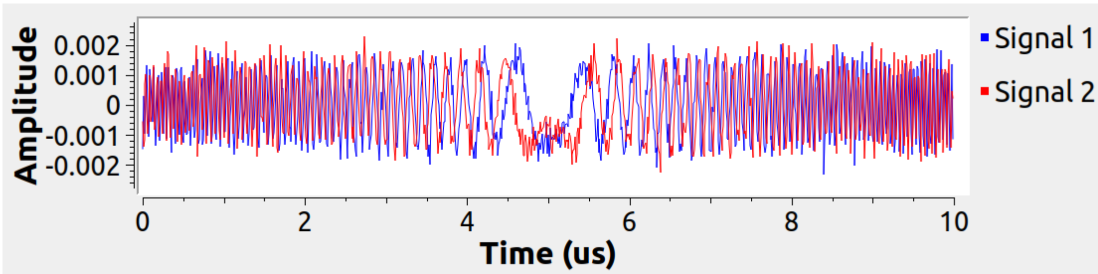

(a) Received signal with no OFDM interference.

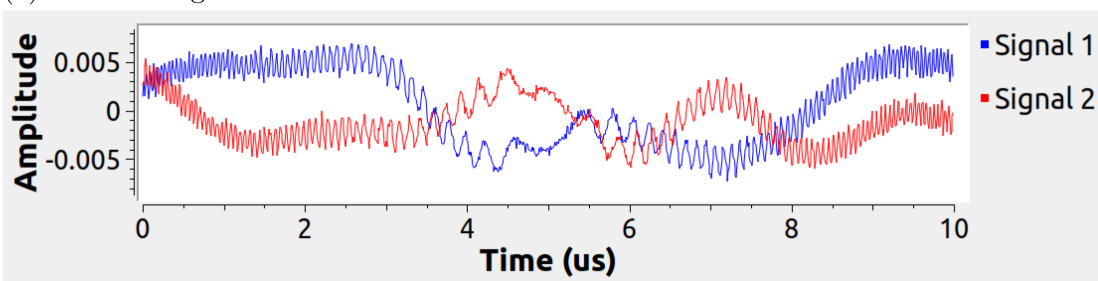

(b) Received signal with OFDM interference.

Figure 5.14: Received signal with (b) and with no (a) OFDM interference. The blue signal is the real part of the signal and the red signal is the imaginary part. These plots are generated with the QT GUI Time Sink block in GNU Radio.

5.3.2 5G OFDM Interference on the Radalt Spectrum

Recall how the direct path leakage is always present whenever the FMCW is operating. The general shape of the direct path leakage is a sinc function and is similar to the output from the loopback test (see Figure 5.4). Figure 5.15 shows the direct path leakage of the FMCW radalt when operating at a center frequency of 4.2 GHz.

The experimental setup is as follows. The transmit and receive antennas are pointed in the same direction, as depicted in Figure 5.12. The copper reflector is removed from the chamber while the OFDM antenna remains pointed towards the radalt system. Since the experiment is conducted within the anechoic chamber, there are no external reflections or technologies that may interfere with the data collection. Thus, only the OFDM emissions are being received by the FMCW radalt (aside from the inherit direct path leakage).

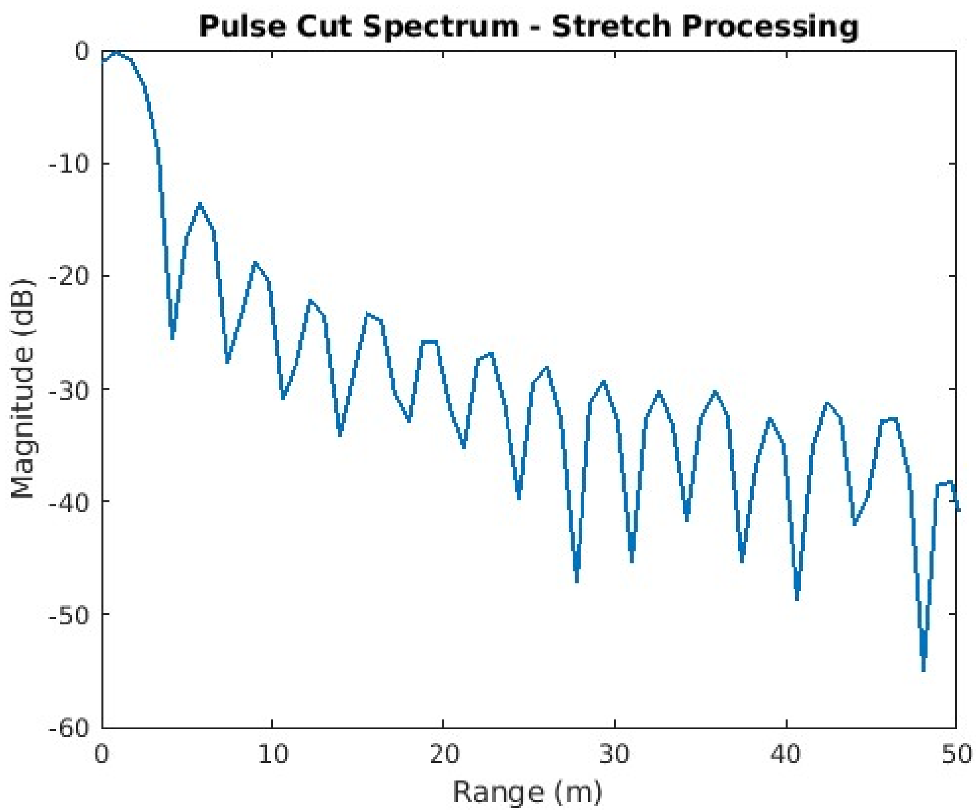

Figure 5.15: Normalized direct path leakage returns of FMCW radalt system. Within the anechoic chamber, there are no targets nor external interference that can affect the FMCW signal.

Observing these data can help to understand the extent to which OFDM emissions affect the FMCW spectrum. Recall that these results are with an INR of 15 dB. Comparisons of Figures 5.16a through 5.16d with Figure 5.15 provide information on how 5G emissions distort and interfere with radalts.

Starting with Figure 5.16a, the effects of the OFDM emissions are clear. Although the mainbeam (peak at 0 m) and first sidelobe appear to be unaffected, the rest of the spectrum has been significantly disrupted. The sidelobes are flattened and raised to approximately −18 dB. Compared to Figure 5.15, which only has the first two sidelobes above −20 dB, this is a drastic impact.

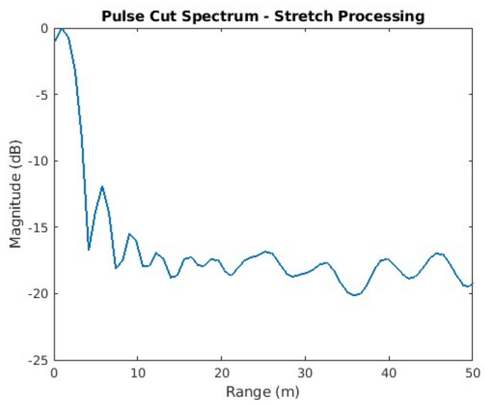

(a) Normalized returns with OFDM emissions operating at a center frequency of 4.2 GHz.

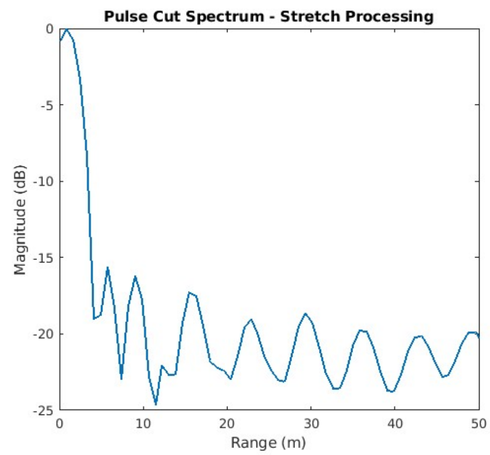

(b) Normalized returns with OFDM emissions operating at a center frequency of 4.19985 GHz.

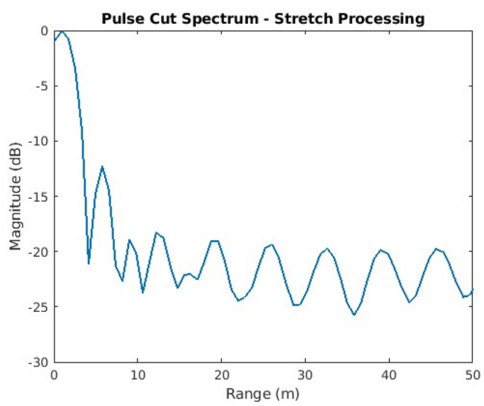

(c) Normalized returns with OFDM emissions operating at a center frequency of 4.1997 GHz.

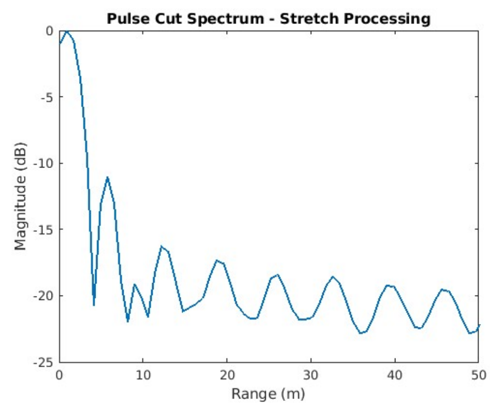

(d) Normalized returns with OFDM emissions operating at a center frequency of 4.1995 GHz.

Figure 5.16: Normalized direct path leakage returns with OFDM emissions operating at one of the four center frequencies: 4.2 GHz (a), 4.19975 GHz (b), 4.1997 GHz (c), or 4.1995 GHz (d). Within the anechoic chamber, the OFDM signal is the only aspect that affects the FMCW system.

Looking now at Figure 5.16b, the center frequency of the OFDM emissions is changed to 4.19985 GHz, 150 kHz below the center frequency of the radalt. The result is expected to be more similar to that in Figure 5.15. However, the bandwidth of the OFDM signal is wide enough to still encompass 4.2 GHz, and thus negative effects are still observed. This time, the sidelobes do not flatten but instead appear to have a sinusoidal shape. Similarly to Figure 5.16a, the sidelobes have been raised to approximately −20 dB. At this point, it appears that the effects of the OFDM emissions still overwhelm the FMCW system.

With a center frequency of 4.1997 GHz, the upper edge of the bandwidth is at 4.2 GHz. Therefore, as previously stated, it is hypothesized that OFDM emissions will have a less significant impact on the FMCW system. However, when comparing Figure 5.16b and Figure 5.16c, they do not look substantially different. The sidelobes have been raised to approximately the same magnitude and still appear sinusoidal. The main difference is that the first sidelobe has a magnitude of approximately −12.5 dB, while in Figure 5.16b it is only −16 dB.

The 5G signals are being transmitted at center frequencies that classify them as intentional 5G emissions (recall Section 3.4) since the bandwidth of the OFDM system encompassed 4.2 GHz, which is the center frequency of the radalt. In Figure 5.16d, the center frequency of the OFDM emissions is set to 4.1995 GHz, meaning that even the bandwidth does not include 4.2 GHz. These 5G signals, although still labeled as intentional 5G emissions since the system still operates within the radalts bandwidth, have the distinct property. The bandwidth of the OFDM emissions do not encompass 4.2 GHz, unlike the other center frequencies, and therefore are expected to result in slightly different behavior. However, apart from a strong first sidelobe, the rest of the FMCW spectrum appears to be the sinusoidal wave that has been common in most of these results.

For all these cases, consider a target at approximately 15 m. Purely from these observations, it seems unlikely that a weak target would be detected by the FMCW radalt. However, targets such as the copper reflector that have strong returns would likely still be detected by the radalt. Even in extreme cases – such as the case in Figure 5.16a – where the center frequency of the OFDM is the same as that of the radalt, the target is strong enough to overcome interference.

Recall that this spectrum is of the direct path leakage, which is not very powerful to begin with. Thus, results may be slightly skewed and indicate that OFDM emissions are more consequential than they really are when trying to detect a target. To verify this, the following section introduces the copper reflector again to act as a target for the FMCW radalt.

5.3.3 5G OFDM Interference on Range Detection

With a target, the scenario becomes more representative of how radalts operate. As described in Chapter 3, the main purpose of radalts is to detect the ground beneath them. In other words, radalts have a constant target below them that they have to measure the range of. If 5G interference deteriorates the performance of this task, radalts run the risk of errors that could become detrimental and even dangerous. This experiment aims to understand how and to what extent OFDM emissions interfere with range detection in FMCW systems.

The experiment is set up as seen in Figure 5.12. The FMCW antennas are facing the copper reflector that has the OFDM transmitter beside it. Recall that the target (and the OFDM transmitter) is 8.56 m from the FMCW radalt antennas. One computer operates the X310 SDR and saves the received data. The other computer runs the OFDM flowgraph on the B210 SDR.

First, the OFDM transmitter was configured with a center frequency at 4.2 GHz, which is the same as the center frequency of the radalt. Figures 5.17a and

5.17b show the two outcomes that occurred when conducting this experiment. Interestingly, the results were not consistent and there were times when the target was detected and times when the target was not detected. Note that from the experiments, it was more common for the radalt to detect the target. Looking more closely at Figure 5.17a, the target is of lower magnitude than the first sidelobe. In a more realistic situation, where one does not preemptively know the location of the target(s), it would not be clear that the second peak is actually a target.

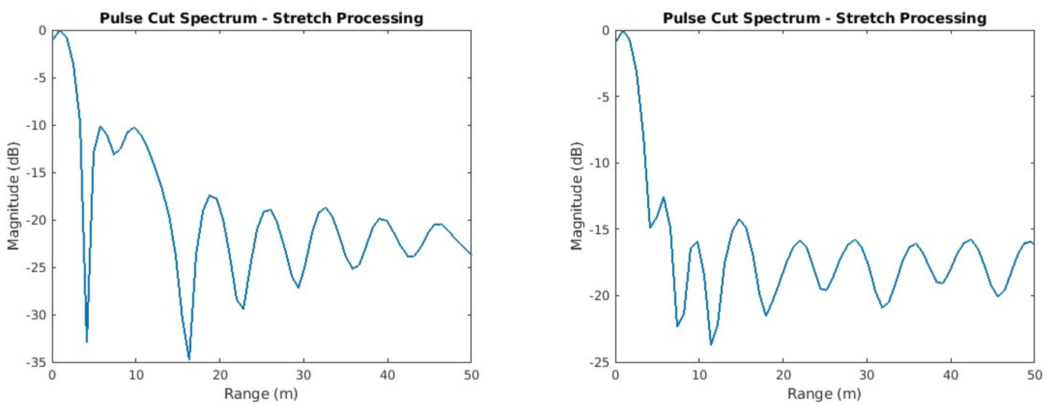

(a) Target detection with range bin shift phenomenon.

(b) Failure to detect target.

Figure 5.17: Range detection of copper reflector with OFDM transmissions operating with a center frequency of 4.2 GHz. The results gave one of two outcomes: target detection (a) or no target detection (b). The FMCW radalt, more often than not, was able to detect the target.

Further, an interesting phenomenon occurred in the data in which the target appeared to be detected. The peak that represents the target is not at the 8.94 m range bin, where it is expected to be. The peak actually shows up one range bin to the right (i.e., one range bin too far away). It is assumed that the OFDM interference caused this error. Since this range bin shift phenomenon never occurred when testing the FMCW radalt (Section 5.1.2), it is valid to assume that the OFDM interference is the cause of this. Alternatively, it could be concluded that the target is never detected by the FMCW radalt and that it is the power of the OFDM interference that the FMCW is receiving. However, the previous section and results like Figure 5.17b, show that OFDM interference flattens the FMCW spectrum even though it does raise the overall magnitude of the sidelobes. Ultimately, the power of the OFDM interference causes a shift in the location of the target by a singular range bin or the target to not be detected at all by the FMCW radalt.

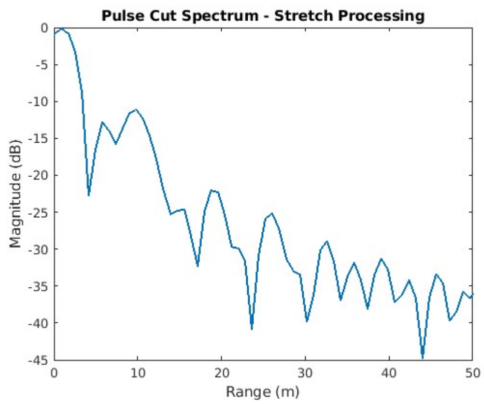

(a) Target detection with range bin shift phenomenon.

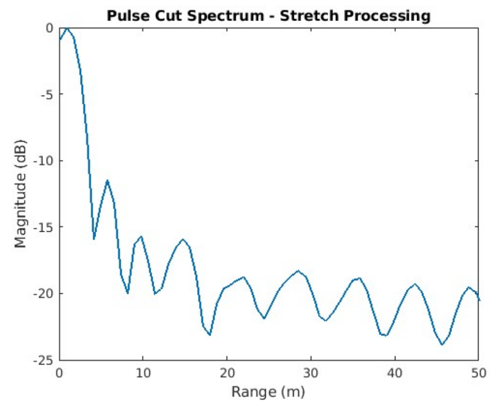

(b) Failure to detect target.

Figure 5.18: Range detection of copper reflector with OFDM transmissions operating with a center frequency of 4.19985 GHz. The results gave one of two outcomes: target detection (a) or no target detection (b). The FMCW radalt, more often than not, was able to detect the target.

Dropping the center frequency of the OFDM transmitter to 4.19985 GHz does not produce considerably different results than when the OFDM transmitter center frequency was set to 4.2 GHz. Again, the results varied between the target being detected and not, as seen in Figures 5.18a and 5.18b. The same range bin shift phenomenon occurred with these results. The target in Figure 5.18a has a greater magnitude than the first sidelobe, making it more evident that the peak is a target – even if it is at the wrong location. The impact of the OFDM emissions on the FMCW radalt spectrum remains apparent, both because of the failures to detect the target and the ambiguous target.

Once the center frequency of the OFDM system has been lowered so that the bandwidth does not include 4.2 GHz, the results become consistent. At these frequencies – 4.1997 and 4.1995 GHz, respectively, for Figures 5.19a and 5.19b – the target is always detected, albeit with the location still shifted by one range bin, by the FMCW radalt.The correct location of the target, however, in these experiments, is closer to the magnitude of the peak, implying that the effects of the OFDM interfernce are lessened with the change in center frequency. In the sidelobes of the FMCW spectrum, there are still distinct effects from the OFDM emissions – the sinusoidal shape reminiscent of what was observed in Section 5.3.2.

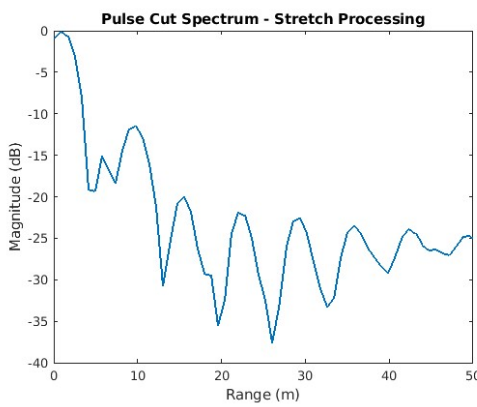

(a) Target detection with OFDM at a center frequency of 4.1997 GHz.

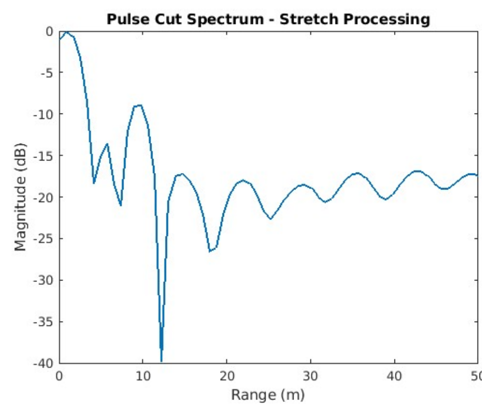

(b) Target detection with OFDM at a center frequency of 4.1995 GHz.

Figure 5.19: Range detection of copper reflector with OFDM transmissions operating with a center frequency of 4.1997 GHz (a) or 4.1995 GHz (b). All experiments resulted in the target being detected.

It is too extreme to say that the target is always detected once the center frequency of the OFDM emissions is low enough that the bandwidth no longer encompasses 4.2 GHz. A more plausible conclusion is that the reduced effects of the OFDM emissions enable more reliable range detection. OFDM emissions where the bandwidth includes the center frequency of the radalt seem to have more severe effects on the FMCW radalt spectrum.

5.4 Conclusions on 5G Interference and Radalts

The main contribution of this work is the fundamental groundwork, including two systems that are representative of radalts and 5G networks, in order to discern the impact of OOB 5G emissions on radalt receivers.

The first part of this chapter introduces two systems: an FMCW radalt and an OFDM transmitter. Both systems were designed in GNU Radio and use SDRs to operate. These two fundamental systems are the basis for all OOB analysis, specifically pertaining to 5G interference on radalts. These systems were tested and set up so that various experiments – even more than those presented in this thesis – could be conducted with ease and ample configurability (both of the systems themselves and their physical layout).

The experiments carried out in Section 5.3 demonstrate the preliminary capabilities of the FMCW radalt and OFDM transmission systems designed in Sections 5.1 and 5.2, respectively. The various experiments allow diverse information on 5G interference on radalts to be acquired. With this same experimental setup, more frequencies, INRs, and targets can be easily tested and observed.

Overall, the main conclusion drawn from the presented experiments is that 5G interference does negatively impact radalt performance. In Section 5.3.3, it is observed that the further the center frequency of the 5G OFDM interfernce is from the FMCW radalt, better and more consistent results are seen. When there are intentional 5G emissions, performance is unreliable and is subject to failures in range detection, which is the main purpose of radalts. Looking back at Section 5.3.1, note that the INR is 15 dB, implying that the OFDM emissions were relatively strong. It is hypothesized that smaller INRs, perhaps signals from rural areas compared to urban cities, would have a lesser impact on radalt performance, whereas higher INRs are more detrimental. This and other future work will be provided in more detail in Chapter 6.

Chapter 6

Conclusions and Future Work

This thesis presents three distinct contributions: a $\Sigma - \Delta$ ADC simulation, the AIR for symbol recovery, and an analysis on the coexistence between 5G networks and radalts. These contributions work towards the mitigation of communications interference and welcoming coexistence in the RF spectrum.

6.1 Summary on WBI and Undersampling ADCs

The first part of this thesis addresses WBI, specifically from a wideband communications signal on a narrowband radar system, and sampling rates. The radar system samples at a rate lower than desired, such that the wideband communications signal ends up undersampled after passing through the ADC. Recovering lost information due to undersampling is the main focus of Chapter 4.

This work proposes a post-processing technique to recover lost symbols from BPSK communication signals when undersampled by a $\Sigma - \Delta$ ADC. Undersampling causes symbols to split into two different samples and be lost within a sample. If the negative effects of undersampling can be overcome in post-processing, computational and material costs of ADCs can be lowered while maintaining and even increasing data rates. The proof-of-concept algorithm presented in Chapter 4 introduces the ability to undersample signals and recover them in post-processing.

The expectation is that an algorithm, such as the AIR, alleviates data storage quantities and mitigates ADC costs.

Furthermore, this thesis introduces a novel $\Sigma - \Delta$ ADC simulation in MATLAB that emulates and replaces the ADC hardware. A mathematical model and diagram of the developed 12-bit $\Sigma - \Delta$ ADC is derived and provided.

6.1.1 Future Work

Since this work is a proof-of-concept, there is much future work to be done to ensure robustness in real-world applications. Some broad future directions include machine learning, developing a real-time algorithm, and adapting the algorithm to other communication signals that are more widely used. The addition of machine learning is a common direction that technology is taking today.

Machine learning could replace the harsh thresholds currently in place to determine the symbols that make up the sample. Using the PDFs of the samples, a machine learning algorithm could learn to recognize different patterns as specific combinations of symbols.

Developing a real-time algorithm would enable direct application to today's systems. Instead of waiting until the system has finished receiving the entire communication signal, the AIR could be applied directly after the ADC, allowing for a more seamless conversion from analog to digital. However, for this to be a possibility, computational costs and complexity need to be greatly reduced to avoid issues such as latency.

Adapting the algorithm to more commonly used communication signals, such as Quadrature Phase Shift Keying (QPSK) and Quadrature Amplitude Modulation (QAM), would allow for more general application. If AIR can be extended to several types of communication signal without loss in performance, proliferation of this algorithm and its benefits can ensue.

More specifically with how the AIR stands now, further tweaking of the thresholds and how the proportions of symbols are determined needs to occur. Especially in situations where three symbols are contained within a singular sample. When this happens, the AIR seems to have a higher error rate and thus must be promptly resolved. Doing this should aid in reducing the error rates for the values of $R > 1$. For the values of $R < 1$, a reevaluation of the PDFs and how the symbols interact within the samples is likely necessary, as a complete symbol is never contained within a sample, and the symbols are always divided between two samples. In addition, developing a more realistic simulation, one in which time delays and hardware jitters are included, would make the results more applicable. In general, more research and analysis is necessary to improve the algorithm for more robust and accurate results that can be applied to real-world data.

6.2 Summary on OOB Interference

Chapter 3 introduces radalts and 5G transmissions, the two technologies of interest in this thesis. It describes their architecture, functionality, and common applications, providing a complete overview. However, the most significant detail is that these technologies reside in adjacent frequency bands within the RF spectrum. Specifically, radalts operate in the 4.2 to 4.4 GHz band and 5G networks operate right below in the 3.7 to 4.2 GHz band. This chapter then introduces OOB interference, a prevalent phenomenon that occurs between adjacent technologies such as these. Striving for coexistence – especially with the ever-increasing number of technologies using the RF spectrum – has become an unavoidable and critical challenge.

This work presents the fundamental systems and preliminary experimentation to tackle the OOB interference problem and coexistence as a whole. A FMCW radalt system and OFDM transmitter, both designed in GNU Radio, allow the user to easily adapt parameters for a variety of scenarios. Additionally, with the use of SDRs, no actual hardware other than the antennas is necessary to observe the interactions between these technologies. The FMCW radalt and OFDM transmitter are validated through testing and experiments are conducted in an anechoic chamber. The analysis of these experiments is presented in Chapter 5, giving a first look at the capabilities of the developed systems and the initial observations of their interactions.

6.2.1 Future Work

Much of the future work for this project involves further exploration of the experiments in Chapter 5 with modifications that would provide more information on how the 5G OFDM emissions interfere wit the FMCW receiver. Three main aspects can be changed: the INR, the center frequency of the OFDM emissions, and the visibility of the target.

Changing the INR would offer insight into the power at which 5G systems start to negatively impact radalt performance. In fact, running these experiments until the OFDM emissions have no effect on the FMCW radalt returns would provide an estimate of an interference power cutoff.

Similarly to the INR, experimenting with the center frequency would provide an interesting comparison between intentional and unwanted 5G emissions, as well as an estimate of where 5G emissions no longer affect the radalt. In practice, it would aid in determining how closely the two technologies can be in the RF spectrum before the OOB interference becomes detrimental to the performance of radalts.

In the experiments conducted in Chapter 5, the target is always a large copper reflector with good reflectivity. However, for radalts, the ground – which is approximately 10,000 m for commercial aircraft at cruising altitudes – is the desired target, and variations in terrain, infrastructure, and weather already affect its visibility. Having targets that more similarly resemble the visibility and reflectivity of the Earth's surface in its varying conditions would help to better discern when range detection fails due to OOB interference from 5G emissions.

In addition, all these aspects need to be varied in conjunction with each other. Change in one aspect is likely to influence the results when changing a secondary aspect. For example, the INR of the OFDM system may change at which center frequency the emissions no longer affect the FMCW receiver.

Moreover, there are other experiments that can broaden the scope of this work. Radalts operate from a high altitude, higher than where any 5G base station resides. This implies that all 5G emissions occur, one, closer to the target (ground) than to the radalt, and two, at an angle to the radalt (since 5G emissions minimally radiate upward). Creating a more realistic scenario within the anechoic chamber would generate more applicable results. The setup for such an experiment would be as follows. The radalt would be set up high with the antennas pointing down towards a target. The OFDM transmitter would be at a slightly higher elevation than the target, with the antenna pointing towards the target as well.

Up until now, the assumption has been that 5G emissions occur near the Earth's surface. Consider the scenario, which is likely on commercial aircraft, where UEs use 5G signals aboard an aircraft. These 5G emissions occur at approximately the same height as the radalt. Experimenting with this scenario could offer new insight on how 5G signals interact with radalts.

Once a decent understanding of 5G networks and radalt interactions has been analyzed, moving all experiments outside, where other technologies and 5G base stations reside, would give more accurate and realistic results. In fact, these experiments would confirm the data collected within the anechoic chamber and provide a deeper understanding of the coexistence between these two technologies.

The goal of these experiments and their analysis is to gain new information and insight on how and to what extent 5G emissions interfere with radalts. Ultimately, the coexistence relationship between 5G transmitters and radalt receivers is far from being solved and understood.

References

[1] J. Kruys and L. Qian, *Sharing RF Spectrum with Commodity Wireless Technologies: Theory and Practice*. Springer, 2011, ISBN: 9789400715844.

[2] P. M. Figliola and J. C. Gallagher, "The federal communications commission's spectrum auction authority: History and options for reinstatement," Congress Research Service, Tech. Rep., Aug. 2023.

[3] "The rf spectrum-sharing challenge," National Security Technology Network, Tech. Rep., 2024.

[4] J. Jeon, H. Niu, Q. Li, A. Papathanassiou, and G. Wu, "Lte with listen-before-talk in unlicensed spectrum," *2015 IEEE International Conference on Communication Workshop (ICCW)*, pp. 2320–2324, 2015.

[5] J. E. Carroll, "Case study: Investigation of interference into 5 ghz weather radars from unlicensed national information infastructure devices, part 3," Institute for Telecommunication Sciences, Tech. Rep., 2012.

[6] F. H. Sanders, "Lessons learned from the development and deployment of 5 ghz unlicesned national information infastructure (u-nii) dynamic frequency selectrion (dfs) devices," Institute for Telecommunication Sciences, Tech. Rep., 2019.

[7] B. H. Kirk, R. M. Narayanan, K. A. Gallagher, A. F. Martone, and K. D. Sherbondy, "Avoidance of time-varying radio frequency interference with software-defined cognitive radar," *IEEE Transactions on Aerospace and Electronic Systems*, vol. 55, no. 3, pp. 1090–1107, 2019.

[8] R. G. Mattingly and J. G. Metcalf, "Fast adaptive spectrum sensing using hardware optimized, cell averaging estimation for cognitive radio and radar applications," *IEEE TRansactions on Aerospace and Electronic Systems*, vol. 59, no. 5, pp. 5084–5096, 2023.

[9] A. F. Martone, K. I. Ranney, K. Sherbondy, K. A. Gallagher, and S. D. Blunt, “Spectrum allocation for noncooperative radar coexistence,” *IEEE Transactions on Aerospace and Electronic Systems*, vol. 54, pp. 90–105, Feb. 2018.

[10] A. E. Mitchell, G. E. Smith, K. L Bell, A. J. Duly, and M. Rangaswamy, “Hierarchical fully adaptive radar,” *IET Radar, Sonar Navigation*, vol. 12, pp. 1371–1379, Dec. 2018.

[11] H. Kuschel, D. Cristallini, and K. E. Olsen, “Tutorial: Passive radar tutorial,” *IEEE Aerospace and Electronic Systems Magazine*, vol. 34, pp. 2–19, 2019.

[12] M. Malanowski, *Signal Processing for Passive Bistatic Radar*. Artech House, 2019, ISBN: 9781630816643.

[13] R. G. Mattingly, N. Goodman, and J. G. Metcalf, “Performance analysis of ofdm interference mitigation via demodulation/remodulation estimation and extraction,” *2024 IEEE Radar Conference (RadarConf24)*, Jun. 2024. DOI: 10.1109/RadarConf2458775.2024.10549356.

[14] J. Price, “The intersection of radar and communications: A study on spectrum management for addressing rf interference,” M.S. thesis, University of Oklahoma, May 2023.

[15] F. H. Sanders, K. R. Calahan, G. A. Sanders, and S. M. Tran, “Measurements of 5g new radio spectral and spatial power emissions for radar altimeter interference,” Institute for Telecommunication Sciences et al., Tech. Rep., 2022.

[16] V. Fortheringham and C. Sharma, *Wireless Broadband: Conflict and Convergence*. IEEE Press and John Wiley Sons, Inc., 2008, ISBN: 9780470227626.

[17] R. S. Kshetrimayum, “An introduction to uwb communication systems,” *IEEE Potentials*, vol. 28, 2 Mar. 2009.

[18] J. N. Pelton, *Satellite Communications*. Springer and International Space University, 2012, ISBN: 9781461419938.

[19] H. Yu, H. Lee, and H. Jeon, “What is 5g? emerging 5g mobile services and network requirements,” *Sustainability*, vol. 9, 10 Oct. 2017.

[20] H. J De Los Santos, C. Sturm, and J. Pontes, *Radio Systems Engineering: A Tutorial Approach*. Springer, 2015, ISBN: 9783319073255.

[21] Y. C. Eldar, *Sampling Theory: Beyond Bandlimited Systems*. Cambridge University Press, 2014, ISBN: 9780511762321.

[22] U. Madhow, *Fundamentals of Digital Communication*. Cambridge University Press, 2008, ISBN: 9780512874144.

[23] W. Kester, *Data Conversion Handbook*. Elsevier: Newnes, 2025.

[24] M. A. Richards, *Fundamentals of Radar Signal Processing*, Third Edition. McGraaw Hill, 2020, ISBN: 9781260468717.

[25] R. G. Mattingly, "Signal processing techniques for radar operation in congested spectrum," Ph.D. dissertation, University of Oklahoma, 2024.

[26] U. Madhow, *Fundamentals of Digital Communication*. Cambridge University Press, 2008, ISBN: 9780512874144.

[27] T. C. Power, S. K. Bergmann, D. Hyslop, and J. L. Oberhausen, *Comments of ctia*, 2022.

[28] "In the matter of expanding flexible use in the 3.7-4.2 ghz band, gn docket no. 18-122," The Federal Communications Commission, 2020.

[29] "Assessment of c-band mobile telecommunications interference impact on low range radar altimeter operations," Radio Technical Commission for Aeronautics, Tech. Rep., Oct. 2020.

[30] M. Viswanathan, *Wireless Communication Systems in Matlab*. Varsha Srinivasan, Jun. 2020, ISBN: 9798648350779.

[31] J. L. Bihan, "Sinc^n fir filter coefficients: Closed-form expressions and recursive relations," *2008 The Third International Conference on Digital Telecommunications*, Jul. 2008. DOI: 10.1109/ICDT.2008.26.

[32] S. A. Flandermeyer, *Gr-plasma: A gnu radio module for radar signal processing*, https://github.com/ShaneFlandermeyer/gr-plasma, 2024.

[33] S. Flandermeyer, R. Mattingly, and J. Metcalf, "Gr-plasma: A new gnu radio-based tool for software-defined radar," in *Proceedings of the GNU Radio Conference*, 2022.

Appendix A

5G Emission Measurements

The Joint Inter-agency 5G Radar Altimeter Interference Quick Reaction Test was formed to better understand the potential issues that arise due to 5G interference in radar altimeters. This includes understanding 5G interference, developing methods for testing this interference, and providing answers to critical questions presented by the government and industry. This project is led by the Department of Defense under the Joint Test and Evaluation Program. This project has been conducted with the cooperation and support of government and industry.

A.1 5G Emission Measurements

5G emissions were measured in three different ways: radiated 5G transmitter emission spectra, three-dimensional (3D) radiation patterns around 5G MIMO arrays (with helicopters), and using ground-based monitoring as verification for the previous method.

These tests were performed at the Table Mountain Radio Quiet Zone facility, commonly referred to as Table Mountain, owned and operated by the US Department of Commerce. Table Mountain is located southwest of Longmont, Colorado, between Boulder and Lyons.

Table A.1 describes the four 5G MIMO array transmitters deployed at Table

Mountain and is derived from [15]. It is important to note that base stations 2

5G Base Station	Manufacturer	Operational Band	MIMO Arrays (# of arrays ×120°)
1	A	3300 to 3600 MHz	3
2	B	3700 to 3980 MHz	1
3	A	3700 to 3980 MHz	1
4	C	3700 to 3980 MHz	1

Table A.1: 5G base stations deployed at Table Mountain for measurements. The azumythal coverage is 120°. Table derived from those in [15].

through 4 (from manufacturers B, A, and C, respectively), are the only upper C-band 5G base station models that are deployed for service in the US. Figure

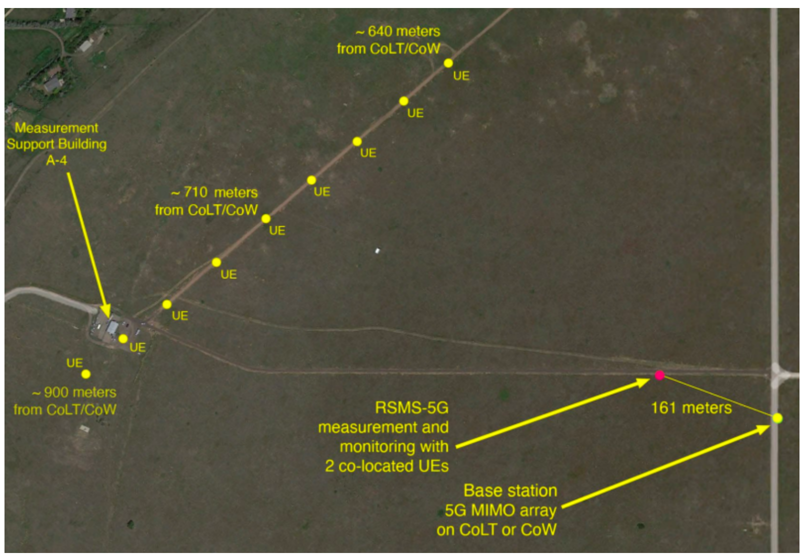

Figure A.1: Top view of the Table Mountain experimental setup. The UEs are all cellphones facing the 5G base station. The RSMS-5G was used to collect data. Courtesy of [15].

A.1 is an aerial shot depicting the geometry. For actual testing, only one base station was present at a time. The UEs were deployed at a nearly right angle to the 5G transmitter. The number of UEs ranged from 9 to 11 and were located 640 to 900 m from the base station. All UEs were stationary at 1 m above the ground and 30 m from each other. Additionally, 1 to 2 UEs were set up at nulls.

A.1.1 Emission Spectra

The National Telecommunications and Information Administration (NTIA) and the research and engineering arm of NTIA, the Institute for Telecommunication Sciences (ITS) designed and engineered a spectrum measurement system simply named the Radio Spectrum Measurement Science (RSMS) system, NTIA/ITS RSMS for short. This system is capable of up to 130 dB of dynamic range in spectrum measurements. The NTIA/ITS RSMS was used to measure the 5G emissions from the MIMO base station antenna arrays. A schematic of the hardware, specifically named the NTIA/ITS RSMS-5G, is shown in Figure A.2.

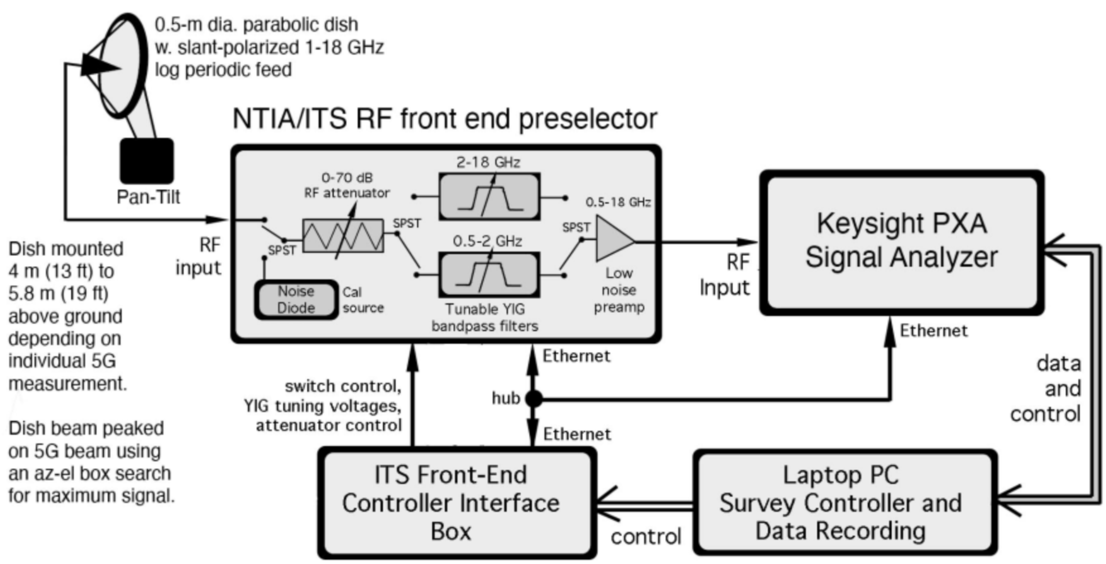

Figure A.2: NTIA/ITS RSMS-5G schemati showing the hardware that makes up the RSMS system. Recall tha the RSMS V5 is the complimentary softare. Courtesy of [15].

The key software aspect of the RSMS-5G system is the step frequency algorithm, which allows a spectrum to be measured a single frequency at a time. A zero-span (time domain) sweep is performed on a frequency for the specified dwell period. The measurement is stored in the time domain sweep at that frequency. This algorithm, using the dwell-and-step approach, allows the spectrum to be unambiguously captured in its entirety, at full available power at all frequencies.

The resolution bandwidth was set to 1 MHz since interference effects on radalt receivers are commonly performed and presented on a per megahertz (MHz^{-1}) basis. Keeping with this nomenclature allowed for easy comparison and usability.

Furthermore, the RSMS V5 (the software of the RSMS-5G system) was used for on-the-ground monitoring of the 5G transmitter while airborne measurements were being recorded. This verified the base station parameters were properly maintained and as expected.

A.1.2 Airborne Radiation Patterns

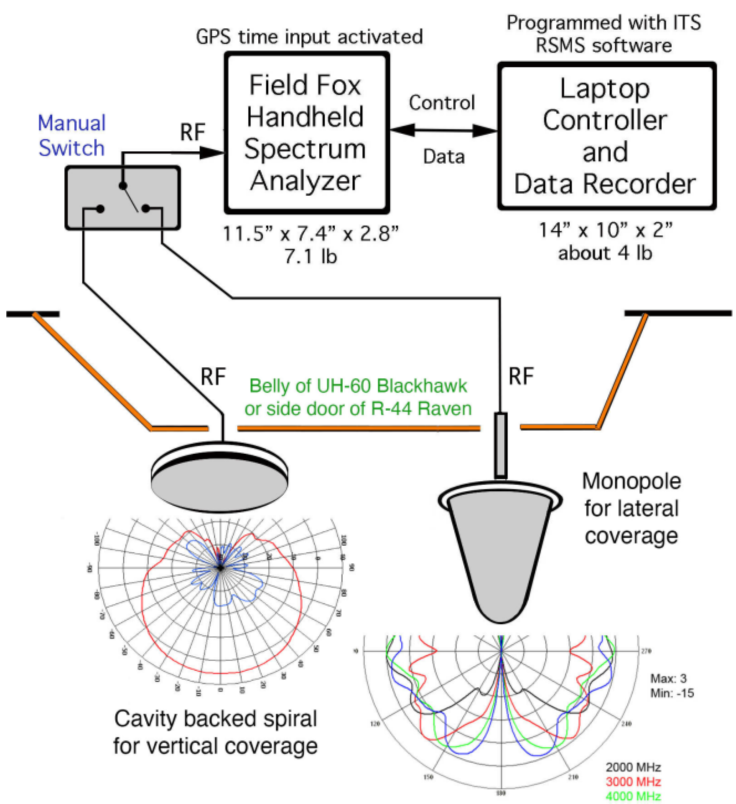

Figure A.3: Dual low-gain antenna schematic for airborne data collection. Courtesy of [15].

The 3D antenna radiation patterns provided the connection between the bench test results and real-world scenarios where harmful interference effects may occur. In other words, the radiation patterns determined at what physical distance and direction from the 5G MIMO array the power level radiated from the array is coupled into, and thus harmful to, the radalt receiver.

Due to the unpredictable and sporadic movement of an airborne platform, in this case a helicopter, a low-gain antenna with nearly uniform gain with a broad angle range was used. Figure A.3 shows this setup. The RSMS V5 software was also employed in these tests to record in-flight data. As with the emission spectra data, the resolution bandwidth was set to 1 MHz for the same reasons as described above (Section A.1.1).

Raw Data to Effective Isotropic Radiated Power Vectors

The conversion of raw field strength data to effective isotropic radiated power (EIRP) vectors allows data to be usable for any point in space at any distance from the array. In the end, three different dataset types are generated:

- $(EIRP/MHz, \theta, \phi)$ vector with EIRP as root mean square (RMS) average-detected power spectrum density per megahertz.
- $(EIRP/MHz, \theta, \phi)$ vector as total RMS average-detected power for the entire 5G channel.
- Heat maps of power as a function of location along the flight path.

A.1.3 Emission Spectrum Results

Depicted in Figures A.4a to A.4c are the measured results of three of the 5G base stations. The base stations operated with 100 MHz channels tuned to 3.8 to 2.98 GHz, which is at the top of the allocated 5G band.

The main structural characteristics of the results are: a wideband power plateau that stretches across the entirety of the 5G transmitter's band, a sharply channelized desired-signal emission that is superimposed on this plateau, and a fast roll-off of spectrum emissions at the band edges. The wideband plateau is

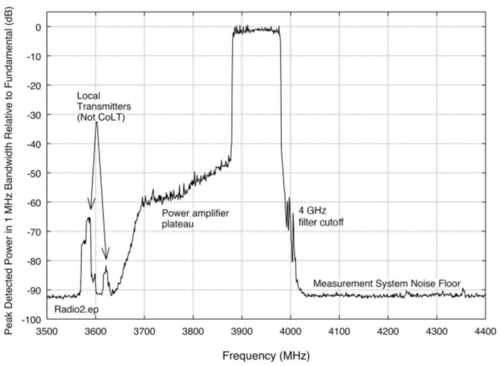

(a) Measured emission spectrum of 5G base station 2.

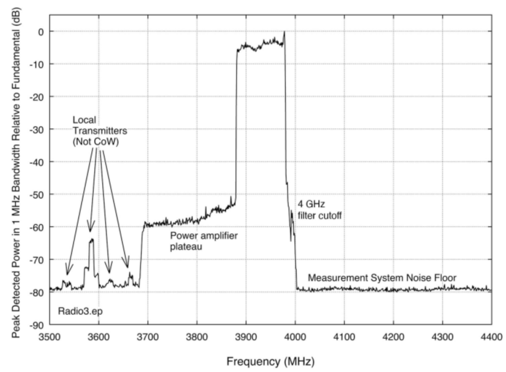

(b) Measured emission spectrum of 5G base station 3.

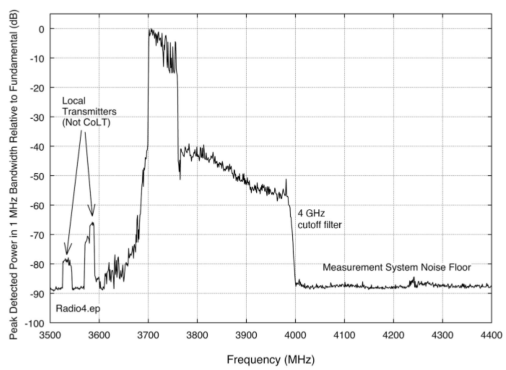

(c) Measured emission spectrum of 5G base station 4.

Figure A.4: Measured emission spectra of 5G base stations 2 through 4 ((a), (b), and (c), respectively), as described in Table A.1.These are possible 5G emissions that could leak into the radalt receiver if the roll-off of the 5G emissions overlap with the filter roll-off of the radalt receiver. Courtesy of [15].

an inherent quality of the amplifier circuit (PAs) within the transmitter. The channelized desired-signal emission is produced with intentional modulation of the signal. The steep spectrum roll-off occurred from effective bandpass filtering on the 3.7 to 3.98 GHz frequency band that the base station was tuned to.

Most importantly, in the radalt band, 5G emissions from all base stations were at least 15 dB below the noise floor of the measurement system. Neither the cycling of the base stations nor small ripples from the cycling were seen.

A.1.4 Airborne Radiation Pattern Results

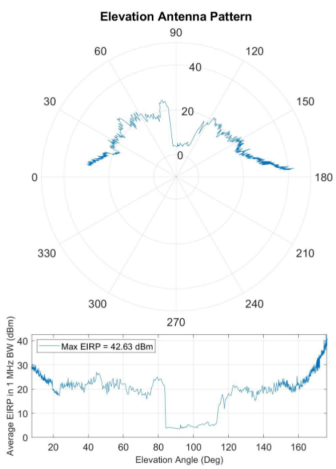

(a) NE to SW overhead traverse for 5G base station 2 at 61 m above ground level.

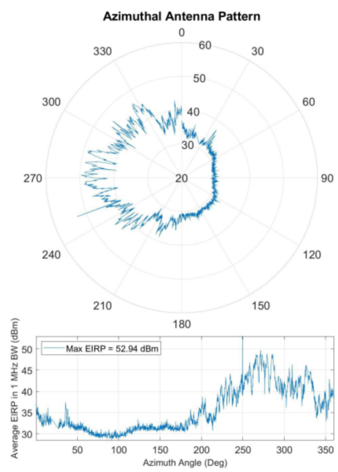

(b) Orbital radiation pattern around 5G base station 2 at 61 m above ground level.

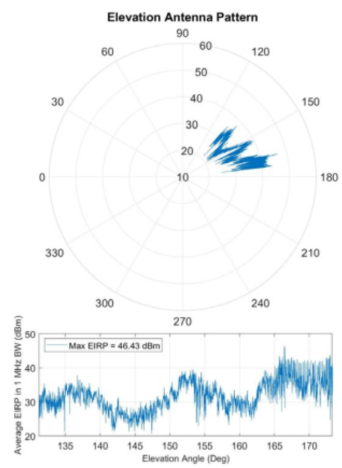

(c) Radiation pattern of ascending hover through 5G base station 4.

Figure A.5: Airborne radiation patterns for different tests and 5G base stations. The top images are in the circular plane showing either elevation (ϕ) (for (a) and (c)) or azimuth (θ) (for (b)) angles. The bottom images are the same data in the (x, y) plane. Courtesy of [15].

In Figures A.5a through A.5c the measured airborne 5G MIMO array radiation patterns are shown. The circular-plane graphs are either elevation (ϕ) or azimuth (θ) angles. The power is total RMS average-detected power ($EIRP/MHz$). The rectangular graphs show the same data but in the (x, y) plane.

Note that there are some outlier points in the datasets (see 250° in Figure A.5b). Although rare, they are assumed to represent emissions from the transmitters.

Appendix B

List of Acronyms and Abbreviations

$3D$	Three-Dimensional
$4G$	Fourth Generation (of Cellular Networks)
$5G$	Fifth Generation (of Cellular Networks)
ADC	Analog-to-Digital Converter
AIR	Algorithm for Information Recovery
$ARRC$	Advanced Radar Research Center
$AVSI$	Aerospace Vehicle Systems Institute
$BLiP$	Beyond Linear Processing
$BPSK$	Binary Phase-Shift Keying
$CMOS$	Complementary Metal-Oxide-Semiconductor
$CTIA$	The Wireless Association (formerly known as the Cellular Telecommunications and Internet Association)
CW	Continuous Wave
DAC	Digital-to-Analog Converter
$DARPA$	Defense Advanced Research Projects Agency
DC	Direct Voltage
$EIRP$	Effective Isotropic Radiated Power
FAA	Federal Aviation Administration
FCC	Federal Communications Commission

FDM	Frequency-Division Multiplexing
FFT	Fast Fourier Transform
FMCW	Frequency Modulated Continuous Wave
I	In-Phase
IF	Intermediate Frequency
IFFT	Inverse Fast Fourier Transfer
IFFT	Inverse Fast Fourier Transform
INR	Interference-to-Noise Ratio
ISM	Industrial, Scientific, and Medicinal (Frequency Band)
ITS	Institute for Telecommunication Science
LFM	Linear Frequency Modulation
LNA	Low Noise Amplifier
LO	Local Oscillator
MIMO	Multiple-Input Multiple-Output
MSPS	Megasamples per second
NTIA	National Telecommunications and Information Administration
OFDM	Orthogonal Frequency-Division Multiplexing
OOB	Out-of-Band
PA	Power Amplifier
PDF	Probability Density Function
Q	Quadrature
QAM	Quadrature Amplitude Modulations
QPSK	Quadrature Phase Shift Keying
Radalt	Radar Altimeter
RF	Radio Frequency

RMS	Root Mean Square
$RSMS$	Radio Spectrum Measurement Science
$RTCA$	Radio Technical Commission for Aeronautics
SDR	Software Defined Radio
$sinc^3$	Third-Order Sinc
SNR	Signal-to-Noise Ratio
$TDWR$	Terminal Doppler Weather Radar
$U-NII$	Unlicensed National Information Infrastructure
UE	User Equipment
UWB	Ultra-Wideband
VFC	Voltage-to-Frequency Converter
WBI	Wideband Interference
XOR	Exclusive OR